Search for Higgs Boson Production in Proton-Antiproton Collisions at $\sqrt{s}$ =1.96 TeV

-DISSERTATION-

Yoshiaki Kusakabe

Presented in partial fulfillment of the requirements
for the degree of the Doctor of Philosophy
in the subject of Physics

Waseda University
Tokyo, Japan
December 2006

Acknowledgements

I want to express thanks to all of the people who supported and encouraged me during the course of my Ph.D program. First of all, I thank Prof. Kunitaka Kondo for his excellent education from my undergraduate days, giving a passionate motivation for high energy physics, precious opportunity to work at the Collider Detector at Fermilab(CDF) and his great generosity. I really enjoyed discussions with him and he always inspired me so much.

I thank Prof. Masakazu Washio. He welcomed me to his laboratory when Prof. Kunitaka Kondo retired from Waseda University. Without his understanding and kindness, I could not finish my Ph.D program at Waseda University. The thank is also to Prof. Shinhong Kim, he provided me with an invaluable financial support, which was inevitable to live in United State from September 2004 to June 2006. He also gave me an opportunity to take part in CDF collaboration meeting held in Elba island Italy from June 2-9, 2006. I express thank to Dr. Kaori Maeshima. She provided me with an opportunity to work for online monitoring system of CDF experiments, the experience gave me an outlook of the experiment. She encouraged me so often when I was stuck in the works at Fermilab, and also served me a lot of delicious dinners so many times.

The work presented in this thesis is based on a lot of collaborations in CDF. In particular, I want to thank Prof. Weiming Yao. He gave me a great opportunity to work for a Top and Higgs physics at CDF and showed me essences of the analysis techniques in hadron collider experiment. I was very impressed with his dedicated attitude toward high energy physics and his kindness. I also wants to express many thanks to Dr. Jason Nielsen and Dr. Anyes Taffard. They are the experts of lepton+jets analyses, and always gave me clear answers to my questions. They are also very kind and friendly to me, and I am really proud of working with them and enjoyed so much. Dr. Yoshio Ishizawa also provided me with a lot of useful information based on his experience in the previous Higgs boson search at CDF RUN2. His information is the baseline for me to start the work, and I want to thank him as well. During the work, Mr. Michael McFarlane and Mr. Tatsuya Masubuchi also gave me a lot of helps and I really appreciate their dedicated attitude. Their supports are crucial for this work, and I could not complete this thesis without our great collaboration. I want to express many thanks to Prof. Thomas Junk, Dr. Anton Anastassov, Dr. Beate Heinemann, Dr. Song Ming Wang, Dr. Jane Natchman, Dr. Kevin Burkett for the convener-ships in Higgs and Exotic physics, and Prof. Evelyn Thomson, Prof. Takasumi Maruyama, Prof. Robin Erbacher, Dr. Jason Nielsen and Dr. Anyes Taffard in Top physics. They helped me to polish up the analysis so much. Without their useful suggestions, comments and careful checks of the method and the results, I

could never push the analysis to this degree of maturity. I also want to express thanks to Dr. Florencia Canelli, Dr. Ben Kilminister, Dr. Bernd Stelzer, Dr. Cristopher Neu, Dr. Daniel Whiteson, Prof. Walfgang Wagner and Prof. John Conway for their useful suggestions and comments which are correlated with their single top or Higgs analysis in other process. I want to say thanks to Ms. Carol Piccolo, Ms. Barbara Perington, and Ms. Dee Hahn. They supported me for a lot of desk works with a lot of kindness, setting up trips and so on.

I want to express my thanks to colleagues and friends. Prof. Takasumi Maruyama, Prof. Shuichi Kunori, Ms. Kyoko Kunori, Dr. Nobuaki Oshima, Dr. Masashi Tanaka, Dr. Tomonobu Tomura, Dr. Koji Ikado, Dr. Takashi Ogawa, Dr. Kohei Yorita, Dr. Masato Aoki, Dr. Takashi Akimoto, Dr. Yoshio Ishizawa, Dr. Ryo Tsuchiya, Mr. Koji Ebina, Mr. Junji Naganoma, Mr. Taichi Kubo, Mr. Tastuya Masubuchi, Mr. Naoki Kimura and Ms. Ai Nagano. They made a lot of fun, helped each other in daily life and provided me with lots of good memories in United States.

I thank the Fermilab staff and the technical staffs of the participating institutions for their vital contributions. This work was supported by U.S. Department of Energy and National Science Foundation; the Italian Instituto Nazionale di Fisica Nucleare; the ministry of Education, Culture, Sports, Science and Technology of Japan; the Natural Sciences and Engineering Research Council of Canada; the National Science Council of the Republic of China; the Swiss Notional Science Foundation; the A.P. Sloan Foundation; the Bundesministerium fuer Bildung und Forschung, Germany; the Lorean Science and Engineering Foundation and the Lorean Research Foundation; the Particle Physics and Astronomy Research Council and the Royal Society, UK; the Russian Foundation for Basic Research; the Comision Interministerial de Cienciay Tecnologia, Spain; in part by the European Community's Human Potential Programme under contract HPRN-CT-2002-00292, Probe for New Physics; and by the Research Fund of Istanbul University Project No.1755/21122001.

I want to express the best of my thanks and appreciations to my parents. They have supported me physically, mentally and financially. I can never appreciate their kindness, generosity, patience and love enough. This thesis is dedicated to my parents. Finally I would like to thank Saeko Hirae. Without her understanding of my situation, kindness, encouragement, patience and love, I could not accomplish the thesis, which is also dedicated to her as well.

Abstract

We performed a search for Standard Model Higgs boson production in association with W boson ($p\bar{p} \rightarrow W^{\pm}H \rightarrow \ell\nu b\bar{b}$) in $p\bar{p}$ collisions at $\sqrt{s} = 1.96$ TeV. The search uses the data collected between February 2002 and February 2006 at Collider Detector at Fermilab (CDF), which corresponds to an integrated luminosity of about 1 fb^{-1}. The experimental final state of $WH \rightarrow \ell\nu b\bar{b}$ process is lepton ($e^{\pm}/\mu^{\pm}$), missing transverse energy and two jets. The largest background in lepton+jets events is W+light flavor process, therefore the identification of jets as b-jets reduces this kind of background significantly. We used displaced SECondary VerTeX b-tagging (SECVTX) technique, which utilizes the signature that b-jets have secondary vertex displaced away from primary vertex because of the long life time of B-mesons. However, there is still much contamination in SECVTX b-tagged jets. Finite resolution of secondary vertex tracking measurements results in false tags, and c-jets are also identified as b-jets due to the long life time of D-mesons frequently. For the purpose of increasing the purity of the SECVTX b-tagged jets, we applied Neural Network to SECVTX tagged jets for the first time by using secondary vertex variables and some variables independent of it. Neural Network filter rejects 65% of light flavor jets and 50% of c-jets from the SECVTX tagged jets. We improved the sensitivity of the Higgs boson signal search by 10% with Neural Network b-tagging technique. Events with one high p_T electron or muon, large missing transverse energy and either single SECVTX b-tagged jet which passes the Neural Network filter or at least two SECVTX b-tagged jets are selected. The number of selected events and dijet mass distributions are consistent with the Standard Model background expectations. Therefore we set an upper limit on $\sigma(p\bar{p} \rightarrow WH) \cdot Br(H \rightarrow b\bar{b})$ as 3.9 to 1.3 for Higgs boson mass from 110 to 150 GeV/c^2 at 95% confidence level (C.L.). The upper limit obtained from $WH \rightarrow \ell\nu b\bar{b}$ process with 1 fb $^{-1}$ is far away from the Standard Model Higgs boson production expectation by a factor of 20 to 100 as a function of Higgs boson mass. To obtain stronger constraint on the Higgs boson production, we combined the upper limits obtained in processes of $ZH \rightarrow \nu\bar{\nu}b\bar{b}$, $ZH \rightarrow \ell\bar{\ell}b\bar{b}$ and $gg \rightarrow H \rightarrow W^{+}W^{-} \rightarrow \ell\bar{\ell}\nu\bar{\nu}$ at CDF. The combination of different channels gives a constraint on the ratio of 95% confidence level upper limit divided by the Standard Model prediction ($(\sigma \cdot Br)_{95}/(\sigma \cdot Br)_{\mathrm{SM}}$), which results in the ratio as 10 to 40 for Higgs boson mass between 110 and 200 GeV/c^2. Finally, the combination of Higgs boson searches between CDF and DØ is also performed. The resulting constraint on $(\sigma \cdot Br)_{95}/(\sigma \cdot Br)_{\mathrm{SM}}$ is about 4 to 10 for Higgs boson mass between 110 and 200 GeV/c^2.

Contents

List of Tables

List of Figures

Chapter 1

Introduction

In the past century, mankind came to know the world of elementary particles with the developments of quantum mechanics, relativity and technologies of accelerators and detectors. The theory which places three generations of quarks and leptons as the fundamental particles and describes the interaction between materials by the exchange of gauge bosons is called "the Standard Model" [1–3] at present. The interactions between matters are categorized into four sectors of "Strong", "Weak", "Electromagnetic" and "Gravitational" interactions. The Standard Model does not include "Gravitational force" in its framework because there has been no realistic experimental fact that confirms theory of gravitation in the scale of fundamental particles. Gauge bosons of strong, weak and electromagnetic interactions are called as gluon(g), weak bosons(W/Z), and photon(γ), which are introduced by the principle of gauge invariance in the gauge groups of $SU(3)$, $SU(2)$ and $U(1)$ respectively. Therefore the Standard Model belongs to $SU(3) \times SU(2) \times U(1)$ group[1]. The Standard Model describes nature to an extremely good precision, and there has been no evidence that implies phenomena beyond the Standard Model. However the principle of gauge invariance prohibits the mass term in Lagrangian, which must be present to describe realistic materials. To overcome this difficulty, a scalar field called as "Higgs field" that breaks the symmetry spontaneously is introduced to keep the gauge invariance[4]. But the Higgs boson(H), the quantized Higgs field, has not been discovered in any experiment yet. Thus, one of the most important and interesting tasks in elementary particle physics is to discover Higgs boson or reject its existence.

With the developments of technologies of accelerators and detectors, the experiments in high energy particle collisions are general approaches to study fundamental parti-

---

[1] More precisely, the Standard Model belongs to $SU(3)_{\mathrm{c}} \times SU(2)_{\mathrm{L}} \times U(1)_{\mathrm{Y}}$ group regarding color, weak iso-spin and hyper currents. In electroweak theory, W, Z and γ are obtained from $SU(2)_{\mathrm{L}} \times U(1)_{\mathrm{Y}}$ symmetry. When only Electro Magnetic(EM) interaction is considered, γ is derived from $U(1)_{\mathrm{EM}}$ symmetry.

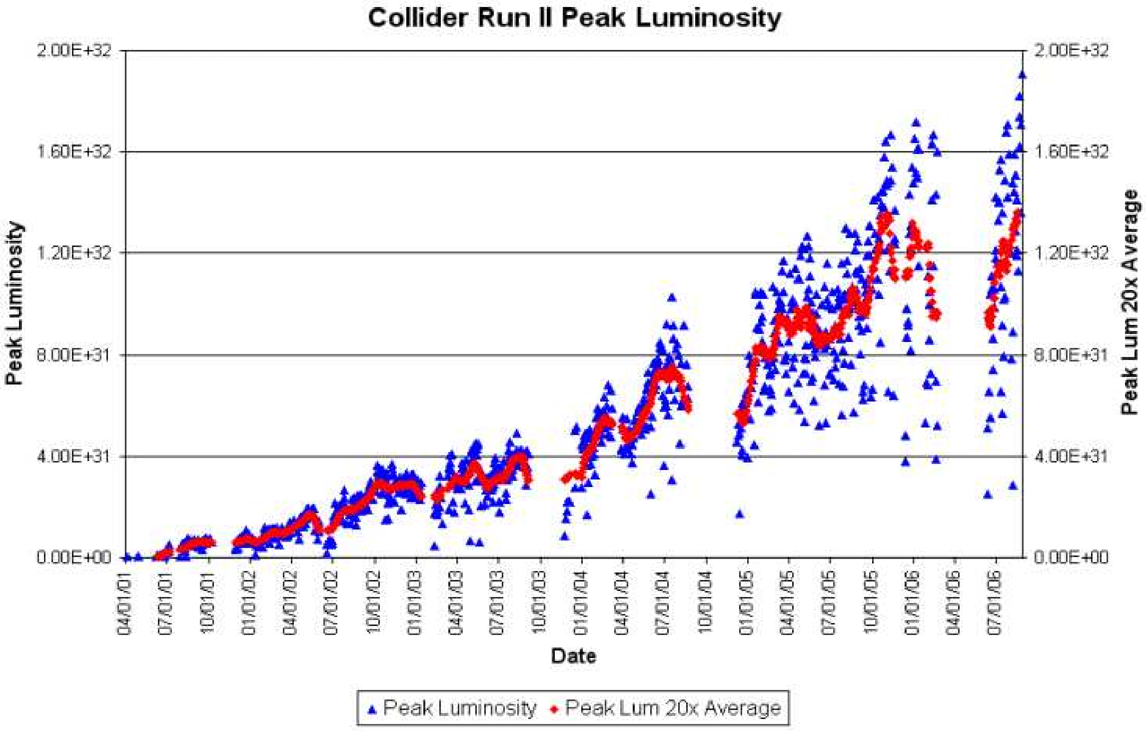

Figure 1.1 Peak value of instantaneous luminosity for each store (blue) and averaged value in the nearest 20 stores (red) in chronological order.

cles. Especially top quark was discovered in the TEVATRON RUN1 experiment (proton-antiproton collisions at $\sqrt{s} = 1.8$ TeV) at Fermi National Accelerator Laboratory (Fermilab) by CDF (Collider Detector at Fermilab) group in 1995[5]. After the discovery of top quark, the TEVATRON was reinforced with $\sqrt{s} = 1.96$ TeV and the luminosity was improved significantly[2]. The TEVATRON has started RUN2 experiment from February 2002, and CDF has accumulated data corresponding to an integrated luminosity of about 1.5 fb^{-1} by February 2006 in total. The amount of good quality data is about 1 fb $^{-1}$, which is used for physics analyses. Instantaneous and integrated luminosity as functions of time are shown in **Figs.1.1** and **1.2**.

TEVATRON is the accelerator with the highest energy in the history and the only active accelerator in the world when this work is performed. The main purposes of the RUN2 experiment are precise measurement of top quark mass, understanding of the top quark properties, precise measurements of electroweak interaction, searches for phenomena beyond the Standard Model and searches for Higgs boson. In accordance

---

[2] In RUN1 experiment, maximum peak instantaneous luminosity and delivered integrated luminosity were about 2.0 $\times 10^{31}$ $\text{cm}^{-2}\text{s}^{-1}$ and 110 pb^{-1} respectively.

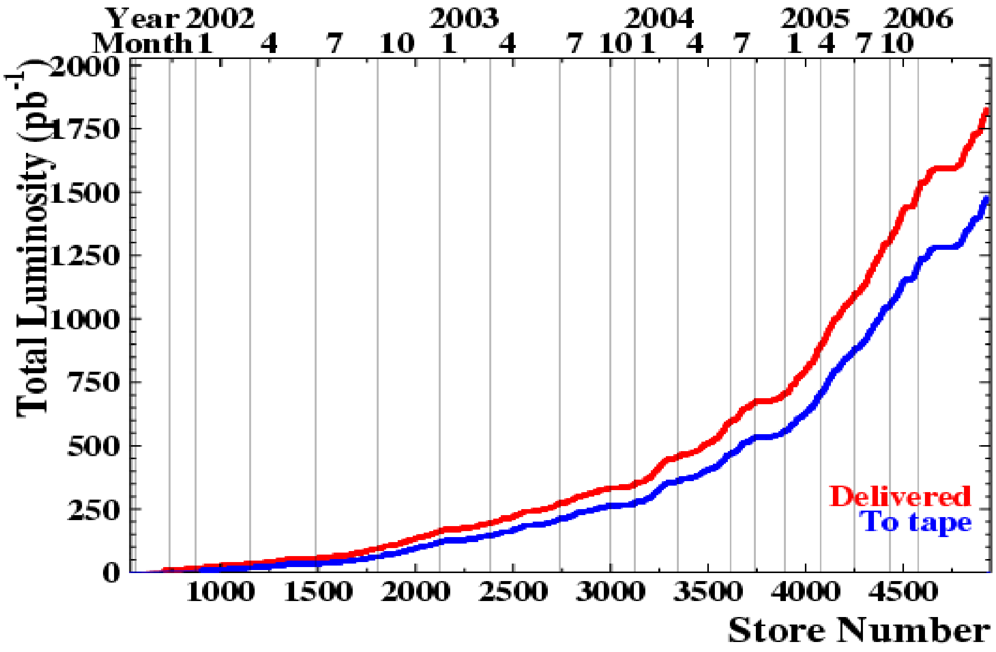

Figure 1.2 Integrated luminosity as a function of time. "Delivered" is the integrated luminosity provided by the TEVATRON and "To tape" is the luminosity acquired by CDF detector and recorded on tape, which is the data used in physics analysis.

with the report from LEP2 direct search for Higgs boson production in e^+e^- collisions, the possibility that Higgs bosom mass(m_H) is less than 114.4 GeV/c^2 is excluded at 95% confidence level(C.L.)[6]. Assuming the Standard Model is the correct theory of nature, there is a correlation between W boson, top quark and Higgs boson mass. Precise measurements of W boson and top quark mass from LEP2 and TEVATRON experiments tell that the Higgs boson mass is lower than 199 GeV/c^2 at 95% C.L. including the latest result of the LEP2 Higgs boson search[7]. Thus, Higgs boson mass is expected to be comparatively light ($114.4 < m_H < 199$ GeV/c^2).

Having the basis in those experimental situations and facts, TEVATRON is the only and the most exciting place to search for Higgs boson with a possibility of discovery at the point of 2006. The main Higgs boson production processes at the TEVATRON are $gg \rightarrow H$, $q\bar{q}' \rightarrow W^{\pm}H$ and $q\bar{q} \rightarrow Z^0H$ in the order of magnitude of production cross section. Higgs boson has large branching ratio in the decay modes of $H \rightarrow b\bar{b}$ for $m_H < 135$ GeV/c^2 and $H \rightarrow W^+W^-$ for $m_H > 135$ GeV/c^2. Furthermore, if the W/Z bosons in the processes decay leptonically, huge background contributions from QCD multi-jets processes can be rejected. Therefore $WH \rightarrow \ell\nu b\bar{b}$ and $ZH \rightarrow \nu\bar{\nu}b\bar{b}$, $\ell\ell b\bar{b}$, where ν, ℓ and b denote neutrino, lepton(electron or muon), and bottom quark, are considered as the most sensitive processes for low mass Higgs boson ($m_H < 135$ GeV/c^2) searches at

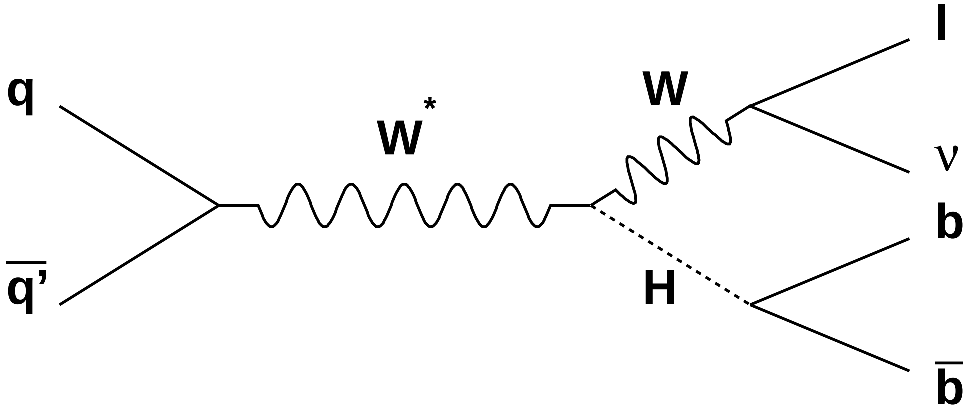

Figure 1.3 The Feynman diagram of $q\bar{q'} \rightarrow WH \rightarrow \ell\nu b\bar{b}$ process.

the TEVATRON. A search for $WH \rightarrow \ell\nu b\bar{b}$ shown in **Fig.1.3** was performed previously with an integrated luminosity of 319 pb^{-1} at CDF RUN2[8, 9]. The work described in this thesis is intended to improve the technique for the search and use the full data set collected at this point.

This thesis is organized as follows. The next chapter begins with theoretical aspects of the Standard Model and the results of the Higgs boson searches in the past. Chapter 3 describes the experimental apparatus of TEVATRON and CDF detector in detail. In chapter 4, methods of bottom quark identification is discussed. In chapter 5, the data set and event selection criteria used in the analysis are mentioned. The method of the Standard Model background estimation and the estimated background are shown in Chapter 6. As a cross check of background estimation, $t\bar{t}$ production cross section measurement is also performed there. The study of the WH signal detection efficiency and systematic uncertainties are performed in Chapter 7. In Chapter 8, the method and the result of the Higgs boson search in WH process are shown. Furthermore, to improve the constraint on Higgs boson production, the combination of results from other channels is also discussed and the result is shown. Finally, the works in this thesis are concluded and the future prospect of the Higgs boson search is mentioned in Chapter 9.

Chapter 2

The Standard Model

The theory which places quarks and leptons as the elementary particles and explains the interactions between matters by the exchange of gauge bosons is called "the Standard Model". Four kinds of forces, strong, weak, electromagnetic and gravitational forces, exist in nature. The Standard Model describes those forces except for gravitation, and the theory described nature to an extremely good precision. The theory is based on two principles of "least action principle" and "gauge invariance". The first principle gives the equation of motion of matters, and the second one introduces the gauge bosons as force carriers. The Standard Model also requires a fundamental scalar field, which spontaneously breaks symmetry, to give mass to particles and bosons without breaking gauge symmetry, and it is called "Higgs field".

2.1 Elementary Particles and Gauge Bosons

Starting from the discovery of electron, the first elementary particle, in the cathode ray experiment by J.J. Thomson in 1897[10], other fundamental particles have been discovered in the following 100 years. The quarks and leptons are considered as the fundamental particles for matters in our universe. Those particles have spin 1/2, which obey the Pauli exclusion principle, and form weak iso-spin doublets. There exist anti-particles for all of the quarks and leptons possessing the same properties of spin, mass and other quantum numbers with an exception of carrying an opposite sign of electric charge. Electron(e), muon(μ), tau(τ), with electric charge(Q) of -1, and their associated neutrinos(ν_e, ν_μ, ν_τ) with Q=0 were found and called as leptons. The presence of up(u), charm(c), top(t) with $Q = 2/3$, and down(d), strange(s) and bottom(b) with $Q = -1/3$ are also confirmed and they are categorised as quarks. Quarks carry color charge for the strong interaction, which was introduced in an analogy of the electric charge in

	Generation			Properties		
	1st	2nd	3rd	Spin	Electric charge	Interaction
Quark	$\begin{pmatrix} u \\ d \end{pmatrix}$	$\begin{pmatrix} c \\ s \end{pmatrix}$	$\begin{pmatrix} t \\ b \end{pmatrix}$	1/2	+2/3 −1/3	EM, Weak, Strong
Lepton	$\begin{pmatrix} \nu_e \\ e \end{pmatrix}$	$\begin{pmatrix} \nu_\mu \\ \mu \end{pmatrix}$	$\begin{pmatrix} \nu_\tau \\ \tau \end{pmatrix}$	1/2	0 −1	Weak EM, Weak
		Mass(GeV/c^2)		Spin	Electric Charge	Interaction
Gauge Boson	γ	0		1	0	EM
	W	80.4			±1	EM, Weak
	Z	91.2			0	EM, Weak
	g	0			0	Strong

Table 2.1 The fundamental particles and gauge bosons in the Standard Model. There also exist the anti-particles for each lepton and quark carrying the same properties and quantum numbers except for opposite sign electric charge.

electromagnetic interaction. Based on the properties under the electroweak interaction, neutrinos $(\nu_e, \nu_\mu, \nu_\tau)$, and quarks of (u, c, t) are categorized into up type, because they carry +1/2 of 3rd component of weak iso-spin. Charged leptons of (e, μ, ν) and quarks of (d, s, b) are categorized into down type because they carry -1/2 of 3rd component of weak iso-spin. In accordance with the weak interaction, those quarks and leptons form weak iso-spin doublets as shown in **Table 2.1**. The interacitons between materials are described by the exchange of the gauge bosons of photon(γ), weak boson(W, Z) and gluon(g) for ElectroMagnetic(EM), weak, and strong interactions respectively.

2.2 Gauge Theory

The least action principle is considered as the basis of the raw of nature, and it introduces all of the raws of motion in a consistent way. The principle is well accepted and considered as one of the ultimate principles in nature. This principle gives the Euler-Lagrange equation:

$$\partial^\mu \frac{\partial \mathcal{L}}{\partial(\partial^\mu \psi(x))} - \frac{\partial \mathcal{L}}{\partial \psi(x)} = 0, \tag{2.1}$$

where $\mathcal{L}$, ψ and ∂^μ are Lagrangian, field as a function space-time(x) and space-time derivative. After the quantum mechanics and relativity were established, relativistic quantum field theory was proposed and developed by many physicists to describe the world of fundamental particles. The description that forces are propagated by the exchange of gauge bosons, which is obtained by the quantization of the gauge field, is well accepted for material interaction in terms of the concept of action through medium. The gauge bosons and its dynamics are obtained from the gauge principle ”The realistic interaction takes place to keep Lagrangian of the frame invariant under the transformation in the associated gauge group”.

2.2.1 Global Gauge Transformation

The Lagrangian of free Dirac field(ψ) is written as:

$$\mathcal{L} = \bar{\psi}(x)\left(i\gamma^{\mu}\partial_{\mu} - m\right)\psi(x), \tag{2.2}$$

where γ^{μ} is Dirac's γ matrix and m is mass of the Dirac particle. The transformation of field ψ:

$$\psi(x) \to e^{iQ\alpha}\psi(x), \tag{2.3}$$

where Q and α are electric charge and a space-time independent parameter respectively, keeps the Lagrangian(Eq.2.2) invariant. The operator of $e^{iQ\alpha}$ means one dimensional unitary transformation($U(1)$). This symmetry results in current conservation law by considering Noether's theorem[11, 12], which is described as:

$$\partial_{\mu} j^{\mu} = 0, \tag{2.4}$$

where j^{μ} is the 4-current vector:

$$j^{\mu} = -Q\bar{\psi}\gamma^{\mu}\psi. \tag{2.5}$$

2.2.2 Local Gauge Transformation

The global gauge transformation considered in the previous section is generalized by adding a space-time dependence to the parameter α, which is called local gauge transformation:

$$\psi(x) \to e^{iQ\alpha(x)}\psi(x). \tag{2.6}$$

The Lagrangian(Eq.2.2) is not invariant under this transformation. To keep the gauge invariance condition, it is necessary to find a covariant derivative which transforms as:

$$D_{\mu}\psi(x) \to e^{iQ\alpha(x)} D_{\mu}\psi(x). \tag{2.7}$$

A vector field A_μ, which cancels extra terms from local gauge transformation, is introduced to attain the invariance. The corresponding covariant derivative is written as:

$$\partial_\mu \to D_\mu = \partial_\mu + iQA_\mu, \tag{2.8}$$

where A_μ transforms under local gauge transformation as

$$A_\mu \to A_\mu - \frac{1}{Q}\partial_\mu \alpha(x). \tag{2.9}$$

This derivation means that the existence of a gauge field A_μ is required to keep gauge invariance. Finally, a gauge invariant field strength tensor:

$$F_{\mu\nu} = \partial_\mu A_\nu - \partial_\nu A_\mu, \tag{2.10}$$

is added to the Lagrangian(Eq.2.2), and Lagrangian of Quantum Electro Dynamics(QED) is obtained as:

$$\mathcal{L}_{\mathrm{QED}} = \bar{\psi}(x)\left(i\gamma^\mu D_\mu - m\right)\psi(x) - \frac{1}{4}F_{\mu\nu}F^{\mu\nu}. \tag{2.11}$$

$\mathcal{L}_{\mathrm{QED}}$ cannot contain mass term of A_μ in a form of $\frac{1}{2}m^2 A_\mu A^\mu$ because it is not invariant under gauge transformation. This is consistent with the experimental fact that photon, the gauge boson of electromagnetic interaction, is massless particle. Euler-Lagrange equation(Eq.2.1) gives equation of motion of the fields. If the Dirac field ψ is used for variation, Dirac equation:

$$\left(i\gamma^\mu \partial_\mu - m\right)\psi(x) = Q\gamma^\mu A_\mu \psi(x), \tag{2.12}$$

is obtained. Otherwise, if gauge field A_μ is varied, Maxwell equation:

$$\partial_\mu F^{\mu\nu} = j^\nu, \tag{2.13}$$

is derived. Therefore, gauge invariance and least action principle are the bases of the description of elementary particles.

2.3 Higgs Mechanism

Despite the phenomenal success of the predictive power of the Standard Model, there is a portion of the framework that has no experimental evidence. One particularly smart aspect for the Standard Model formalism is the unification of the electromagnetic and weak interactions through the exploitation of the local gauge symmetry. This symmetry is a quality of the theory in which the Standard Model Lagrangian is invariant to local gauge transformations. However, This symmetry requires $W^{\pm}$ and Z^0 to be massless, because mass terms in the Lagrangian breaks the symmetry. The resulting massless weak bosons contradict experiments. Fundamental fermions and bosons can acquire mass without breaking gauge invariance by introducing a fundamental scalar doublet field Φ defined as:

$$\Phi = \begin{pmatrix} \Phi^+ \\ \Phi^0 \end{pmatrix}, \tag{2.14}$$

where Φ^+ and Φ^0 are complex fields written as:

$$\Phi^+ = \frac{\Phi_3 + i\Phi_4}{\sqrt{2}}, \tag{2.15}$$

$$\Phi^0 = \frac{\Phi_1 + i\Phi_2}{\sqrt{2}}. \tag{2.16}$$

The field Φ is called "Higgs field"[4], which breaks the electroweak symmetry spontaneously. Higgs potential takes the form of

$$V(\Phi) = \mu^2 \Phi^\dagger \Phi + \lambda (\Phi^\dagger \Phi)^2, \tag{2.17}$$

where λ is a self coupling of the Higgs field. If μ^2 is selected as negative value, Higgs potential acquire minimum at non-zero points as shown in **Fig.2.1**. The electroweak symmetry is spontaneously broken when one of the vacuum state is selected. When the field is expanded around the non-zero vacuum expectation value of:

$$v = \sqrt{\frac{-\mu^2}{\lambda}} = \sqrt{\frac{G_F}{\sqrt{2}}} = 246(\mathrm{GeV}), \tag{2.18}$$

where G_F is the Fermi coupling constants, weak bosons and fermions acquire mass of:

$$m_W = \frac{1}{2} v g, \tag{2.19}$$

$$m_Z = \frac{1}{2} v \sqrt{g^2 + g'^2}, \tag{2.20}$$

$$m_f = \frac{1}{\sqrt{2}} g_f v, \tag{2.21}$$

where g, g' are the coupling constant in electroweak interaction, and g_f is the coupling constant between Higgs boson and fermion.

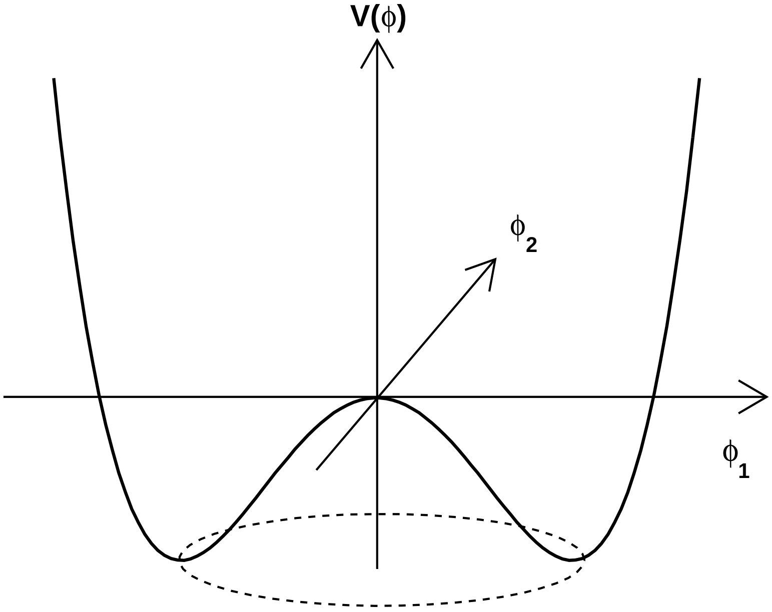

Figure 2.1 Higgs potential as a function of scalar field ϕ_1 and ϕ_2, where $\mu^2 < 0$ and $\phi_3 = \phi_4 = 0$ are assumed.

2.4 Higgs Production and Decay

The Next to Leading Order(NLO) Higgs boson production cross section at the TEVATRON[13] is shown in **Fig.2.2**. The gluon fusion Higgs production has about 10 times larger cross section than WH process, and the cross section of WH process is about twice as much as ZH production.

The Higgs boson decay branching ratio is calculated by HDECAY[14], which takes care of NLO effect, and shown in **Fig.2.3**. Higgs boson decay is dominated by $H \to b\bar{b}$ mode for m_H <135 GeV/c^2, and $H \to W^+W^-$ mode for m_H >135 GeV/c^2. In general, QCD multi-jet processes has far larger cross section than that of Higgs boson production. This results in that Higgs boson searches in the processes $gg \to H \to b\bar{b}$, $WH \to q\bar{q}'b\bar{b}$, and $ZH \to q\bar{q}b\bar{b}$ are not expected to have good sensitivities. However, the requirement of the leptonic decay of the associated weak boson reduces such a huge QCD jets events. As a result, $WH \to \ell\nu b\bar{b}$ is expected to be one of the most sensitive processes for low mass Higgs boson ($m_H <$ 135 GeV/c^2). In this thesis, the branching mode of $W \to \tau\nu_\tau$ is not considered because τ is not observed directly and the identification and its kinematics measurement are based on the decay products of it. This fact results in the contamination of the lepton identification in the events and difficulty in the event handling. In this thesis, lepton(ℓ) denotes only $e^\pm$ or $\mu^\pm$.

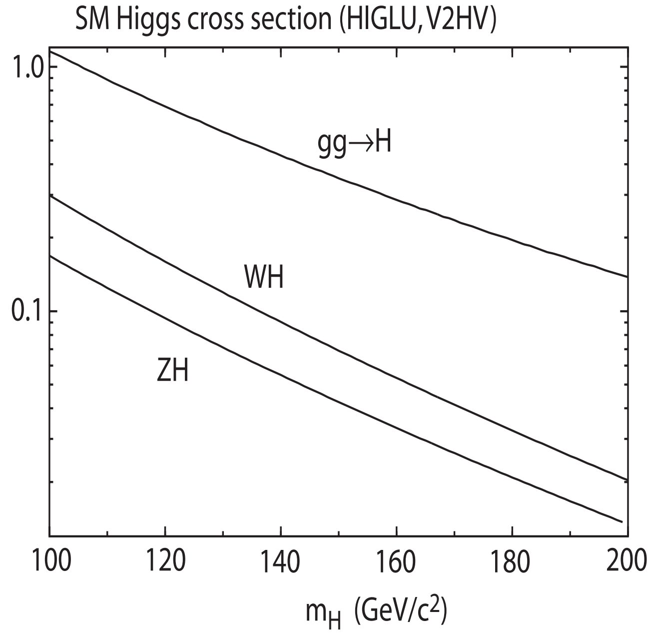

Figure 2.2 The NLO Higgs boson production cross section for $gg \to H$, $q\bar{q}' \to WH$, and $q\bar{q} \to ZH$ processes as a function of Higgs boson mass at the TEVATRON ($p\bar{p}$ collision, $\sqrt{s} = 1.96$ TeV).

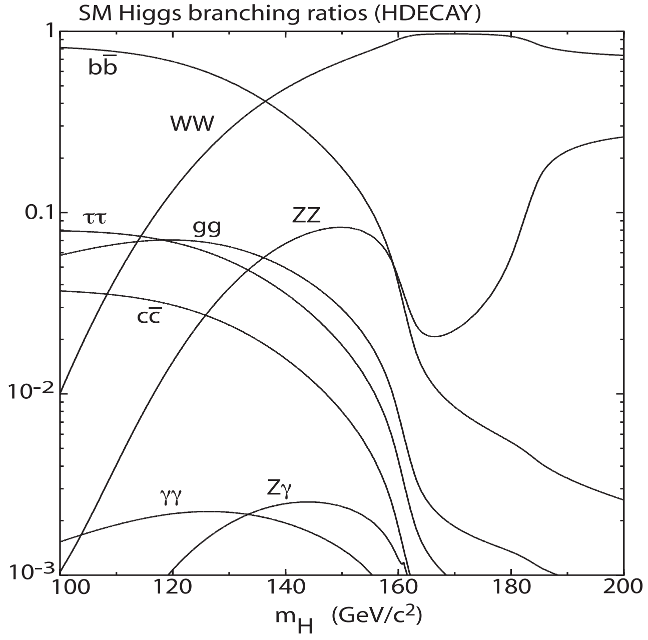

Figure 2.3 The branching ratio for each Higgs boson decay mode as a function of Higgs boson mass.

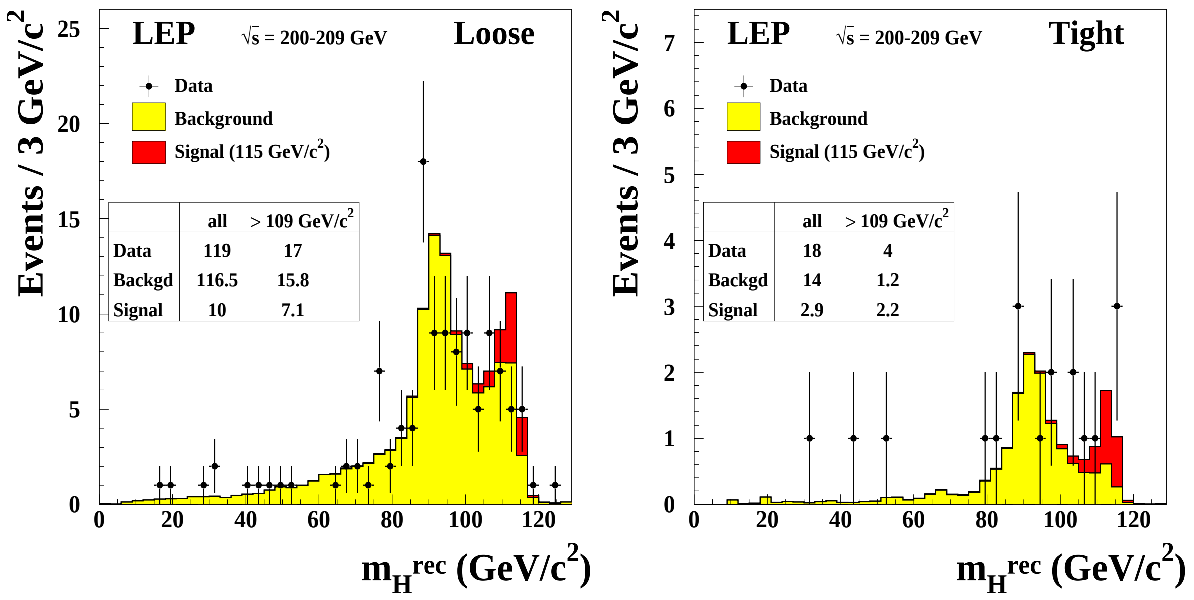

Figure 2.4 Distributions of the reconstructed Higgs boson mass obtained from two selections with differing signal purities. The histograms show the Monte Carlo predictions, lightly shaded (yellow) for the background, heavily shaded (red) for an assumed the Standard Model Higgs boson of mass 115 GeV/c^2, together with data.

2.5 Searches for Higgs Boson in the Past

2.5.1 Direct Search at LEP

The LEP performed a search for the Standard Model Higgs boson production in e^+e^- collisions with an integrated luminosity of 2461 pb^{-1} at center-of-mass energies between 189 and 209 GeV/c^2[6]. The most sensitive Higgs Production process at LEP is $e^+e^- \to ZH$, where Higgs boson decays to bottom quark pair and Z^0 decays to all possible final states. The reconstructed dijet mass distributions are shown in **Fig.2.4**. The Standard Model background expectation and observed data are consistent each other. Finally, the possibility of the Higgs boson mass is excluded as:

$$m_H > 114.4 \mathrm{GeV/c}^2, \tag{2.22}$$

at 95% confidence level (C.L.).

2.5.2 Indirect Search

The presence of Higgs boson has meaningful effects on many electroweak parameters, and it makes the electroweak theory renormalizable. The one loop effect from top quark and

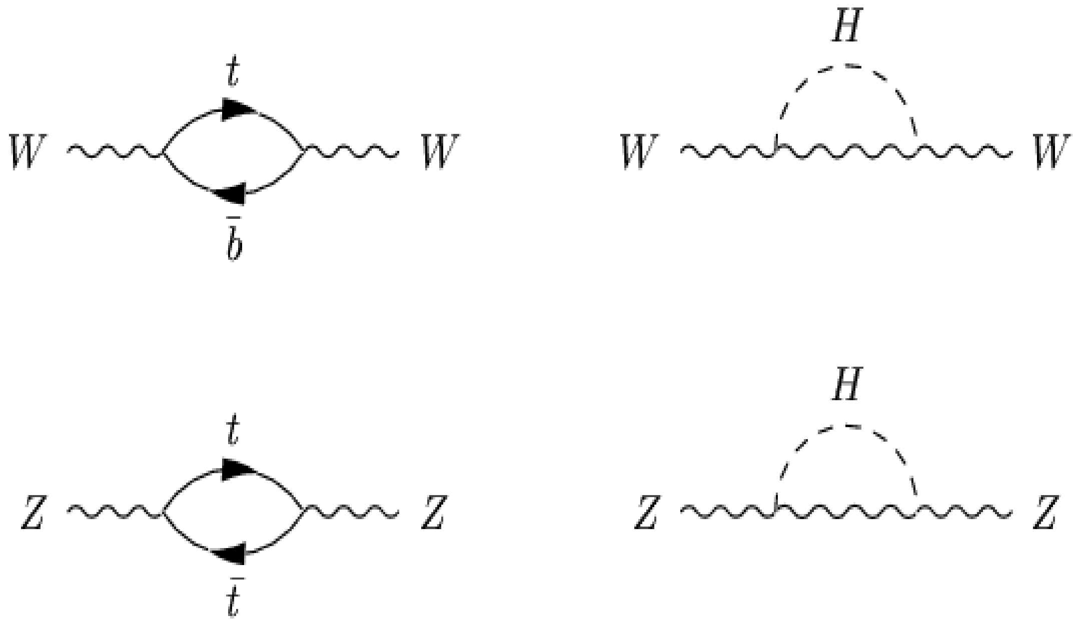

Figure 2.5 Contributions of self-coupling loops to higher order electroweak processes.

Higgs boson to W and Z bosons are shown in **Fig.2.5**. A parameter of ρ,

$$\rho = \frac{M_W^2}{M_Z^2}(1 - \sin^2\theta_W) \equiv 1 + \Delta r, \tag{2.23}$$

relates the W and Z boson mass and Weinberg angle. Δr is a radiative correction from M_t and M_W written as

$$\Delta r = \frac{3G_F}{8\pi^2\sqrt{2}}M_t^2 + \frac{\sqrt{2}G_F}{16\pi^2}M_t^2\left[\frac{11}{3}\ln\left(\frac{M_H^2}{M_W^2}\right) + \cdots\right] + \cdots. \tag{2.24}$$

One can infer the Standard Model Higgs boson mass from the precise measurements of top quark and W boson mass under the assumption that the Standard Model is the correct theory of nature[15]. The precise measurements of those particles from TEVATRON, LEP2, LEP1 and SLD are summarized in **Fig.2.6**. The relationships between top quark, W and Higgs boson are shown in **Fig.2.7**. The Standard Model relationship for the mass of top quark and W boson as a function of the Higgs boson mass is also shown. The arrow labeled $\Delta\alpha$ shows the variation of this relation if $\alpha(m_Z)^2$ is changed by one standard deviation. This variation gives an additional uncertainty to the Standard Model band shown in the figure.

Of particular interest is the constraint on the mass of the Higgs boson, because this fundamental ingredient of the Standard Model has not been observed yet. **Fig.2.8** shows the $\Delta\chi^2$ curve derived from high-Q^2 precision electroweak measurements[16, 17], per-

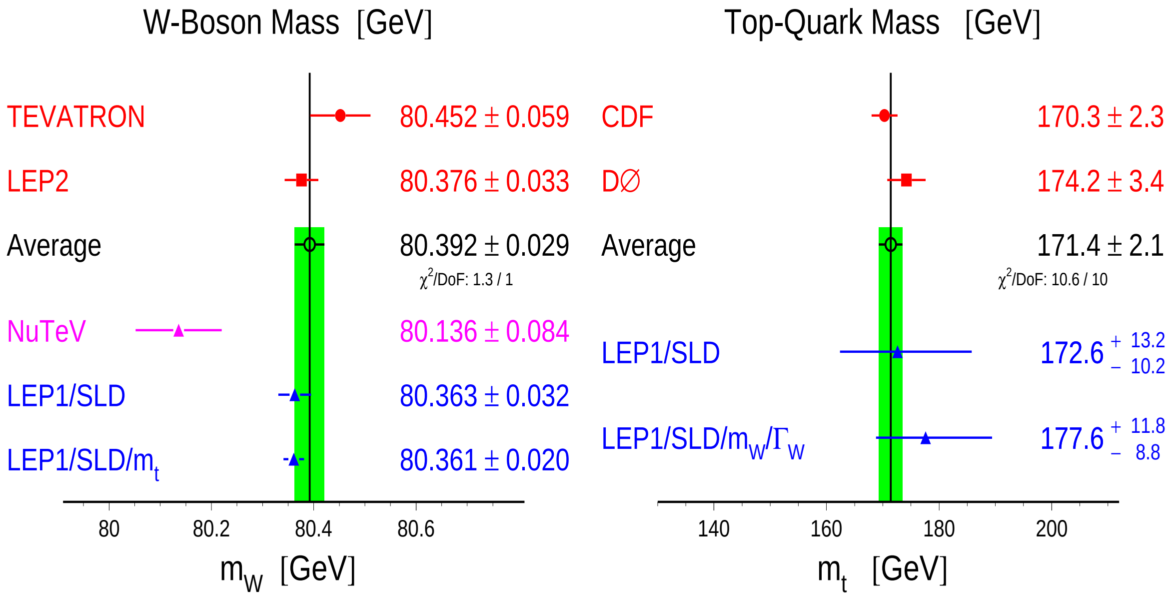

Figure 2.6 Summaries of the precision measurements of W boson mass (left) and top quark mass (right).

formed at LEP, SLD, CDF, and DØ, as a function of the Higgs boson mass, assuming the Standard Model to be the correct theory of nature.

The preferred value for its mass, corresponding to the minimum of the curve, is at 85GeV/c^2, with experimental uncertainties of +39 and -28 GeV/c^2 (at 68% C.L. derived from $\Delta\chi^2 = 1$ for the black line, thus not taking the theoretical uncertainty shown as the blue band into account). While this is not a proof that the Standard Model Higgs boson actually exists, it does serve as a guideline in what mass range to look for it. The precision electroweak measurements tell us that the mass of the Standard Model Higgs boson is lower than about 166 GeV/c^2 (one-sided 95% C.L. upper limit derived from $\Delta\chi^2 = 2.7$ for the blue band, thus including both the experimental and the theoretical uncertainty). This limit increases to 199 GeV/c^2 when including the LEP-2 direct search limit of 114.4 GeV/c^2 shown in yellow. The constraints on m_H from direct and indirect searches are summarized as:

$$114.4 < m_H < 199 \ (\mathrm{GeV/c^2}) \quad \text{at 95\% C.L.} \tag{2.25}$$

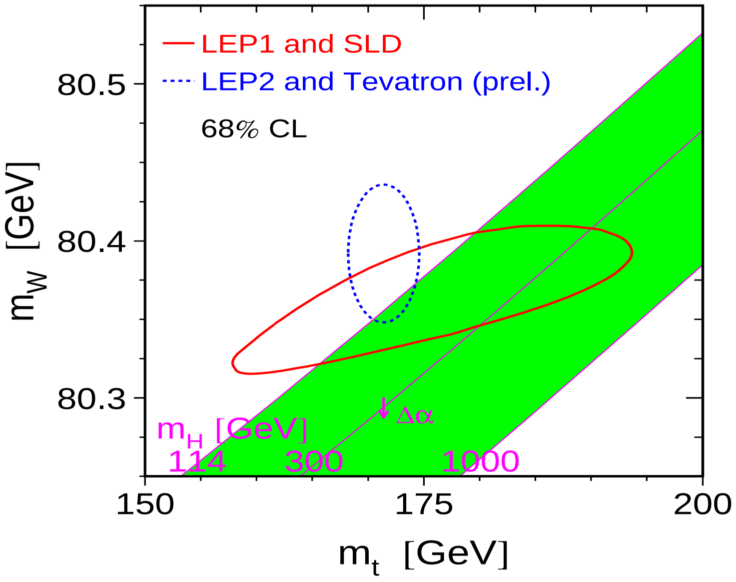

Figure 2.7 The comparison of the indirect measurements of m_W and m_t (LEP-I+SLD data) (solid contour) and the direct measurements ($p\bar{p}$ colliders and LEP-II data)(dashed contour). In both cases the 68% C.L. contounrs are plotted.

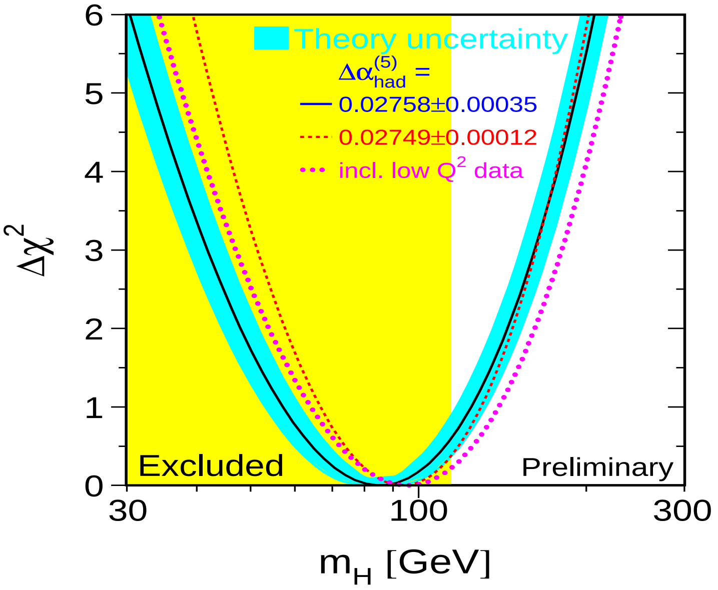

Figure 2.8 $\Delta\chi^2 = \chi^2 - \chi^2_{\mathrm{min}}$ vs Higgs boson mass m_H. The line is the result of the fit. The band represents an estimate of the theoretical error due to missing higher order corrections. The vertical band shows the 95% C.L. exclusion limit on m_H from the direct search. The dashed curve is the results obtained using the evaluations of $\Delta\alpha^{(5)}_{\mathrm{had}}(M_Z^2)$.

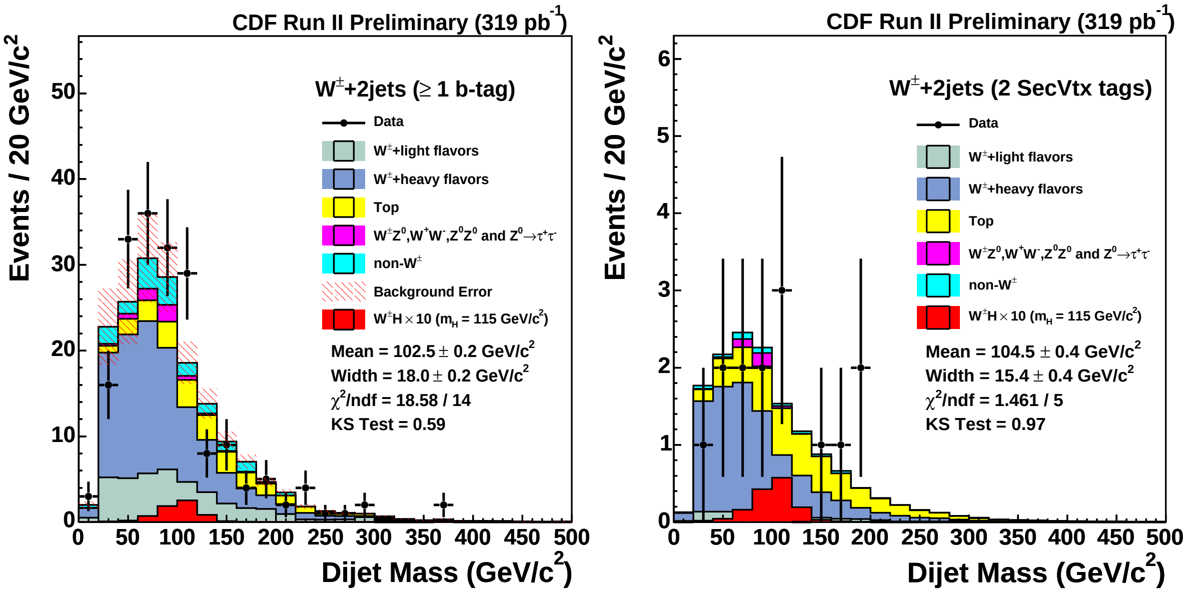

Figure 2.9 The dijet mass distributions in lepton ($e^{\pm}/\mu^{\pm}$)+ missing transverse energy+ two jets events including at least one(left) or two(right) b-tagged jets in CDF RUN2 experiment with 319 pb^{-1}.

2.6 Previous Searches at the TEVATRON

2.6.1 Search for $WH \to \ell\nu b\bar{b}$ at CDF RUN2

A search for $WH \to \ell\nu b\bar{b}$ was performed in CDF RUN2 experiment[8, 9]. The analysis used the data collected between February 2002 and August 2004, which is corresponding to an integrated luminosity of 319 pb^{-1}. The analysis used events including high p_T electron or muon, large missing transverse momentum and two jets with at least one of the jets identified as b-quark. The dijet mass distributions for at least one or two b-tagged events are shown in **Fig.2.9**. The Standard Model background expectation and observed data were consistent each other. The constraint on the WH production cross section times branching ratio of $H \to b\bar{b}$ was obtained as shown in **Fig.2.10**, e.g. $\sigma(p\bar{p} \to WH) \cdot Br(H \to b\bar{b}) < 10$ pb at $m_H = 110$ GeV/c^2 and < 2.8 pb at 150 GeV/c^2 as a function of Higgs boson mass. This thesis is based on the previous analysis. Starting from the previous analysis, we improve techniques for the search and use the full data set obtained up to the point of this thesis.

2.6.2 Search for $WH \to \ell\nu b\bar{b}$ at DØ RUN2

DØ collaboration has also performed a search for $WH \to \ell\nu b\bar{b}$ in the TEVATRON RUN2 experiment[18]. Their latest result is obtained from the data collected by DØ

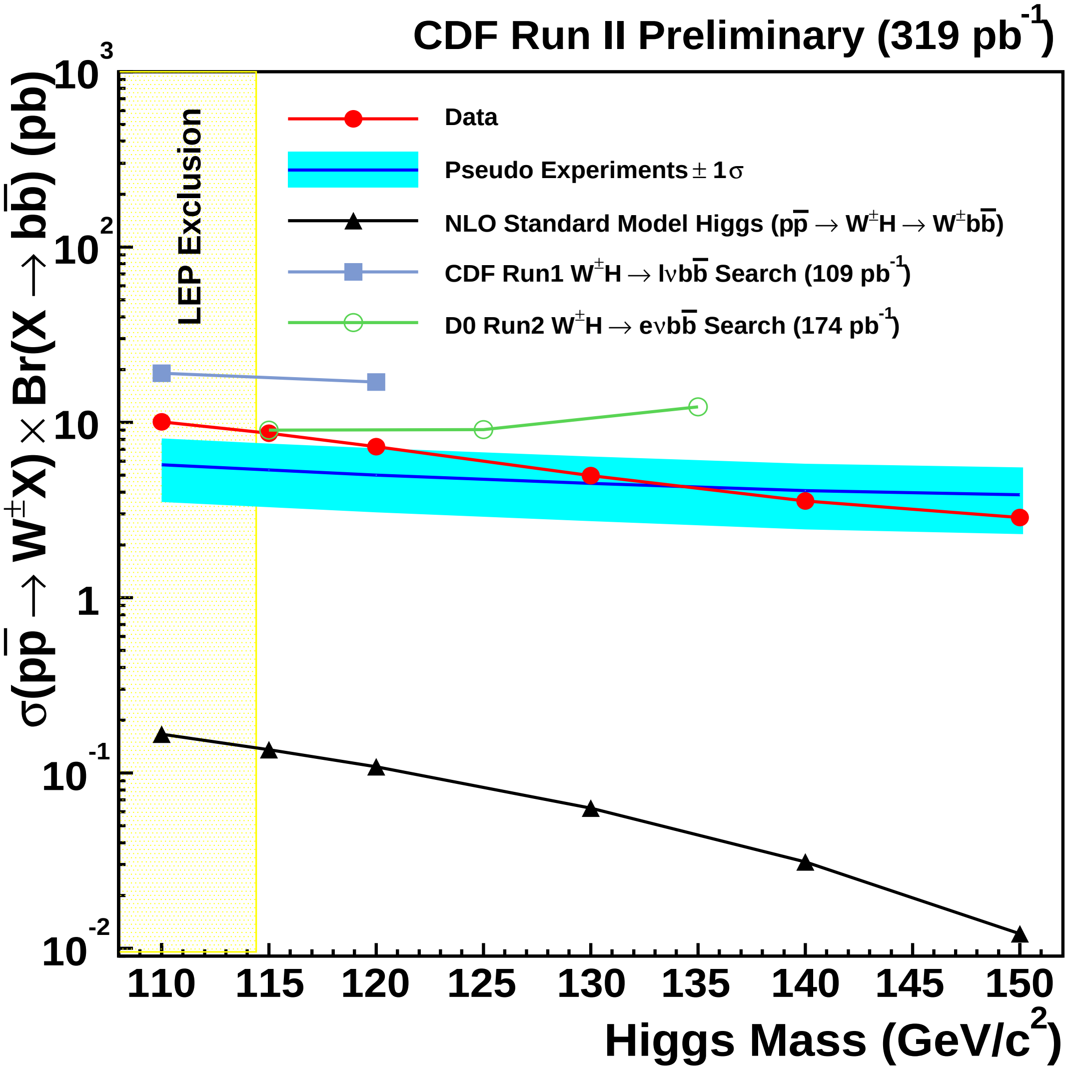

Figure 2.10 The constraint on the production cross section times branching ratio corresponding to $WH \to Wb\bar{b}$ process obtained in lepton$(e/\mu)+$ missing transverse energy$+$ two jets with at least one b-tagged jet in CDF Run2 data (319pb^{-1})

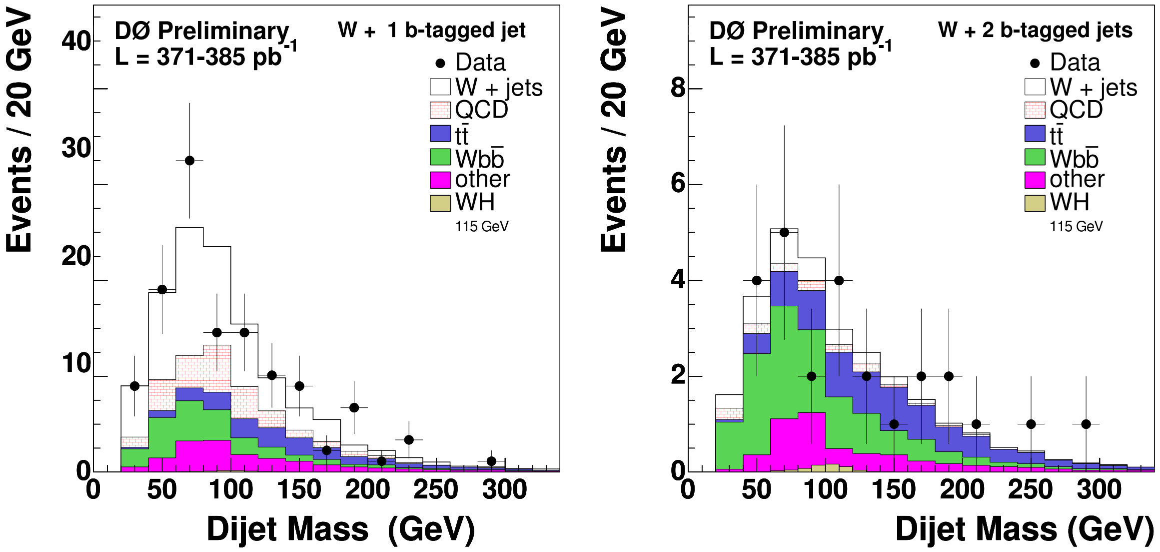

Figure 2.11 The dijet mass distributions in lepton($e^{\pm}/\mu^{\pm}$) + missing transverse energy + two jets events including exactly one b-tagged jet(left) or at least two b-tagged jets(right) in DØ RUN2 experiment with 378 pb^{-1}.

detector, which is corresponding to an integrated luminosity of 378 pb^{-1}. The dijet mass distributions obtained from $W + 2$ jet events with exactly one b-tagged jet and at least two b-tagged jets are shown in **Fig.2.11**, which do not show any significant excess indicating WH production. Accordingly, the limit on the WH production cross section times $H \rightarrow b\bar{b}$ branching ratio is set at 95% C.L. as shown in **Fig.2.12**.

2.6.3 Other Higgs Boson Searches at the TEVATRON

Many other searches for the Standard Higgs boson production were performed in addition to $WH \rightarrow \ell\nu b\bar{b}$ both in CDF and DØ collaborations. No evidence of the Standard Model Higgs boson production were obtained in all of the searches at present. The constraints on the production cross section times branching ratio at 95% C.L. for those processes were obtained and summarized in **Fig.2.13**.

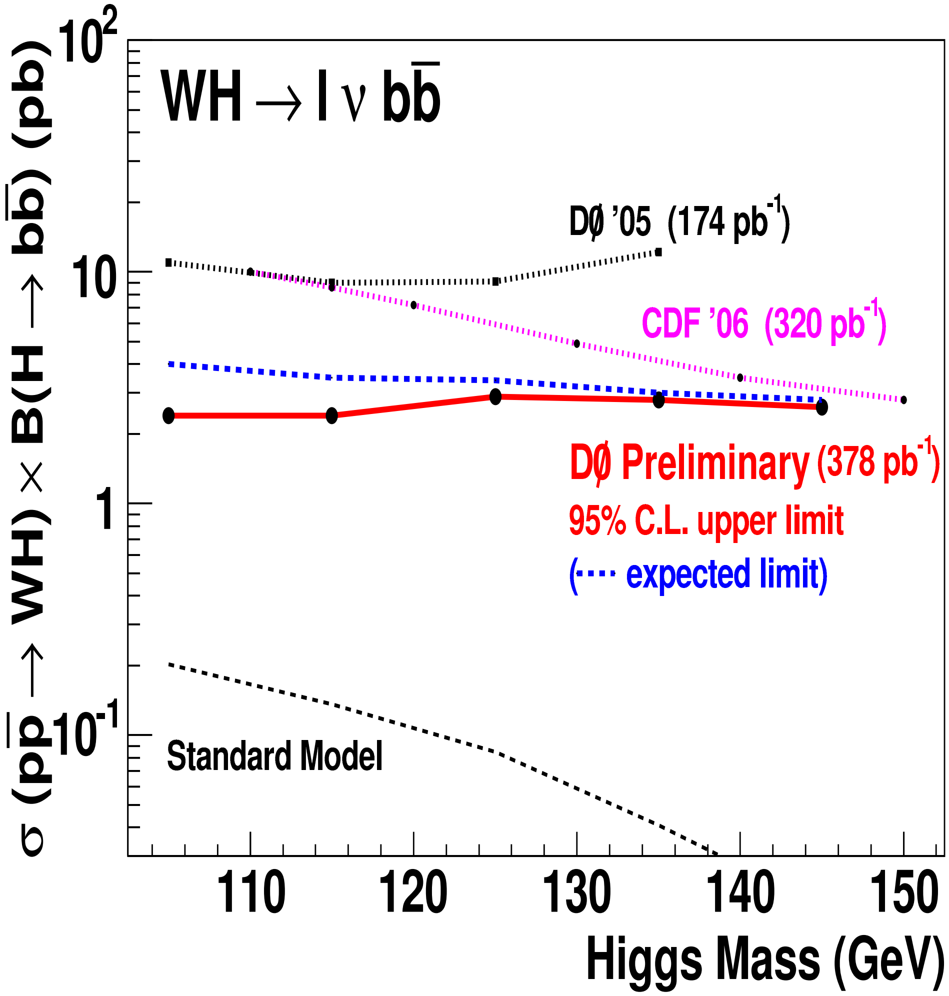

Figure 2.12 The constraint on production cross section times branching ratio corresponding to $WH \rightarrow Wb\bar{b}$ process obtained in lepton($e^{\pm}/\mu^{\pm}$) + missing transverse energy + two jets. The limit is extracted by the combined use of exactly one b-tagged and at least two b-tagged events using DØ RUN2 data of 378pb $^{-1}$

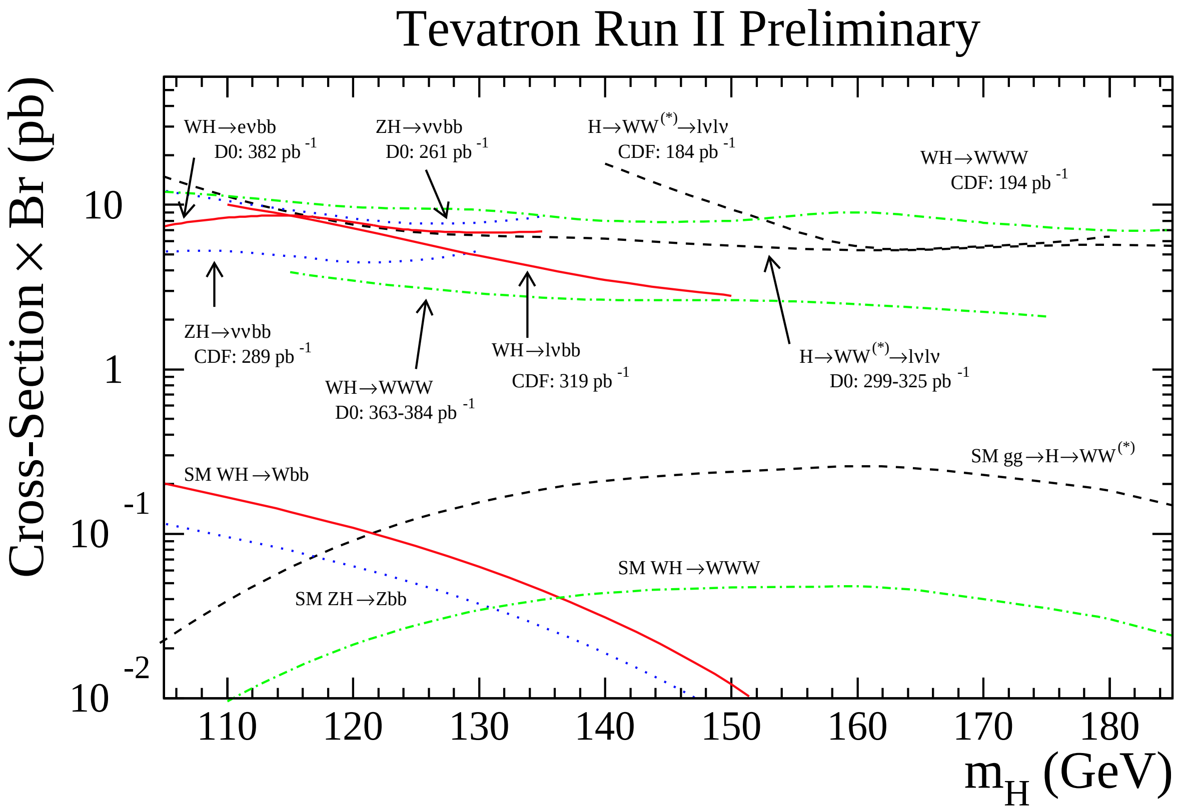

Figure 2.13 Summary of the constraints on the Standard Model Higgs boson production cross section times branching ratio for each process at 95% C.L. obtained in TEVATRON RUN2 experiment up to winter 2005.

Chapter 3

Experimental Design

The TEVATRON is the accelerator with the largest energy in the world currently. The analysis uses the data collected between February 2002 and February 2006 in proton-antiproton collisions at $\sqrt{s} = 1.96$ TeV by the Collider Detector at Fermilab (CDF) in the TEVATRON RUN2 experiment. The experimental aspects are described in this chapter.

3.1 Accelerator Complex

The Accelerator complex at Fermilab consists of several key components, that can be conceptually separated into a series of accelerators that prepare the protons, produce and store anti-protons and finally accelerate both protons and antiprotons to $\sqrt{s}$ =1.96 TeV and orchestrate the collisions. The schematic view of the accelerator chain is shown in **Fig.3.1**.

3.1.1 Proton Source

The Pre-accelerator is a linear accelerator that produces negative hydrogen ions and accelerates them to 750 keV simply by applying the electric field to the ionized hydrogen. The output frequency is 15 Hz and the resulting H^- ions then enter into the Linac or Linear Accelerator. The Linac is the next step in the acceleration process. It takes negatively charged hydrogen ions from 750 keV to 400 MeV. The Linac also operates with 15 Hz frequency. The modes of operation include feeding the beam to the Booster, feeding the beam to the Nuclear Therapy Facility or simply dumping the beam into a concrete block. The Booster is the first circular accelerator in the proton accelerator chain. It has a radius of 75 meters and consists of alternating magnets and RF cavities. The Booster strips electrons of the H^- ions and accelerates the protons from 400 MeV to 8 GeV. The

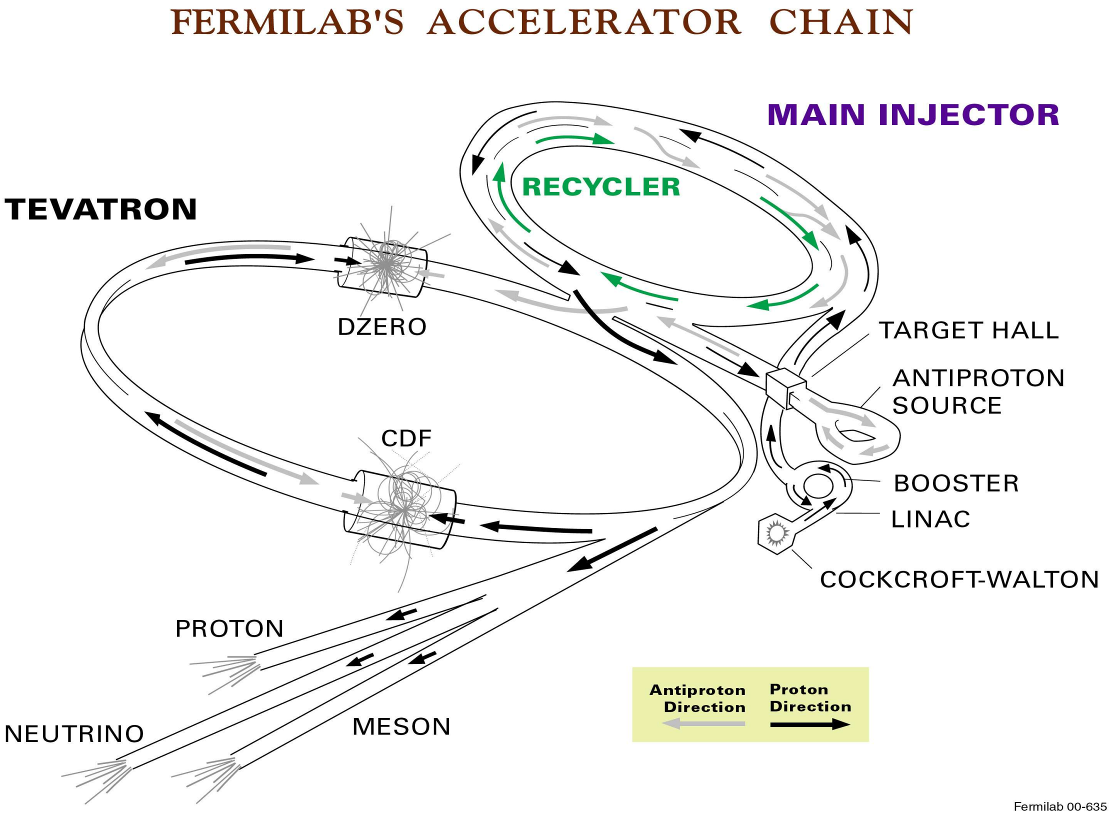

Fermilab 00-635

Figure 3.1 Schematic view of the TEVATRON accelerator complex.

RF cavities apply the accelerating field while the magnets apply the bending field to keep protons in the circular orbit and ramp it up in accordance with the instantaneous energy of the beam.

The Main Injector is a circular accelerator that serves several purposes. For one, it accelerates the protons that transported from the Booster from 8 GeV to 150 GeV. In another mode of operation the Main Injector stacks the antiprotons and accelerates them to 120 GeV. The circumference of this machine is seven times that of the Booster and it is able to accelerate beam every 2.2 sec.

3.1.2 Antiproton Source

The production of the antiprotons is a technologically challenging task and thus the antiprotons production and storage capacity is the main limiting factor for the colliding beams luminosity. The antiprotons are produced at the Target station when the 120 GeV proton beam coming from the Main Injector hits a nickel target. In this process many types of particles are being produced. A system of magnets is then used to separate 8 GeV antiprotons and direct them to the next stage accelerator. The purpose of the

Debuncher, a triangular synchrotron [1] machine where antiprotons are directed after being produced, is not to accelerate them but rather to make the momentum of the particles inside the beam more uniform - this process is normally referred to as "cooling" [2]. The mean radius of the Debuncher is 90 meters. The resulting 8 GeV beam of antiprotons is then delivered into the Accumulator. The Accumulator is located in the same tunnel as the Debuncher and is also a triangular synchrotron. It is used for storage and further cooling of the antiprotons.

The Recycler is a relatively recent addition to the Fermilab accelerator chain. It resides in the same tunnel as the Main Injector and is used to decelerate and cool down the antiprotons left in the TEVATRON after the store. Several different cooling techniques are used in the Recycler which serves an important purpose of improving the antiproton utilization efficiency.

3.1.3 TEVATRON

With the diameter of exactly 2 km the TEVATRON is the largest accelerators at Fermilab, and the only one that uses superconductive niobium/titanium alloy magnets which are able to create 4.2 T fields. The Tevatron is mainly a storage ring. In the so called 36×36 operation mode there are 36 bunches of protons and 36 of antiprotons circling the ring in the opposite directions. The bunches of protons and antiprotons are passing through each other, "bunch-crossing", every 396 ns.

The beams of protons and antiprotons undergo focusing via quadrupole magnets in the BØ and DØ interaction points, around which the CDF and DØ detectors are built. This is done in order to reduce the beam spot size and thus increase the instantaneous luminosity and the chance of a proton collision with antiproton.

3.2 The CDF II Detector

The Collider Detector at Fermilab, known as CDF[19, 20], is a multipurpose particle detector built around the TEVATRON BØ interaction point. It is approximately 15 meters long and 10 meters high and maintains approximate axial and forward-backward symmetries. The associated Cartesian coordinate system is defined as a right-handed basis with the z-axis set by the colliding beams and the protons moving in the positive z-direction. The x-axis points radially outwards and y-axis vertically upwards. Although occasion-

---

[1] A circular accelerator in which both magnetic field and accelerating electric field are changed synchronously as the particles are accelerated, in order to maintain the same particle orbit.

[2] Another way of looking at it is to consider cooling as a process of increasing particle density in momentum phase-space.

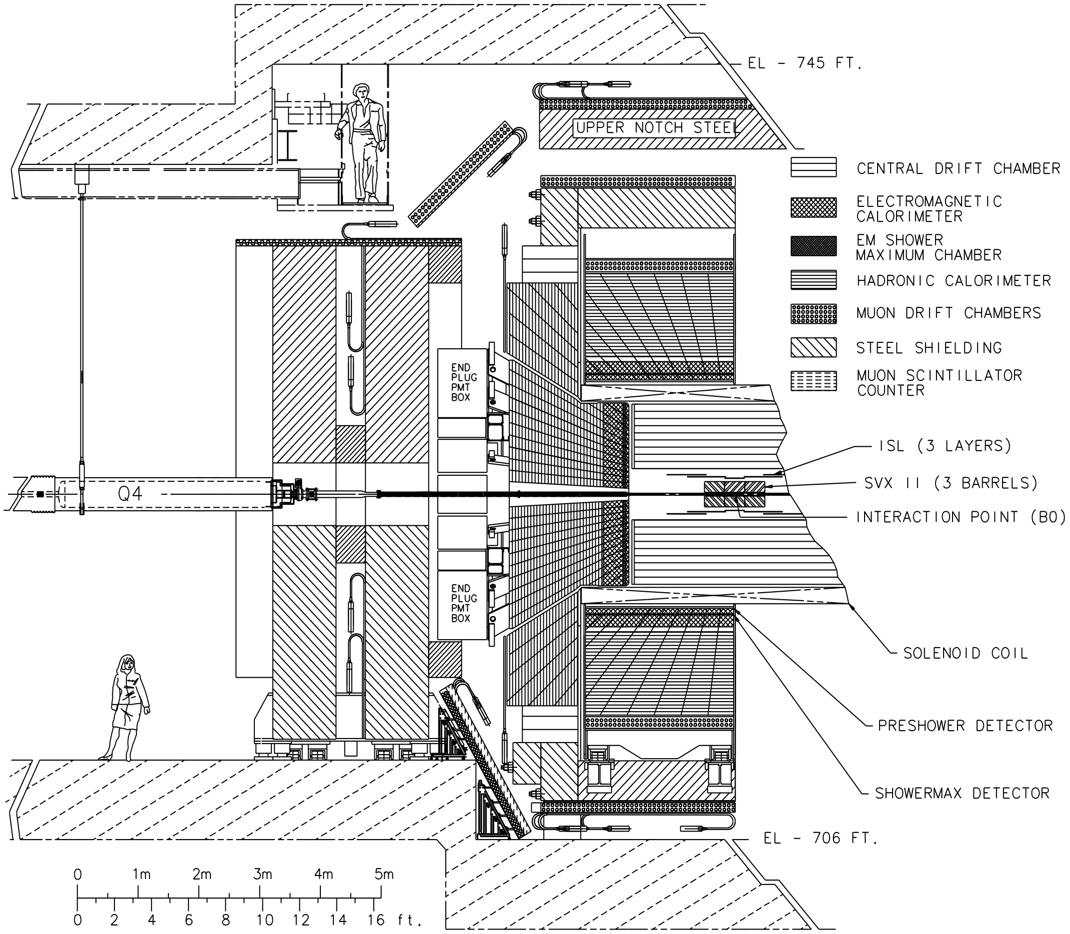

Figure 3.2 Elevation view of one half of the CDF II detector.

ally it is convenient to work in cylindrical (r, z, ϕ) or polar (r, θ, ϕ) coordinates, where the azimuthal angle ϕ is the (xy) plane angle measured from the direction of x-axis, another coordinate system is commonly used in collider physics. In this system the polar angle θ is replaced by pseudo-rapidity:

$$\eta = -\ln \tan \frac{\theta}{2}. \tag{3.1}$$

The utility of the (r, θ, ϕ) coordinate system stems from the axial symmetry of the experiment and from the nature of proton-antiproton collisions. The latter manifests itself in the fact that the interactions of colliding partons often result in considerable longitudinal momentum of the collision products. The rapidity of the system:

$$y = \frac{1}{2} \ln \frac{E + p_z}{E - p_z}, \tag{3.2}$$

transforms under boosts along the z-axis as $y' = y + \tanh^{-1}\beta$ and thus Δy are invariant under such transformations. The pseudo-rapidity is the relativistic or massless approximation to the real rapidity of the system:

$$\eta = \frac{1}{2}\ln\frac{p+p_z}{p-p_z} = -\ln\tan\frac{\theta}{2}. \tag{3.3}$$

Many detector components are segmented uniformly in η and ϕ . Typically the pseudo-rapidity η refers to "detector η" determined with respect to center of the detector coordinate system. The η can also be determined with respect to the point where the interaction took place (in that case it is called "event η").

After each collision the particles that were produced in the interaction traverse through various detector subsystems. The first one they encounter is the tracking system, then calorimetry and finally the muon sub-detectors. These are the basic components that provide the data that serves as the foundation of our measurement. The schematic overview of the CDF detector is shown in **Fig.3.2**.

3.2.1 Tracking System

The CDF tracking system consists of the Central Outer Tracker(COT)[21] and silicon detector subsystem that in turn consists of Silicon VerteX detector(SVX), Intermediate Silicon Layers(ISL) and Layer 00(L00) [22–24].

The entire tracking volume resides inside a superconducting solenoid magnet with the radius of 1.5 meters and the length of 4.8 meters. It creates uniform magnetic field of 1.4 T along the direction of the z-axis. The trajectory of a charged particle in magnetic field is a helix. From the parameters of this helix the particle momentum can be determined, as the magnitude of the magnetic field is known. The schematic view of the CDF tracking system in the (r-z) plane is shown in **Fig.3.3**. The region of the detector with $|\eta| < 1.0$ is referred to as "central region".

As can be seen in **Fig.3.3** a charged particle that is produced in the rapidity interval has to travel through the entire COT tracking volume and thus has a better transverse momentum measurement than a particle with $|\eta| > 1.0$. The region $1.0 < |\eta| < 3.6$ is called "plug" or "forward". The first sub-detector that a particle created in a collision transverse is the Silicon detector. The main part, SVX, consists of three cylindrical barrels placed end-to-end in Z; each is 29 cm long with five layers of double sided micro-strip silicon wafers. It occupies the space between 2.5 and 10.7 cm. The technology used allows the measurement of the ionization induced by a charged particle traversing the silicon wafer, the "hit" position, to be measured with the precision of 12 μm. The

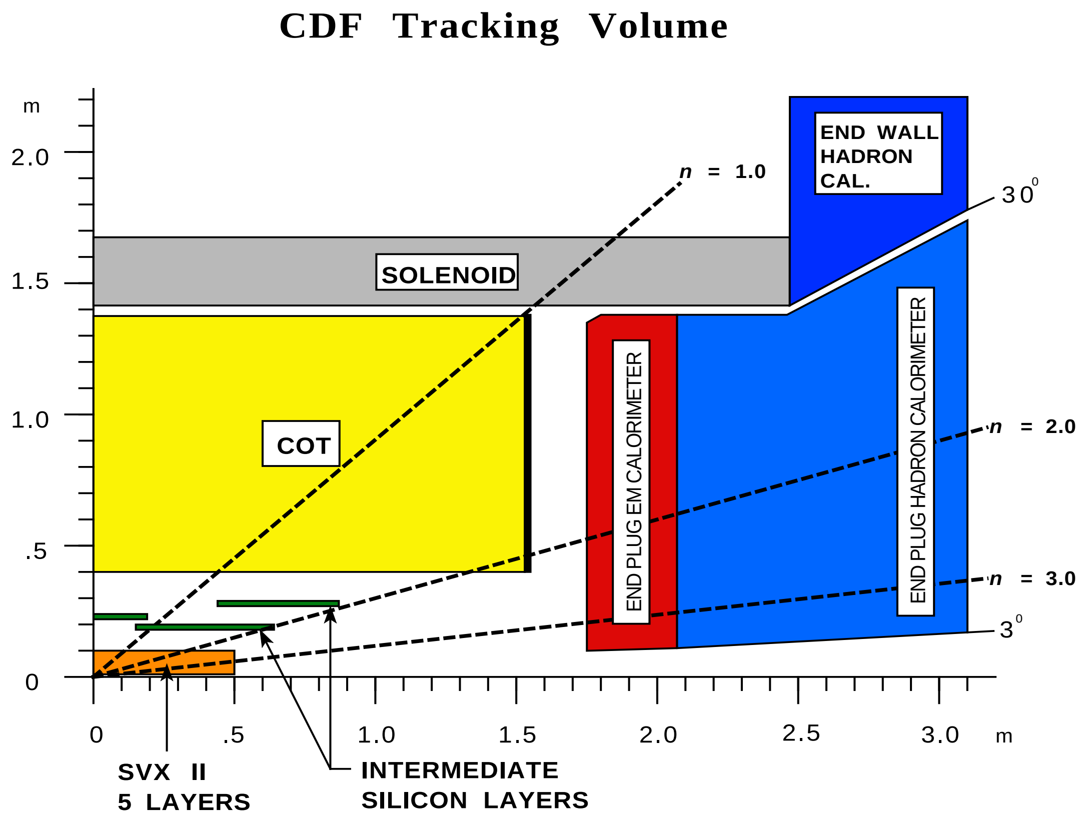

Figure 3.3 The CDF tracking system.

double-sided silicon microstrips that are used in SVX are arranged so that one side of a chip has axial[3] strips, while the other side hosts either 90° stereo[4] strips or small angle 1.2 stereo[5] strips. Such an arrangement makes it possible to combine the (r-ϕ) and (r-z) measurements into a three dimensional position measurement.

Both the ISL and L00 are the extensions to the silicon tracking subsystem. The L00 consists of two sets of single-sided radiation-hard silicon microstrips mounted directly onto the beam pipe at radii of 1.35 and 1.62 cm. It provides the position measurement closest to the interaction point. The ISL consists of several layers of double-sided silicon placed at the radii of 22, 20 and 28 cm. It is aimed at extending the tracking coverage to the region of $1.0 < |\eta| < 2.0$ as well as to provide help with resolving any ambiguities in matching COT tracks with SVX tracks in a dense-track environment.

The individual "hits" both from the COT and the silicon detectors are linked together with pattern-recognition software into a "track", the entity that describes the trajectory of a charged particle. The measure of the performance of the tracking system can be

---

[3] Strips aligned along the z-axis, providing finest granularity in (r-ϕ).

[4] perpendicular to z-axis

[5] Set at a small angle to z-direction

illustrated by the ability to determine the parameters of the helix trajectory. The resolution in the impact parameter that is achieved by the tracking system is about 40 μm, and the z_0 resolution is about 70 μm, where z_0 is the z coordinate of the closest approach to the z-axis.

The Silicon detector subsystem has 722,432 readout channels. The hit data is collected, assembled and packed for transmission by radiation hard integrated circuits. The data is transported via an optical fiber link to the external data-processing units.

Precise position measurements so close to the interaction point that are possible with the Silicon Vertex detector are used to extrapolate the tracks all the way to the collision region. It is crucial for the determination of the vertex position and provides a measurement that can distinguish a particle which is coming from a primary interaction from a particle which was produced at a displaced secondary vertex and decay products of another long lived particle.

After a charged particle exits the Silicon detector it passes through the Central Outer Tracker. The COT occupies the region with $|z| < 155$ cm and $44 < r < 132$ cm. It is a cylindrical multi-wire open-cell drift chamber filled with Argon-Ethane gas mixture, which was chosen as it provides fast drift velocity. This design constraint, in turn, stems from the need to avoid event pileup; consequently the maximum drift time is required to be less than 396 ns. The gas mixture used has the maximum drift time of about 50 ns in the drift field of roughly 2 kV/cm.

The COT consists of 30,240 sense wires grouped into eight superlayers. The superlayers alternate between axial and stereo, with the latter having the wires strung at $\pm 2^\circ$ with respect to the axial direction. Each charged particle that escapes the COT traverses 96 layers of sense wires that ideally can provide the same number of position measurements. The single hit resolution of the COT is about 140 μm. The track reconstruction software converts the individual hits into the fitted particle trajectories, the helix parameters of which allow the measurements of charged particle momenta. It results in the transverse momentum resolution of:

$$\frac{\sigma_{p_T}}{p_T} = 0.0015 \times p_T (\mathrm{GeV/c}). \tag{3.4}$$

Whenever possible the hit information from both the COT and the Silicon detector are combined to produce the best track fit. For the particles with very high momenta the parameters of a track are harder to determine precisely as the curvature of the helix is quite small. Fortunately for some of the particles, in particular, electrons, an additional measurement of their energies is possible via the Calorimetry subsystem.

3.2.2 The Calorimetry

Charged particles with energies greater than 350 MeV may leave the tracking volume and propagate beyond the solenoid magnet that surrounds it. Neutral particles, both photons and neutral hadrons, leave the tracking volume undetected. Even if they were seen by the tracking system no information about their momenta would be available for a quite obvious reason – their trajectories do not bend in magnetic field. In many of cases the measurement of their momenta is essential for the understanding of observed events. The calorimetry subsystem serves the purpose of filling this gap and is based on the fact that as particles that have reasonably high electromagnetic or hadronic interaction cross sections propagate through matter they transfer their energy to the medium until eventually all of it is absorbed. Some media produce measurable response to such energy depositions by emitting light in amounts dependent on the amount of energy lost by the particles.

The CDF calorimetry system[25, 26] consist of alternating layers of scintillator and absorber material. As particles interact with absorber they produce cascades of particles or "showers" that penetrate the scintillator. The light from the latter is guided into the photomultipliers. Their response is in turn digitized and with the help of relevant calibrations converted into the measurement of the deposited energy.

All the calorimeters are divided into segments or "towers" in such a way that the division boundaries between them point at the interaction point. The entire calorimetry system consists of two regions, central and forward; the later is also known as the "plug". The central calorimeters cover the region of 2π in ϕ and as far as $|\eta| < 1.0$ in pseudo-rapidity. They are segmented into the "towers" of $0.11 \times 15^\circ$ in $\eta \times \phi$. The Central ElectroMagnetic (CEM) part consists of alternating layers of lead absorber and polystyrene scintillator, while the Central HAdronic part (CHA) uses thicker steel plates as the absorber. The CEM is $18X_0$ radiation lengths thick, while the CHA is around $4.5\lambda_0$ attenuation lengths thick. The energy resolution of the CEM is estimated to be:

$$\frac{\sigma_E}{E} = \frac{13.5\%}{\sqrt{E_T}} \oplus 2\%, \tag{3.5}$$

where notation $\oplus$ means that the constant part is added in quadrature. The CHA resolution is estimated to be:

$$\frac{\sigma_E}{E} = \frac{50\%}{\sqrt{E_T}} \oplus 3\%. \tag{3.6}$$

The CEntral Shower-maximum (CES) and Central Pre-Radiator (CPR) detectors are also considered as a parts of the calorimetry system. The CES is a gas multiwire proportional chamber with cathode strips that provide measurements of the z-position and anode wires that allow a measurement of the ϕ of the energy deposition. The chamber is embedded into the CEM at about $5.9X_0$ where the maximum of electromagnetic energy deposition occurs. The position resolution in both directions is around 2 mm. The CPR consists of proportional chambers placed between the solenoid and the calorimeter. These two subsystems, CES and CPR, provide both position measurement that helps in matching energy depositions to tracks and in shower profile measurements (information used in particle identification to distinguish between $e^{\pm}/\gamma$ and γ/π_0).

It should be noted that the segmentation of the calorimeters is rather large and thus it is quite possible that the energy measured by a particular tower was contributed to by multiple particles. Occasionally this poses a problem as the energies of the individual particles can not be determined. In other situations, most notably when a ”jet” of particles that results from hadronization of a quark or gluon coming directly from hard scattering hits the calorimeter, the total energy of all component particles is exactly the information that is needed.

3.2.3 The Muon System

Muons are 200 times heavier than electrons, so they lose substantially less energy due to electromagnetic interactions as they travel through the calorimeter material. This allows the muons to pierce through the calorimetry subsystem after they exit the tracking volume. The CDF muon subsystem consists of several chambers that are located outside of the calorimeters and includes Central MUon detector (CMU), Central Muon uPgrade (CMP), Central Muon eXtension (CMX)[27, 28]. Due to space and design constraints, the muon coverage is incomplete. **Fig.3.4** shows the ϕ-η regions that are instrumented.

The CMU is comprised of series of rectangular drift cells four layers deep. The hits registered in at least 3 out of 4 layers form a ”stub”, which after being properly matched with the corresponding COT track suggests the presence of a muon. The CMP subdetector consists of both drift chambers and scintillator plates and functions similar to the CMU by providing a ”stub” that is used in muon reconstruction. The coverages of CMU and CMP partially overlap, refer to **Fig.3.4**. The CMP is placed behind additional 60 cm of steel and thus is less sensitive to remnant hadrons that penetrate through CHA(punch-through hadrons). The CMX subsystem, like CMP, combines drift cells and scintillator plates arranged in semi-conical arches that cover the pseudo-rapidity region of $0.6 < |\eta| < 1.0$.

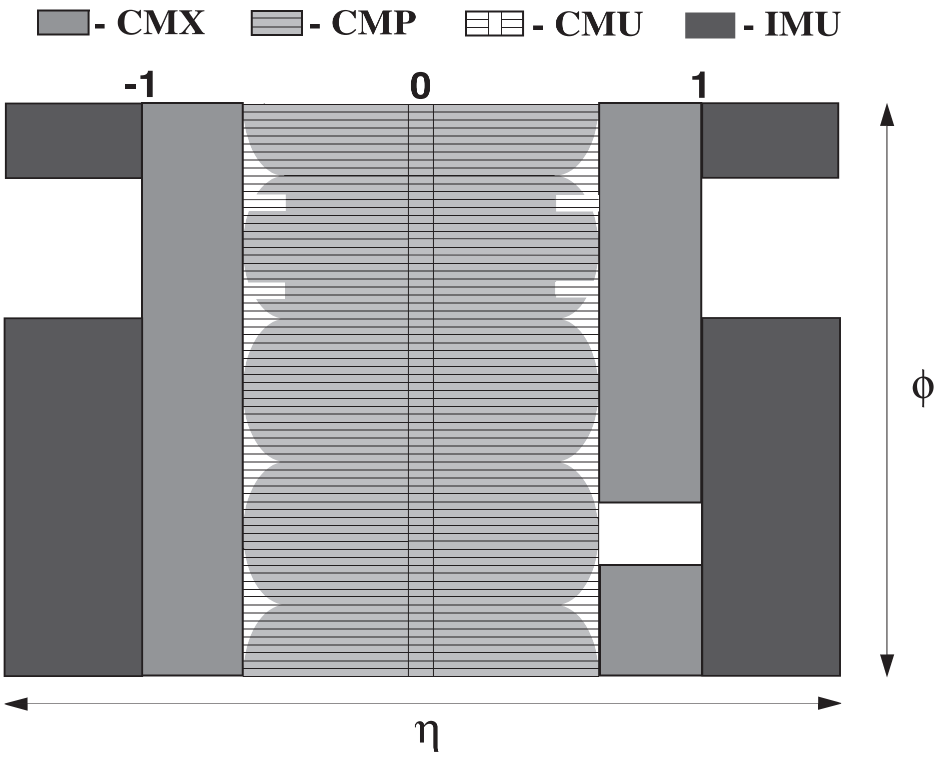

Figure 3.4 η and ϕ coverage of the CDF muon system.

3.3 Data Acquisition and Trigger

A schematic view of the CDF Data Acquisition(DAQ) and trigger system is given in **Fig.3.5**. The trigger plays an important role to efficiently extract the most interesting physics events from the large number of minimum bias and background events and to reduce the amount of data to a reasonable volume. A huge rejection already at trigger level is essential to retrieve the high statistics needed for the search for new physics.

The CDF trigger is a three level system. The time available for event processing increases in each level of the trigger which permits the use of an increasing amount of information to either accept or reject an event. While Level-1 and Level-2 triggers are based on only parts of the detector information, the Level-3 triggers makes use of the complete event data. A signal is defined as an event where a variable (for instance the energy in the calorimeter) lies above a certain trigger threshold. A list of quantities that can be cut on at the different trigger levels is given in[29]. L1 and L2 are hardware triggers while L3 is a software trigger. An optimised version of the reconstruction executable is running on a Linux PC farm with about 100 nodes. The design processing rates for Level-1, 2 and 3 are 50 kHz, 300 Hz and 50 Hz respectively. The typical event size is about 250-300 kB. The L1 triggers base their decisions on information of the calorimeters, the

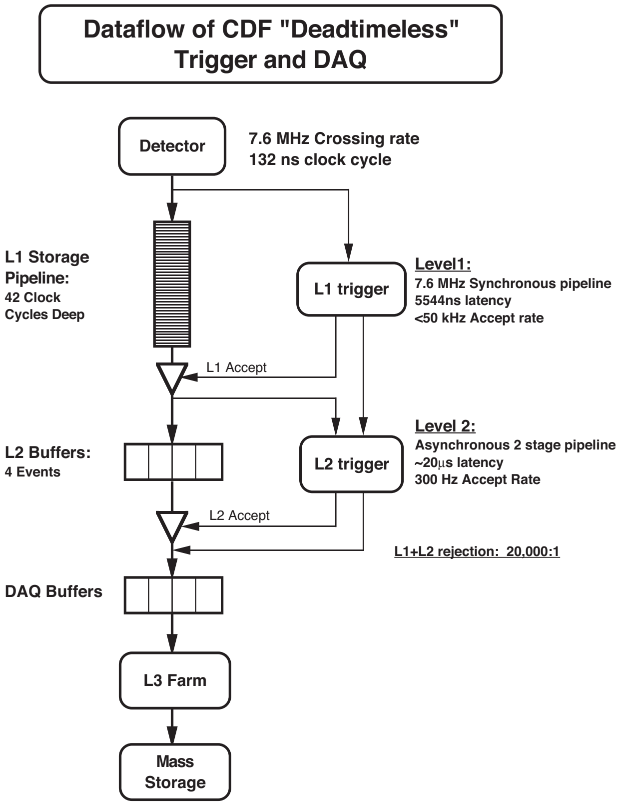

Figure 3.5 Data flow schematic of the three level pipe-lined and buffered trigger system.

muon system, the forward detectors and the drift chamber(see **Fig.3.6**). The eXtremely Fast Tracker(XFT) reconstructs r/ϕ tracks in the COT with a transverse momentum resolution of $\delta p_T/p_T^2 = 0.01651$ GeV^{-1}. and an angular resolution of 5.1 mrad.

An important feature of Level 2 is the Silicon Vertex Tracker(SVT). It adds silicon r/ϕ hits to the L1 XFT tracks. This allows to select events with two tracks having an impact parameter larger than 120 μm in order to identify secondary vertices. This will make a large number of important processes involving the hadronic decays of bottom hadrons accessible. This is of special interest for Higgs physics since for low m_H the Higgs boson predominantly decays into two bottom quarks. Full event reconstruction takes place on the L3 trigger farm and hence a wide variety of requirements can be imposed on the events passing L3[30]. Computing power on the order of one second on a Pentium II CPU is available per event. Events passing the final trigger level belong to a certain trigger path. Each "path" is a unique combination of L1, L2 and L3 triggers. The trigger decisions are combined via a logical "AND". Many paths combined by a logical "OR" can be used to feed a single data set. The data is written to approximately 20 streams and stored on tape. After reprocessing the events they are split up into more specific data sets. During measurements the data quality is monitored online[31].

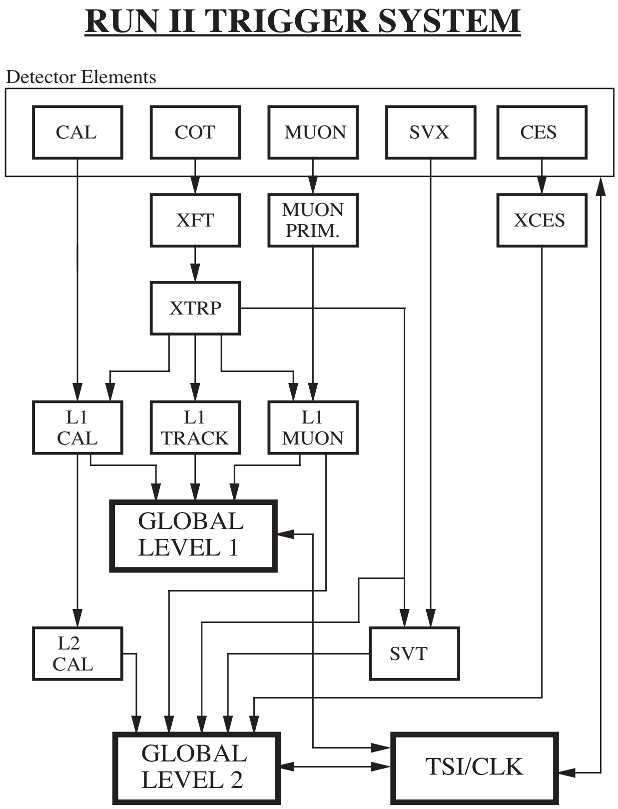

Figure 3.6 Functional block diagram of the CDF L1 and L2 trigger system.

3.4 Online Monitoring

After passing L3 triggers, Data is going to be saved in storage systems. Some of the data stream are picked up by online data validation programs, what is called “Consumer” [32] as shown in **Fig.3.7**. The data streams are arranged by Consumer Server Logger (CSL) [33, 34] to meet hardware and software requirements from up and down streams. Consumer programs consist of 13 subprograms and they are always running to check the condition of detectors and the quality of data when data taking is performed.

YMon[35]: A low level online detector diagnostic and monitor program. This generates a bunch of plots like occupancy, energy distribution, multiplicity and so on for each component of CDF detector.

XMon[36]: An online cross section monitor for each Level 1, 2 and 3 triggers.

TrigMon[37]: A low level online trigger diagnostic and monitor program. This monitors the various trigger quantities in each trigger bank looking for hot/failed channels, loose cables, trigger bits fired, bunch counter mismatches, photomultiplier spikes, and so on.

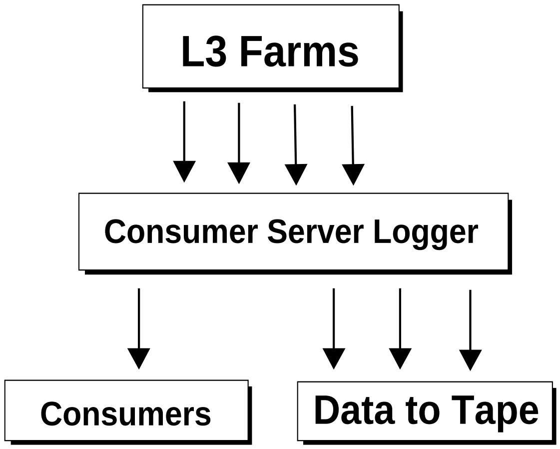

Figure 3.7 Data flow after L3 triggers.

LumMon[38]: An online monitor to see the performance of the Cherenkov Luminosity Counters (CLC) and record luminosity from CLC.

BeamMon[39]: An online monitor to find the beam line and determine some properties of the luminous region.

SVXMon[40]: The silicon monitoring program to be used for the online and offline diagnostics of the CDF silicon tracker. Its main purpose is to accumulate various statistics during data taking and to present a coherent set of silicon performance plots.

SiliMon[41]: An online monitor to evaluate the performance of the silicon system.

ObjectMon[42]: A high-level object monitor. The purpose is monitoring of Level 3 reconstructed objects as an online consumer. This also serves as a tool in the validation of the offline reconstruction of data.

Stage0[43]: An online monitor to check the detector performance after tracking system, which complements YMon.

DAQMon[44]: An online monitor to check the readout performances of almost all of the different crates in the event. This monitors the different readout time(in microseconds) and event volume(in bytes) for each crate.

DAQErrMon[45]: An online monitor to check the consistence between event record and various readout of data banks.

SVTSPYMON[46]: An online monitor to collect histograms and other monitoring data (e.g. beam position information) from the SVT Online monitoring processes running on SVT crates, reformat suitably and make them available to the people in charge of it.

PhysMon[47]: An online monitor which processes runs, file by file, and looks at things like electron, muon, photon, Z, W, J/ψ, and trigger efficiencies. Various histograms are also produced on time.

Chapter 4

b-Tagging

In this chapter, the methods of b-tagging is discussed. Physics processes that have jets in final observable particles have huge amount of QCD light flavor jets background, and searches for such a process becomes difficult to find a good sensitivity. Important physics processes that include Standard Model Higgs boson or top quarks are expected to have a large branching fraction to bottom quarks in the final state. Thereby it is critical to identify jets which are originally b-quarks as b-jets. Then enormous QCD light flavor jets are significantly removed.

Three ways of b-jets identification techniques have been developed and used in analyses in CDF by utilizing properties of b-quark. "Soft Lepton b-Tagging(SLT)" uses the lepton kinematics from the selmileptonic decay of B-meson, but the semileptonic branching ratio is about 10% level[48, 49]. "Jet Probability b-tagging(JetProb)" is going to determine how possibly jets are coming from primary vertex using impact parameter of the tracks in the jets. Then, jets that are not supposed to come from primary vertex to specific probability are assigned as b-jets[50, 51]. "Secondary Vertex b-tagging(SECVTX)" utilizes the property that b-quark shows a displaced secondary vertex. This algorithm is used in this thesis, and details are discussed in this chapter. However, the SECVTX b-tagging still have much contamination from false tags or misidentification of c as b-jet. Multivariate Neural Network(NN) technique is introduced to overcome this difficulty and improve SECVTX tagging purity for the first time, which is also discussed in this chapter as well.

4.1 Displaced Secondary Vertex b-Tagging

The b-quark has a relatively long lifetime of 1.5×10^{-12} s. This means that the B hadrons formed during the hadronization of the initial b-quark can travel a significant distance before decaying into a collection of lighter hadrons. This distance is given by

$L = \beta c\tau'$, where β is the velocity $\beta \sim 1$ and τ' is the proper life time ($\tau' = \tau\gamma$). The average transverse distance traveled by the B hadron is therefore $L_T \sim 6.8$ mm. The spot where the decay happens can be reconstructed in the micro-strip silicon detector by identifying tracks which form a secondary vertex significantly displaced from the primary $p\bar{p}$ interaction point (primary vertex).

SECVTX b-tagging is performed for all of the jets in a event by using only the tracks which are within η-ϕ distance of $\Delta R = 0.4$ for each jet. Poorly reconstructed tracks[1] are not used for SECVTX finding. To find secondary vertices, at least two tracks with good quality are necessary. Displaced tracks in jets, which are determined by impact parameter significance defined as $|d_0/\sigma_{d_0}|$ where d_0 and σ_{d_0} are impact parameter and total uncertainty from tracking and beam position measurements, are used for the SECVTX reconstruction. Secondary vertices are looked for and reconstructed by two-pass approach.

Pass 1: At least three tracks are required to pass loose selection criteria ($p_T > 0.5$ GeV/c, $|d_0/\sigma_{d_0}| > 2.0$), and secondary vertex is reconstructed out of the selected tracks. One of the tracks used in the reconstruction is required to have $p_T > 1.0$ GeV/c^2.

Pass 2: Exactly two tracks are required to pass tight selection criteria ($p_T > 1.0$ GeV/c, $|d_0/\sigma_{d_0}| > 3.5$ one of the tracks must have $p_T > 1.5$ GeV/c). Then reconstruct secondary vertex from the two tracks.

Only when **Pass 1** fails, **Pass 2** is applied. If either attempt is successful, the transverse distance L_{xy} from the primary vertex of the event is calculated along with the associated uncertainty on L_{xy}, which we denote $\sigma_{L_{xy}}$. Finally jets are tagged positively or negatively depending on $L_{xy}/\sigma_{L_{xy}}$ (L_{xy} significance)[52]:

$$L_{xy}/\sigma_{L_{xy}} \geq 7.5 \quad \text{(positive tag)} \tag{4.1}$$

$$L_{xy}/\sigma_{L_{xy}} \leq -7.5 \quad \text{(negative tag)} \tag{4.2}$$

The sign of L_{xy} indicates the position of the secondary vertex with respect to the primary vertex along the direction of the jet as illustrated in **Fig.4.1**. If the angle between the jet direction and the vector pointing from primary vertex to the secondary vertex is less than $\pi/2$, L_{xy} is positively defined. Otherwise, it becomes negative. If L_{xy} is positive, the secondary vertex points towards the direction of the jet. This is consistent with a B hadron traveling from the primary vertex in the direction of the jet. And positive L_{xy} is preferred in a realistic B hadron decays. For negative L_{xy} the secondary vertex points

---

[1] Transverse momentum, the number of silicon hits attached to the tracks, quality of those hits, and χ^2/N_{DOF} of tracks are used to determine if the track is good or poor.

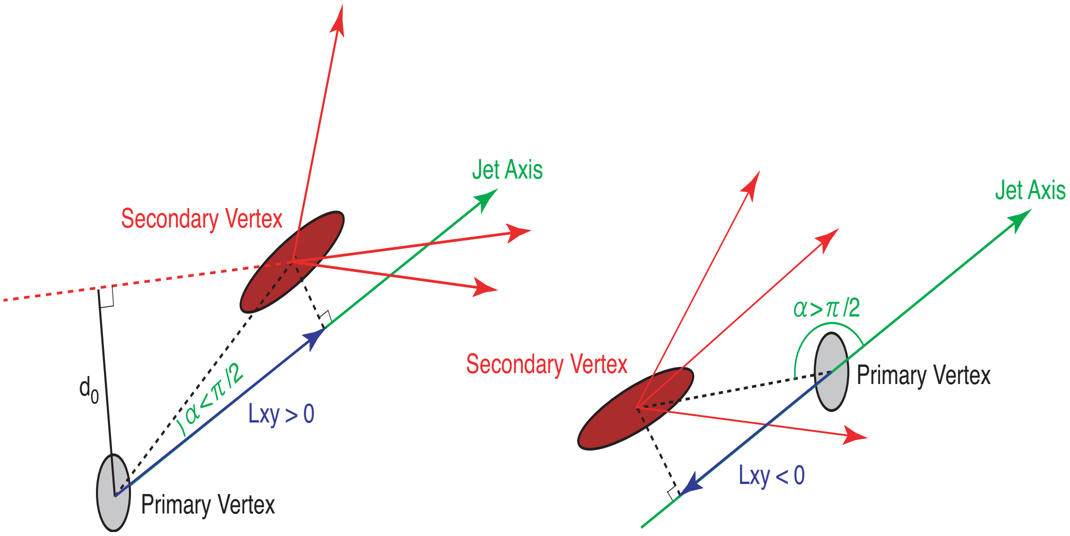

Figure 4.1 Cartoon showing true reconstructed secondary vertex ($L_{xy} > 0$, left) and fake one ($L_{xy} < 0$, right).

away from the jet which may only happen by coincidence or as a result of mis-measured tracks. Jets tagged with a negative L_{xy} are labeled mis-tagged jets. Additionally, in order to reject secondary vertices due to material interaction, the secondary vertices must satisfy the following requirements:

- **Pass 2** vertices found between 1.2 and 2.5 cm from the center of SVX[2] are vetoed.
- All vertices with a radius greater than 2.5 cm with respect to the center of the SVX are vetoed.

The negative tags are useful for evaluating the rate of false positive tags, which is denoted as "mistag" in this thesis. Mismeasurements are supposed to be randomly take places, therefore the L_{xy} distribution of fake tags is expected to be symmetric with respect to the primary vertex.

---

[2] Some care must be taken since CDF origin is taken to be the center of the COT which is not the origin of the SVX (the SVX center is shifted approximately (-1mm,+1mm) with respect to the COT origin.

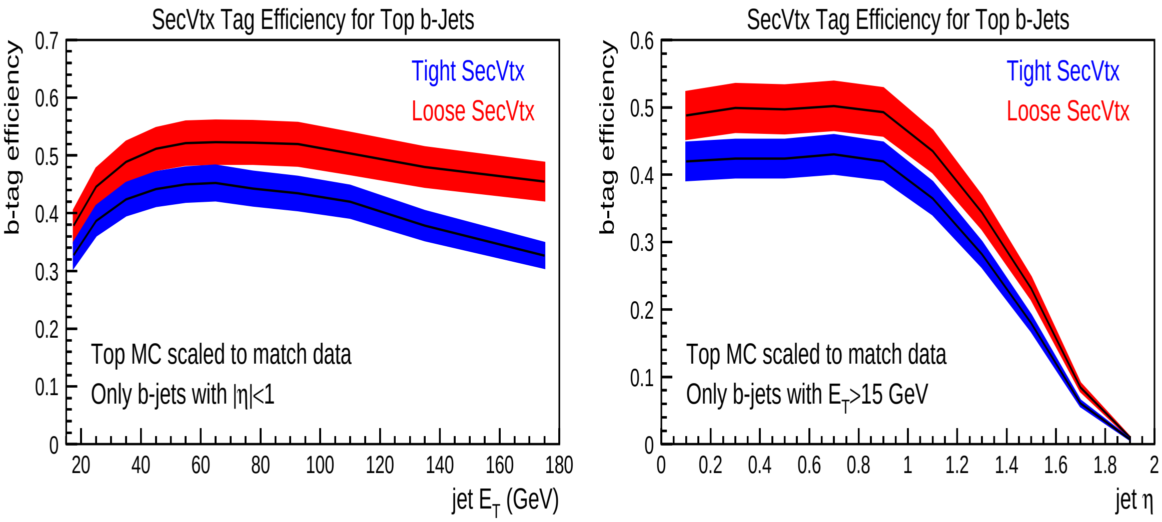

Figure 4.2 b-tagging efficiencies as functions of E_T(left) and η(right) of jets. Only the jets which were b-quarks in parton level are used for the calculation. Two SECVTX tagging conditions, "Tight" and "Loose" are shown. The bands associated with black lines are total systematic uncertainty.

b-Tagging Performance

The SECVTX b-tagging algorithm is discussed, and it is also important to see the performance of the method. b-tagging efficiencies are calculated as functions of E_T and η of jets using $t\bar{t}$ Monte Carlo(MC) sample as shown in **Fig.4.2**. Unfortunately, the b-tagging efficiency obtained from MC samples does not reflect the data. Thus this fact is compensated by taking a scale factor of $SF_{\text{btag}} = \epsilon_{\text{data}}/\epsilon_{\text{MC}}$ into account. The scale factor is obtained as:

$$SF_{\text{btag}} = 0.89 \pm 0.07. \tag{4.3}$$

This factor is obtained from the data with run number less than 190000, which is collected before Aug 2004. In this thesis, the tagging criteria discussed is called "Tight SECVTX", which was discussed above. A "Loose" condition also exist, which requires looser criteria on the tagging variables. The b-tagging efficiencies decreases as a function of jet η, due to COT coverage[3], which results in worse the tracking measurement in $|\eta| > 1$ region.

The mistag rate is also shown in **Fig.4.3**. The mistag rate increases as a function of jet E_T. It is understood that the quality of the secondary vertex reconstruction becomes worse in high-E_T region, because the resolution of tracking measurements get worse for high p_T tracks.

---

[3] Charged particles travelling $|\eta| < 1.0$ passes entire volume of COT, and it result in a good tracking measurement. Otherwise it results in worse resolution.

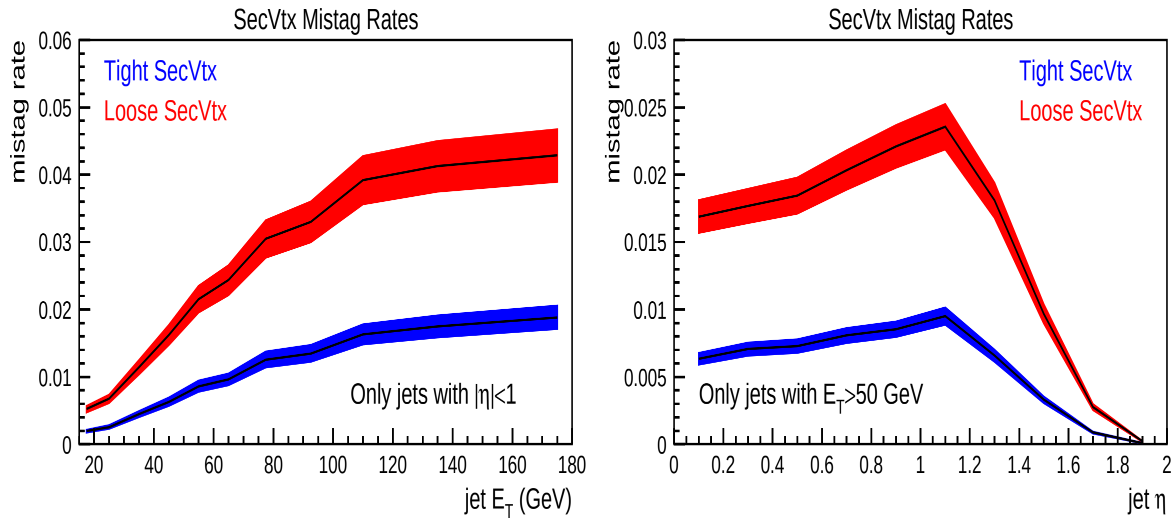

Figure 4.3 Mistag rate distributions as functions of E_T(left) and η(right) of jets. The rate is measured from inclusive jet data.

4.2 Neural Network *b*-Tagging

As discussed in previous section, SECVTX *b*-tagging put the basis on the long life time of B hadrons. D hadrons originating from c-quarks also have fairly long life time and c-jets are also tagged as b-jets frequently. Therefore b-tagged jets by SECVTX is still contaminated by falsely tagged light flavor or gluon jets or c-jets[4]. For the sake of improving the b-tagging purity, Neural Network[53] is applied for b-tagging(NNbtag) for the first time. The idea is to make the best of SECVTX tag related variables and other variables independent of SECVTX tag by combining the variables using Neural Network into two discriminant variable to separate b-jets from c and l(light flavor or gluon) jets.

The Neural Network used in the thesis is the JETNET[54] package with an interface to ROOT[55] provided by Ohio state university. The tagger is designed with two neural networks in series. One is trained to separate b-jets from l-jets, and the other, b from c. Jets which pass a cut on both of the Neural Networks outputs are accepted by the tagger. These Neural Networks are trained and applied only to events which are already tagged by the SECVTX algorithm. At present, the NN b-tagging is developed to increase the purity of the SECVTX b-tagged jets. It should be a future improvement to develop a method to increase not only purity but tagging efficiency by applying the tagger to the jets without requiring SECVTX b-tagging condition, but it is not a discussion in this thesis.

---

[4] Background estimate shown in chapter 6 implies that about 50% of the SECVTX tagged jets are from falsely tagged light flavor or gluon jets and c-jets.

SECVTX variable	SECVTX independent variable
• Number of tracks in SECVTX	• Number of good tracks
• Fit χ^2	• Jet Probability (JetProb)
• Transverse decay length (L_{xy})	• Reconstructed mass of pass 1 tracks
• L_{xy} significance ($L_{xy}/\sigma_{L_{xy}}$)	• Reconstructed mass of pass 2 tracks
• Pseudo-$c\tau$ ($L_{xy} \times M_{SECVTX}/p_T^{SECVTX}$)	• Number of pass 1 tracks
• Vertex Mass ($\sqrt{(\sum \lvert \boldsymbol{p}_{\rm vtx}\rvert)^2 - (\sum \boldsymbol{p}_{\rm vtx})^2}$)	• Number of pass 2 tracks
• $p_T^{\rm vtx}/(\sum_{\rm good\ tracks} p_T)$	• $\sum_{\rm Pass1\ track} p_T/p_T^{jet}$
• Vertex pass number (pass 1 or 2)	• $\sum_{\rm Pass2\ track} p_T/p_T^{jet}$

Table 4.1 Variables used in the Neural Network *b*-tagger.

The Neural Networks take as input the same 16 variables listed in **Table 4.1**, and distributions of the variables obtained from $t\bar{t}$ MC sample are shown in **Figs.4.4** and **4.5**. Those variables are chosen primarily based on the characteristics of *b*-quark decay that has higher track multiplicity, larger invariant mass, longer life time and harder fragmentation function than *c*- and *l*-quarks. The mass-energy-momenta quantities, track quantities and L_{xy} significance are good discriminators for *b*-jets. The p_T ratio variables are useful identifying *l*-jets, however *c*-jets are more difficult. Pseudo-$c\tau$ and fit χ^2 are the best discriminators. The output of the two Neural Networks are shown in **Fig.4.6**.

The Neural Network *b*-tagger discussed above is validated by comparing the performance on data and Monte Carlo. The Neural Network output from *b*-*l* network on a sample of SECVTX tagged heavy-flavor jets from the 8 GeV electron[5] data and the corresponding Monte Carlo sample are shown in **Fig.4.7**, and the output from *b*-*c* network on a tagged light-flavor jets from generic jet data and Monte Carlo is also shown there. In accordance with **Fig.4.7**, Neural Network *b*-tagger performance on data and Monte Carlo are consistent enough, and this means that the input variable modeling are good adequately.

The true *b*-jet selection efficiency as a function of the two Neural Network outputs for *b*, *c* and *l* jets are shown in **Fig.4.8**. We choose to set the cut value for 90% *b* efficiency (after the SECVTX efficiency), corresponding to a value of $NN_{bl} = 0.182$ and $NN_{bc} = 0.242$. The scale factor, measured from the electron sample, is 0.97 ± 0.02 (Note that this is the additional scale factor on top of the SECVTX scale factor, and applicable because all of the jets under consideration have already been tagged by SECVTX). Then we find the *l* and *c* jets rejection power at these cut values. 65% of light-flavor jets and about 50% of the *c* jets are rejected when keeping 90% of *b*-jets.

---

[5] The use of a property of semileptonic decay of *B* meson provides pure *b*-jets sample.

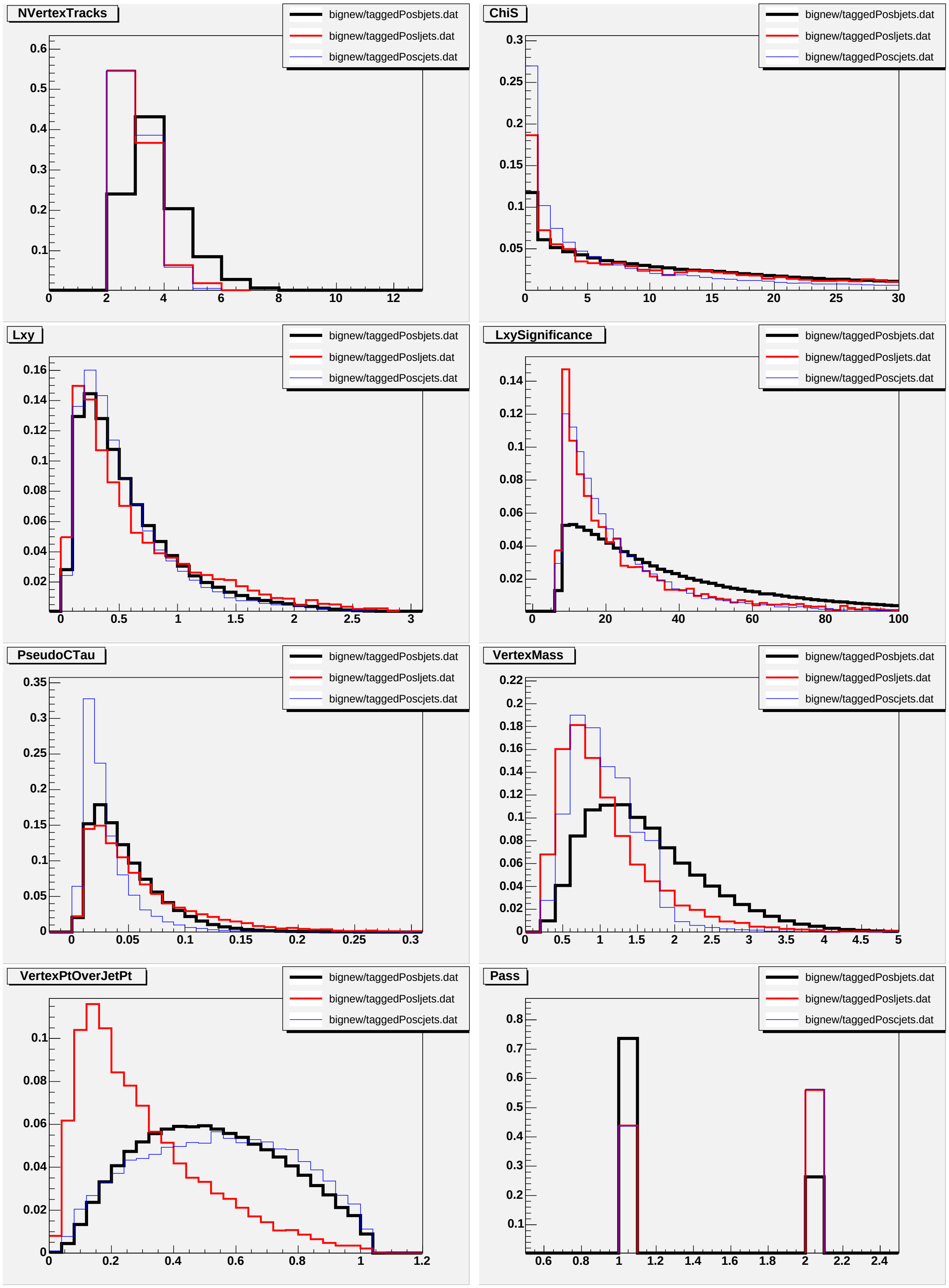

Figure 4.4 SECVTX related input variables for Neural Network b-tagger. Number of tracks in SECVTX(left), fit χ^2(right) in first row, L_{xy}(left), L_{xy} significance(right) in second row, pseudo-$c\tau$(left), vertex mass(right) in third row, $(p_T^{\text{vtx}}/(\sum_{\text{good tracks}} p_T)$(left) and vertex pass number(right) in the bottom row. Parton-jet matching is imposed for b(black), l(red) and c(blue) respectively.

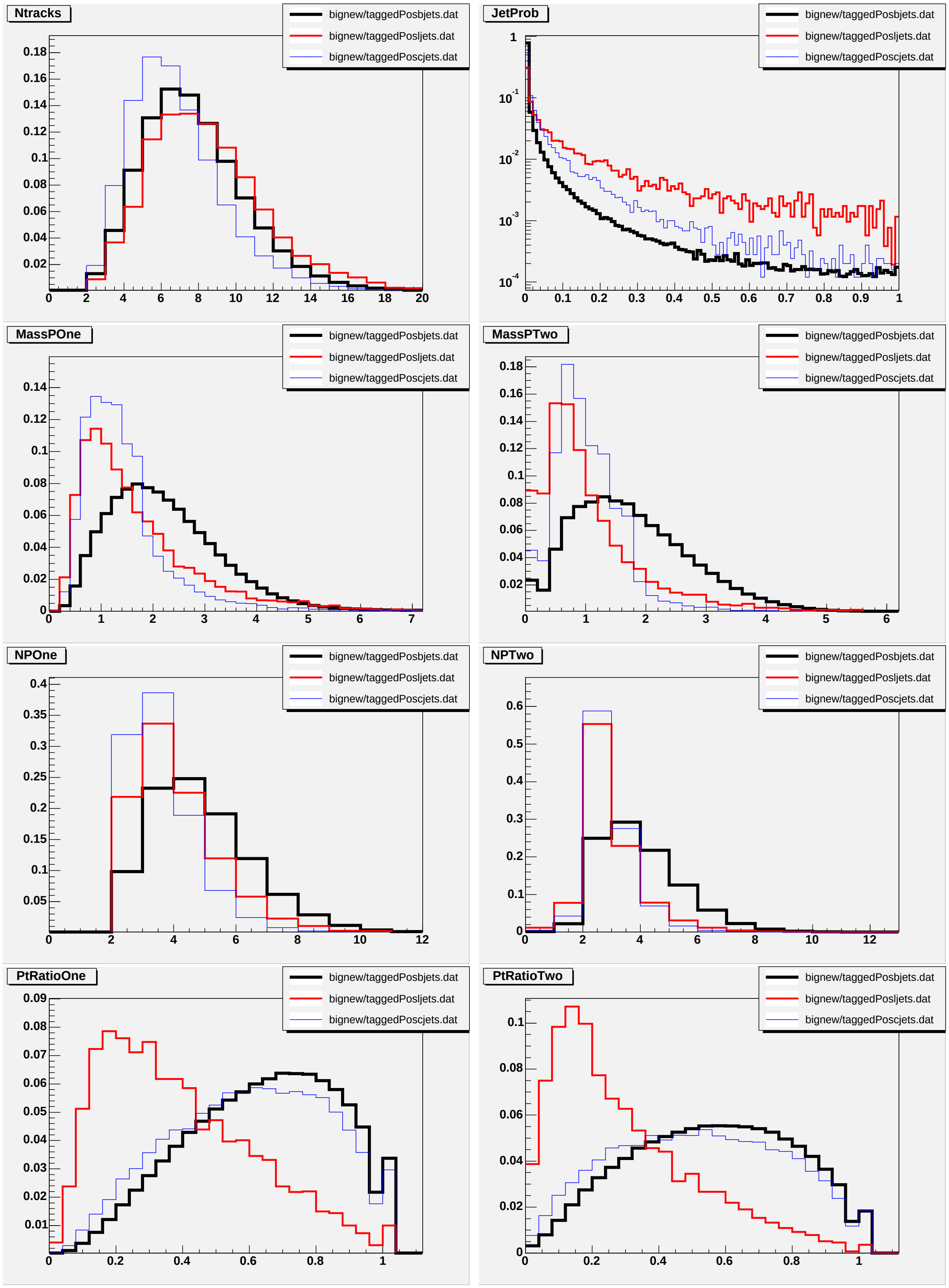

Figure 4.5 SECVTX independent input variables for Neural Network b-tagger. Number of good tracks(left), jet probability(right) in first row, reconstructed mass of pass 1(left) and pass 2(right) tracks in second row, number of pass 1(left) and pass 2(right) tracks in third row, $\sum_{track} p_T/p_T^{jet}$) of pass 1(left) and pass 2(right) tracks in the bottom row. Parton-jet matching is imposed for b(black), l(red) and c(blue) respectively.

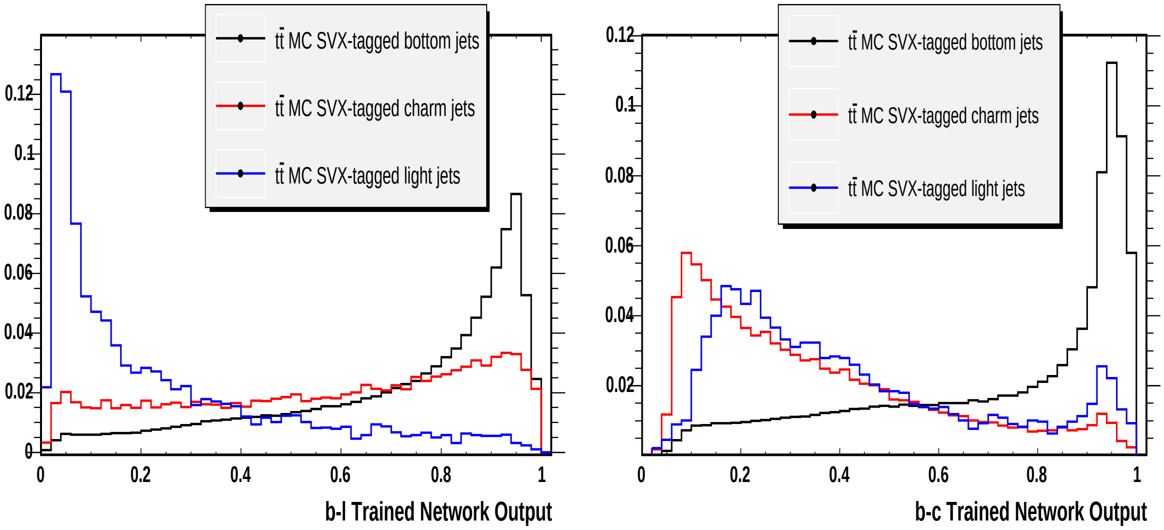

Figure 4.6 Neural Network outputs obtained from trainings of b-l(left) and b-c(right) jets. b, c and l jets are written in black, red and blue respectively.

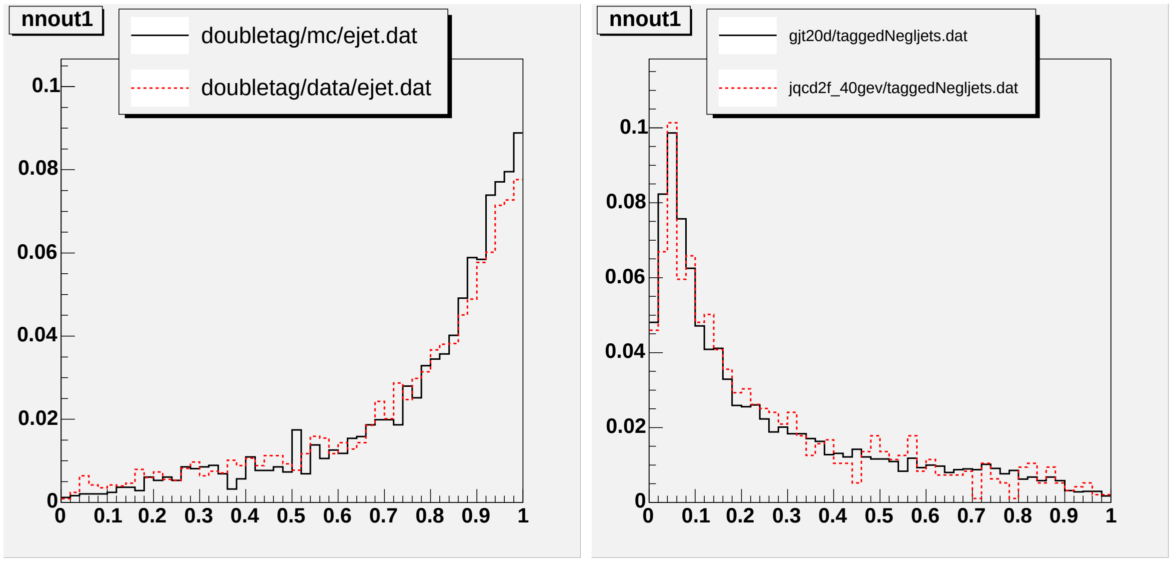

Figure 4.7 Comparisons of NN b-tag output in data (solid black), and Monte Carlo (dashed red) for SECVTX-tagged heavy-flavor-enriched jets (left) and tagged light-flavor jets (right).

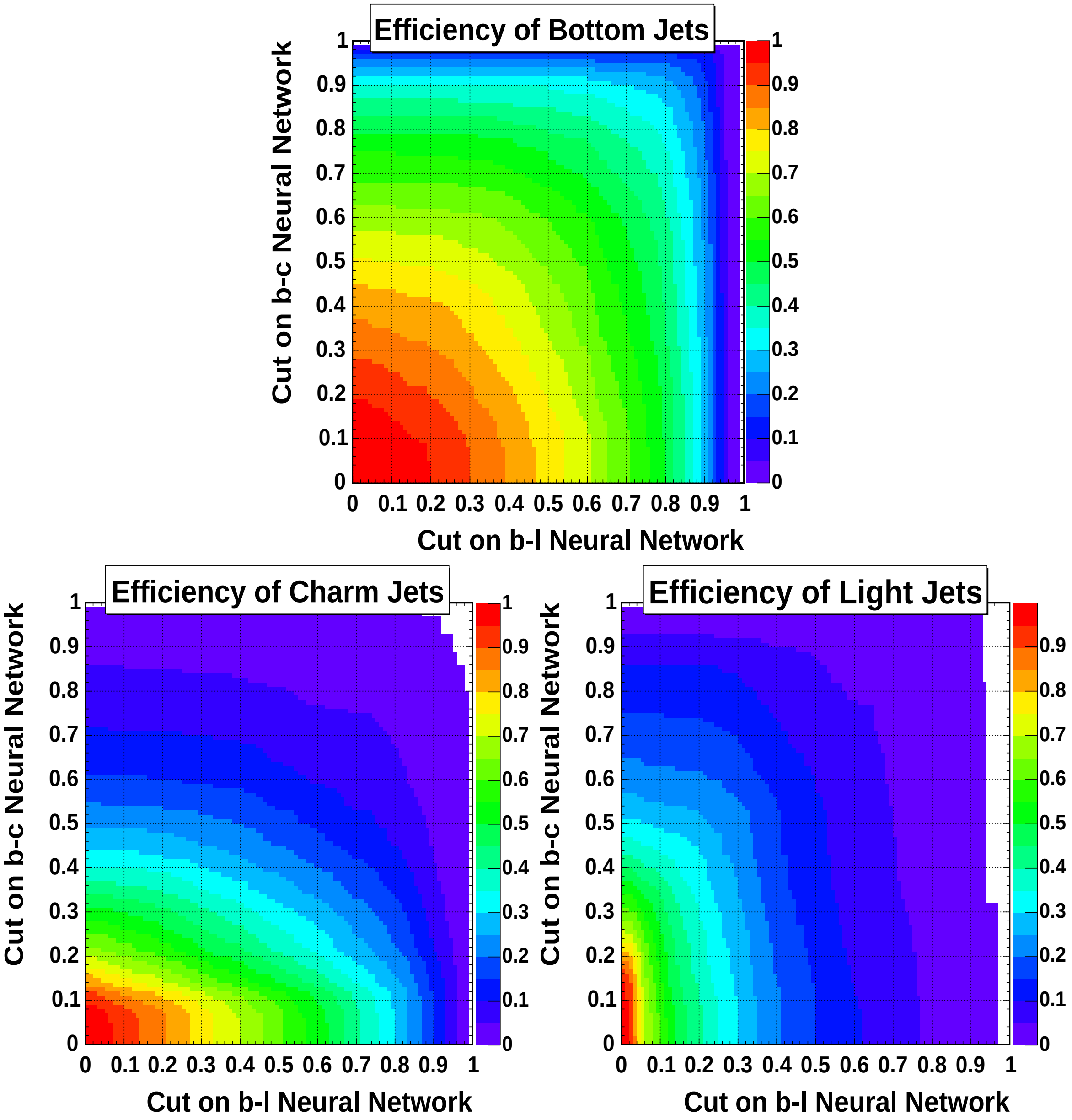

Figure 4.8 The true b-jet selection efficiency as a function of outputs from b-l and b-c networks obtained from b(top), c(bottom left) and l(bottom right) jets respectively.

Chapter 5

Data Set and Event Selection

One of the most important tasks for data analysis is the classification of events to select a set of events interesting to the physics process we are looking for. The classification is based on the final state particles and observable quantities. Particles identification and precise measurements of their 4-momentum are the goal of detectors in collider experiments, and which is called "event reconstruction". After the reconstruction, events selection which are meaningful to the target process is inevitable.

5.1 Event Reconstruction

The event data read out by the CDF detector has to undergo event reconstruction which, roughly speaking, converts tracking system hits, calorimeter energy deposition measurements and muon chamber stubs into physics objects that are associated with certain particles. The physics objects that are important to $WH \rightarrow \ell\nu b\bar{b}$ search are jets, high p_T electron or muon and large missing transverse energy(missing E_T or $\not\!\!E_T$), which is the imbalance of transverse energy measurement and assigned as a transverse energy of neutrino, because neutrino cannot be directly measured by CDF detector. Thereby, jet, electron, muon and missing E_T have to be reconstructed. Electron and muon identification criteria, jet and missing E_T reconstructions are discussed in detail.

5.1.1 Electron

Electron[1] identification starts with large energy deposition in the EM part of the calorimeter. An existence of a high-p_T track that matches the calorimeter readout is required as well as properties of the calorimeter shower profile, unlike a hadronic shower that spreads

---

[1] Electron here means e^- and e^+

into hadronic section and often spills over into neighboring towers, electromagnetic showers are short and well localized. A number of other requirements are imposed on an electron candidate and due to different instrumentation these requirements vary for different pseudo-rapidity ranges. Central (CEM) electrons propagate through the region of the detector with $|\eta| < 1.1$. The following list summarizes the identification criteria that a high-p_T central electron has to satisfy:

- Large energy deposit in calorimeter
  · $E_T \geq 20$ GeV

- Large transverse momentum obtained from COT track curvature
  · $p_T \geq 10$ GeV

- Most energy deposit in EM calorimeter
  · $E_{\mathrm{HAD}}/E_{\mathrm{EM}} \leq 0.055 + 0.00045 \times E_{\mathrm{tot}}$

- Matching between calorimeters and COT
  · $E/P \leq 2.0$ unless $P_T \geq 50$ GeV/c

- EM shower shape
  · $L_{\mathrm{shr}} \leq 0.2$
  Lateral shower profile variable, a measure of deviation of energy depositions in cluster towers from typical energy depositions observed in electron test-beam data

- Removal of charged hadron which mimics electron using CES and COT
  · -3.0 cm $< Q \times \Delta x < 1.5$ cm
  · $|\Delta z| < 3$ cm
  · $\chi^2_{\mathrm{strip}} < 10.0$
  where Δx and Δz are the r-ϕ/r-z distances between the COT track and the matching CES cluster and χ^2_{strip} is a comparison of the CES r-z profile to the electron test beam profile

- Vertex position in luminous region
  · $|z_0| < 60$ cm

- Track quality
  · COT axial superlayer segment hits ≥ 3
  · COT stereo superlayer segment hits ≥ 2
  Both segments are required to have ≥ 5 COT hits

- Fiducial volume
  Must traverse a well-instrumented detector region

- Photon conversion removal
  Photon can be misidentified if it converts to an electron-positron pair as it goes through materials. Such a photon is identified by looking for a pair of COT tracks satisfying:
  · opposite sign of the two track
  · $|\Delta(xy)| < 2$ mm
  · $|\Delta(\cot\theta)| < 0.04$
  where $\Delta(xy)$ is the distance between the tracks in the transverse plane and $\cot(\theta)$ is the difference between the cotangent of polar angles of the tracks.

- Isolation
  · $E_T^{\text{iso}}/E_T^{\text{cluster}} < 0.1$
  where E_T^{iso} is the energy transverse to the beam direction in the cone of $\Delta R < 0.4$ around the cluster excluding the electron cluster itself

The precision of electron transverse energy measurements from the EM clusters is shown in Eq.3.5.

5.1.2 Muon

As discussed in **Sec.3.2.3**, muons are measured in subsystems outside the calorimeters, which consists of CMU, CMP, CMX and IMU. Muon candidates are subdivided into several categories according to the detector subsystems that they propagate through. Muons that produce stubs[2] in both CMU and CMP chambers are called CMUP muons. The coverage of muon subsystems is different and the muons that have a stub in either CMU or CMP are labeled CMU-only or CMP-only muons. Muons that traverse and create a stub in CMX are called CMX muons. The list below summarizes additional criteria that a muon candidate has to satisfy:

- High p_T
  · $p_T \geq 20$ GeV/c

- Small energy deposit in calorimeters
  · $E_{\text{EM}} \leq 2 + \max(0, 0.0115 \times (p - 100))$ GeV
  · $E_{\text{HAD}} \leq 6 + \max(0, 0.0280 \times (p - 100))$ GeV

---

[2] Track segment reconstructed by 4 layer structure in CMU, CMP and CMX is called as “stub”.

- Isolation
  · $E_T^{\rm iso}/P_T \leq 0.1$
  where $E_T^{\rm iso}$ is the transverse energy in the cone of $\Delta R = 0.4$ around the muon track excluding the tower associated with the track.

- Vertex position in luminous region
  · $|z_0| \leq 60$ cm

- Cosmic ray removal
  Impact parameter(d_0) satisfies:
  · $|d_0| \leq 0.2$ cm for tracks without silicon hits
  · $|d_0| \leq 0.02$ cm for tracks with silicon hits
  · Timing measurements from COT and muon chambers

- Track quality
  · COT axial superlayer segment hits ≥ 3
  · COT stereo superlayer segment hits ≥ 2
  Both segments are required to have ≥ 5 COT hits.
  · χ^2 cut on muon tracks

- Matching between COT track and stub in muon chambers
  · $|\Delta x_{CMU}| \leq 3.0$ cm (CMUP)
  · $|\Delta x_{CMP}| \leq 5.0$ cm (CMUP)
  · $|\Delta x_{CMX}| \leq 6.0$ cm (CMX available after run number[3] of of 150144)
  where $|\Delta x|$ is the distance in the x-y plane between hits in muon chambers and the track extrapolated to the radius of the muon chambers

- Fiducial cut
  Muons must satisfy fiducial conditions listed below. Let $x_{\rm fid}$ and $z_{\rm fid}$ represent fiducial distances of the tracks in transverse plane and z-direction respectively.

  CMUP muons
  · Fiducial distance from CMU: $x_{\rm fid} < 0$ cm, $z_{\rm fid} < 0$ cm
  · Fiducial distance from CMP: $x_{\rm fid} < 0$ cm, $z_{\rm fid} < -3$ cm

  CMX muons
  · Fiducial distance from CMX: $x_{\rm fid} < 0$ cm, $z_{\rm fid} < -3$ cm
  · The tracks are required to go through all COT superlayers, e.g. exit the COT

---

[3] CDF data are assigned unique six digit number, what is called "run number", in chronological order.

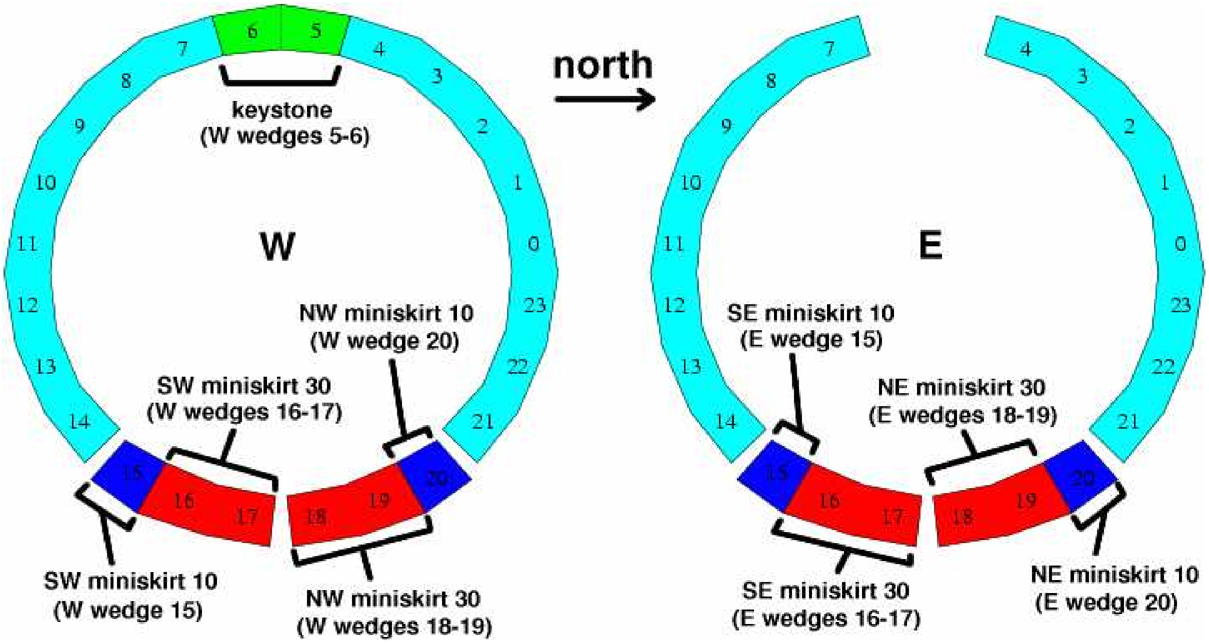

Figure 5.1 Transverse view of CMX coverage.

volume at a radius of 140cm.

· Exclude data that was detected specific CMX region which were not operating and/or triggering in a stable fashion. CMX coverage in transverse plane is shown in **Fig.5.1** and divided into 3 regions:

Arches: $0° \leq \phi < 75°$, $105° < \phi < 225°$, $315° < \phi < 360°$

·No use of $210° < \phi < 225°$ if $\eta < 0$ for runs between 190697 and 209760

Keystone: $75° \leq \phi \leq 105°$ and $\eta < 0$

· No use for runs before 190697

Miniskirt: $225° \leq \phi \leq 315°$

· No use for runs before 190697

The precision of muon momentum measurement is shown in Eq.3.4.

5.1.3 Jet

Quarks and gluons produced in the collisions undergo fragmentation as they travel away from the interaction point. This results in a stream of energetic colorless particles propagating in a relatively narrow cone around the original partons' direction (a hadronic jet). Most typically a jet consists of charged and neutral pions, kaons and to a lesser extent light baryons, like protons and neutrons. The energy of the original parton is inferred from the sum of energy depositions of jet constituents in calorimeter towers. Jet clustering is the procedure whereby the energy in nearby calorimeter cells is joined together in order to include as much as possible the energy depositions associated with the original parton, while excluding the energies that are not directly related to it.

The jet clustering starts with the most energetic calorimeter tower in a cluster, called a seed tower, and computes the energy sum in a cone of a given $\Delta R = \sqrt{\Delta\eta^2 + \Delta\phi^2}$. This analysis uses the cone size of $R = 0.4$. After a cluster is formed around the seed tower, the position of an E_T-weighted centroid is computed as:

$$\eta_{\text{centroid}} = \frac{\sum_{i \in \text{cluster}} E_T^i \eta^i}{\sum_{i \in \text{cluster}} E_T^i}, \tag{5.1}$$

$$\phi_{\text{centroid}} = \frac{\sum_{i \in \text{cluster}} E_T^i \phi^i}{\sum_{i \in \text{cluster}} E_T^i}. \tag{5.2}$$

The centroid position defines the new cluster center and the new clustering cone is drawn around it. The process is repeated until the cluster remains unchanged. In some situations the clusters overlap and are either merged if the overlap is more than 75% or left unchanged. A jet "raw" four-momentum is then determined based on the energy of the cluster and the position of the centroid. There are a lot of effects both physics and detector that contribute to the deviation of the jet four-momentum constructed as outlined above and the four-momentum of the original parton. Several corrections are applied to the raw quantities:

$$E_T^{\text{corr}} = (E_T^{\text{raw}} \times f_{\text{rel}} \times -E_T^{\text{MI}}) \times f_{\text{abs}} - E_T^{\text{UE}} + E_T^{\text{OC}}, \tag{5.3}$$

where the corrections are the following:

- Level 1: relative correction, f_{rel}, detector-η dependent, takes into account differences in tower-by-tower calorimeter response

- Level 2: time-dependent correction, f_{time}, compensates for calorimeter deterioration over time, due, for instance, to aging of the photo-tubes

- Level 3: raw energy scale, f_{scale}, accounts for non-linearities in single-particle

- Level 4: multiple interactions, E_T^{MI}, correct for the possibility of several interactions in a particular bunch-crossing, parametrized by the number of vertices in the event

- Level 5: absolute energy correction, f_{abs} , a p_T-dependent factor obtained from the Monte Carlo as a mean ratio of parton p_T to the jet p_T

- Level 6: underlying event, E_T^{UE} , accounts for any contributions to the jet energy not coming from the original parton, beam remnants, spectator partons
- Level 7: out-of-cone correction, E_T^{OC} , parametrized by p_T and determined from Monte Carlo, accounts for the energy deposited outside of the cone due to gluon radiation and fragmentation effects

Where level 2 and 3 corrections are no longer used explicitly, but those correction effects are already included in level 1 correction[4].

5.1.4 Missing Transverse Energy

The so called "missing transverse energy" or $\not\!\!E_T$ is a reconstructed object that is not directly related to a single particle produced in a collision. Considered as a two-component vector that lies in the plane transverse to the beam direction it is simply the negative of the sum of all transverse momenta in the event. More precisely, the uncorrected $\not\!\!E_T$ is the negative of the vector sum of all calorimeter tower depositions projected on the transverse plane. The missing energy is often thought of as a measure of the sum of the momenta of the particles that escape detection, most notably neutrinos. In order to be more readily interpretable as such the raw $\not\!\!E_T$ needs to be corrected:

$$\not\!\!\boldsymbol{E}_T^{\mathrm{corr}} = \not\!\!\boldsymbol{E}_T^{\mathrm{raw}} - \sum_{\mathrm{jets}} \left(\boldsymbol{E}_{T\mathrm{jet}}^{\mathrm{corr}} - \boldsymbol{E}_{T\mathrm{jet}}^{\mathrm{raw}} \right), \tag{5.4}$$

where $\boldsymbol{E}_{T\mathrm{jet}}^{\mathrm{corr}}$, $\boldsymbol{E}_{T\mathrm{jet}}^{\mathrm{raw}}$ are transverse energy of jets before and after the jet energy correction, $\not\!\!\boldsymbol{E}_T^{\mathrm{raw}}$ is a raw level missing E_T defined as:

$$\not\!\!\boldsymbol{E}_T^{\mathrm{raw}} = - \sum_{i \in \mathrm{tower}} \boldsymbol{E}_T^{(i)}, \tag{5.5}$$

where $\boldsymbol{E}_T^{(i)}$ is transverse energies of any calorimeter towers.

5.2 Event Selection

The experimental observable particles of $WH \to \ell\nu b\bar{b}$ are lepton($e^{\pm}/\mu^{\pm}$), two jets and missing E_T, where lepton and missing E_T are originating from W-boson. Thereby such a lepton is expected to have high-p_T and also large missing E_T is expected because almost all of energies of W-boson is split into lepton and neutrino. For $WH \to \ell\nu b\bar{b}$ target process,

---

[4] In a development of jet energy correction, those corrections were divided before.

high-p_T electron and muon triggers are used and additional offline selection criteria are imposed.

5.2.1 Triggers

High-p_T Electron Trigger

At the Level 1 trigger, calorimeter towers are gathered in pairs so that the effective $\eta \times \phi$ segmentation is $0.2 \times 15°$. At least one trigger tower is required to have $E_T > 8$ GeV with $E_{\mathrm{HAD}}/E_{\mathrm{EM}} < 0.125$. At least one XFT track with $p_T > 8$ GeV/c is also required to point to this tower. At Level 2, a clustering algorithm combines the energy deposited in neighboring towers. Towers adjacent to the seed tower fond at Level 2 with $E_T > 7.5$ GeV are added to the cluster. The total E_T of the cluster must be larger than 16 GeV. At Level 3, full event reconstruction and electron identification are performed. A three dimensional COT track of $p_T > 9$ GeV must point to a cluster of $E_T > 18$GeV with $E_{\mathrm{HAD}/E_{\mathrm{EM}}} < 0.125$. This trigger is denoted by "`ELECTRON_CENTRAL_18`"

High-p_T Muon Trigger

CMUP : At Level 1, hits in the CMU to match hits in the CMP are required. An XFT track with $p_T > 4$ GeV/c must point to the CMU and CMP hits. At Level 2, XFT track with $p_T > 8$ GeV/c, which does not necessarily match the muon hits, has to exist. At Level 3, a fully reconstructed COT track with $p_T > 18$ GeV/c must match a stub in the CMU($|\Delta x|_{\mathrm{CMU}} < 10$ cm) and in the CMP($|\Delta x|_{CMP} < 20$ cm). This trigger is called "`MUON_CMUP18`".

CMX : At Level 1, CMX hits must match the central muon extension scintillator hits and an XFT track with $p_T >$8 GeV/c. At Level 2, no requirement is imposed. At Level 3, a fully reconstructed COT track with $p_T > 18$ GeV/c must match a stub in the CMX($|\Delta x|_{\mathrm{CMX}} < 10$ cm). This trigger is called "`MUON_CMX18`".

5.2.2 Offline Selections

To select candidate events of $WH \rightarrow \ell\nu b\bar{b}$ process, the following criteria are imposed:

- Data quality

  Data taken with silicon detector components must be in good quality[56], which is based on the conditions of each component of detectors.

- Trigger

  Data must be triggered by the specific triggers discussed in the previous section.

- Presence of exactly one primary lepton($e^{\pm}/\mu^{\pm}$)
  Leptonic decay of W-boson produce exactly one high p_T electron or muon, which must be identified by the criteria discussed in **Secs.5.1.1** and **5.1.2**. If there exist more than one leptons, such events are vetoed.

- Distance between primary vertex and vertex of lepton track
  · $|z_{\text{lepton track}} - z_0| < 5$ cm
  If the lepton is coming from the interaction point(primary vertex, z_0), vertex position of lepton track($z_{\text{lepton track}}$) should be close to primary vertex.

- Z^0 removal
  If some leptons are not identified correctly, for example isolated tracks, $Z^0 \rightarrow \ell\bar{\ell}$ events still remain. To remove such events, invariant mass of the lepton and other objects(X) must not be in the Z^0-boson mass window($76 < m_{\ell X} < 106$ GeV/c^2).

- Large missing E_T
  · $\not{E}_T > 20$ GeV
  Neutrino from W-boson decay is expected to have large missing transverse energy.

- Jet
  · $E_T > 15$ GeV
  · $|\eta| < 2.0$
  The target process considered in this thesis contains two jets originating from $H \rightarrow b\bar{b}$ decay mode. Thus the jets are expected to have large transverse energy and they are required to be in the SVX coverage for SECVTX b-tagging. For the search for $WH \rightarrow \ell\nu b\bar{b}$, $W+$ exactly 2 jets events are used. However, W+1,3,$\geq$4 jet events also gives a good cross checks of the data handling and background modeling considered in the next chapter.

- b-tagging
  To increase the purity of b-tagged events, at least one SECVTX b-tagged jets are required. If only one of the jets is b-tagged, the jet is required to pass the Neural Network b-tagging filter to reject mistag, $Wc\bar{c}$ and Wc event. If there are two or more SECVTX b-tagged jets, Neural Network is not applied. Such events are considered to be pure enough, because it is rare that two or more jets are mistagged by SECVTX simultaneously.

Detector	Integrated luminosity(pb^{-1})
CEM	955 ± 57
CMUP	955 ± 57
CMX (arch)	941 ± 56
CMX (keystone and miniskirt)	622 ± 37

Table 5.1 Integrated luminosity breakdown into sub detectors.

5.2.3 Luminosity

The data used in this thesis is collected between February 2002 and February 2006. The integrated luminosity as a function of time is shown in **Fig.1.2**, which shows that about 1.7 fb^{-1} is delivered by TEVATRON and 1.5 fb^{-1}, which does not require silicon detectors, is recorded by CDF DAQ system. The integrated luminosity of data with silicon detector and good quality becomes 955 pb^{-1}. Due to some inefficiency in specific portions of detectors, the total luminosities differ from detector to detector as listed in **Table 5.1**. In this thesis, the total luminosity is denoted by 955 pb^{-1} or $1\mathrm{fb}^{-1}$ depending on the context.

Chapter 6

Background

Once data interesting to the target process is obtained, background estimation, which is dependent on the purposes of analyses, becomes possible and it is the biggest deal to say something new from the data. In this chapter, a method of background estimation is discussed in detail. The final state of $WH \rightarrow \ell\nu b\bar{b}$ process is lepton $(e^{\pm}/\mu^{\pm})$+ two jets + large missing E_T, which is called "W+2jets" event. This state is very similar to the most promising process of top quark pair production, what is called "W+4jet"[1] process ($t\bar{t} \rightarrow (b\ell^{-}\bar{\nu})(bq\bar{q}')$) except for the number of jets. W+3 or more jets bin is dominated by $t\bar{t}$ events. Thereby, the background estimate can be validated by measuring $t\bar{t}$ production cross section using W+3 or more jets data. For this purpose, background estimation is performed for W+1, 2, 3, ≥ 4 jet events.

6.1 Background Categories

Background consists of all possible physics process except for the target process. The purpose of the background estimation is to search for the Standard Model Higgs boson. Thus the background components listed below are taken into account.

- Non-W QCD:
  Events that lepton is faked by QCD jet or lepton comes from semileptonic decay of heavy flavor jet

- Mistag:
  Events that have jets falsely b-tagged by SECVTX and Neural Network b-tagger due to vertex and track resolution

---

[1] When one of the jets are not measured or does not satisfy the jet selection criteria, such an event, called "W+3jet", is also used because large acceptance of $t\bar{t}$ process in $W + 3$jet bin

- $W+$ heavy flavor:
  $Wb\bar{b}$, $Wc\bar{c}$ and Wc processes in parton level

- Monte Carlo derived background:
  Events originating from $t\bar{t}$, single top, diboson ($WW/WZ/ZZ$) and $Z \to \tau\tau$ processes

In the following subsections, each contributions of the background source is discussed in detail.

6.1.1 Non-W QCD

Jet events sometimes mimic W-boson signature when jet passes the lepton selection criteria based on calorimeter based measurement or heavy flavor jet produces leptons via semileptonic decay. Also large missing E_T deriving from mismeasurements of energy or semileptonic decays of heavy flavor jet can be obtained. It is difficult to model and produce such a event in detector simulation since heavy flavor content cannot be well predicted.

Generally, non-W events mainly come from a non-isolated lepton[2] and small missing E_T. Such a event is used to extrapolate the expected non-W contribution in signal region, e.g. good lepton isolation and large missing E_T. Accordingly, let isolation vs missing E_T plane be divided into 4 sectors (shown in **Fig.6.1**)[57, 58]:

- region A: Isolation > 0.2 and $\not\!\!E_T < 15$ GeV
- region B: Isolation < 0.1 and $\not\!\!E_T < 15$ GeV
- region C: Isolation > 0.2 and $\not\!\!E_T > 20$ GeV
- region D: Isolation < 0.1 and $\not\!\!E_T > 20$ GeV

Here, region D is the signal region. Missing E_T vs isolation distribution obtained from high-p_T electron and muon samples are shown in **Fig.6.2**. For an extraction of non-W background from data, we set a couple of assumptions:

- Lepton isolation and missing E_T are uncorrelated in non-W events
- b-tagging rate is not dependent on missing E_T in non-W events

---

[2] Object that passes all of the lepton identification criteria except for isolation requirement.

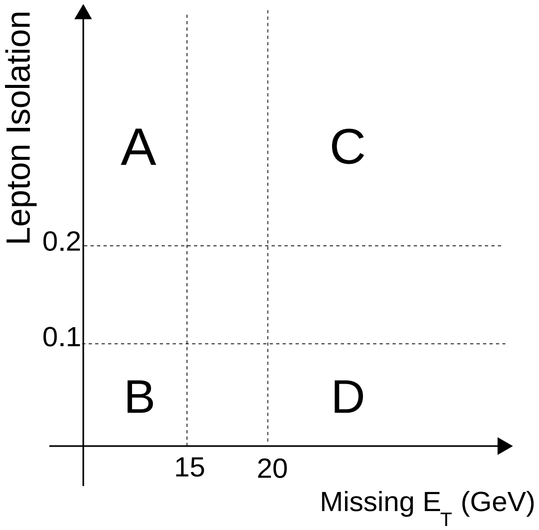

Figure 6.1 Missing E_T and lepton isolation plane divided into four sectors for non-W background estimation.

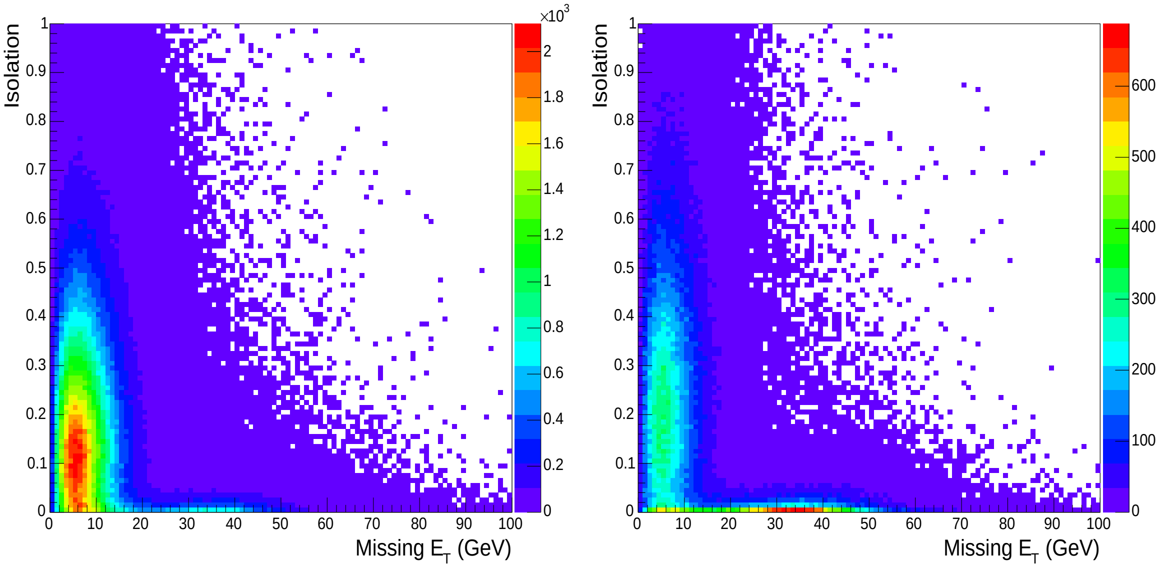

Figure 6.2 Missing E_T vs lepton isolation distributions in high-p_T electron(left) and muon(right) samples associated with at least one jet before applying SECVTX b-tagging.

Lepton and missing E_T in non-W events are not real, therefore there is not any reason to have correlation between them. Also b-tagging is not supposed to be affected too much by missing E_T.

With the first assumption, the number of non-W events($N_D^{\mathrm{non}-W}$) and its fraction($f_{\mathrm{non}-W}$) in the signal region before requiring b-tagging are obtained as:

$$N_D^{\mathrm{non}-W} = \frac{N_B \times N_C}{N_A}, \tag{6.1}$$

$$f_{\mathrm{non}-W} = \frac{N_D^{\mathrm{non}-W}}{N_D} = \frac{N_A \times N_B}{N_C \times N_D}, \tag{6.2}$$

where N_i $(i = A, B, C, D)$ are the number of pretag[3] events in each sideband region. In accordance with the second assumption, the SECVTX b-tagging efficiency obtained in region B can be applied to the signal region D. Here we define an event tagging efficiency per taggable jets as:

$$r_B = \frac{N_B^{(\text{tagged event})}}{N_B^{(\text{taggable jet})}}, \tag{6.3}$$

where $N_B^{(\text{tagged event})}$ and $N_B^{(\text{taggable jet})}$ are number of tagged events and taggable jets in region B respectively. Then the number of non-W background in region D after SECVTX b-tagging($N_D^{+\mathrm{non}-W}$) is obtained by the relation of:

$$N_D^{+\mathrm{non}-W} = f_{\mathrm{non}-W} \times r_B \times N_D^{(\text{taggable jets})}. \tag{6.4}$$

We call this procedure "Tag Rate Method" since it uses the tag rate in region B It is also possible to estimate non-W contribution directly from the SECVTX tagged sample as:

$$N_D^{\prime+\mathrm{non}-W} = \frac{N_B^+ \times N_C^+}{N_A+}, \tag{6.5}$$

where $N_X^+(X = A, B, C, D)$ denotes positive SECVTX b-tagged events, and this method is called "Tagged Method". These methods are data-based techniques, so the estimates could also contain other background processes. Subtracting the known backgrounds should results in a better non-W QCD estimate. The contributions from $t\bar{t}$ and W+jets events to each sideband region are studied in [57, 58], and their contributions from $t\bar{t}$ and W+jets events to each side band region are subtracted.

For a validation and estimation of systematic uncertainties of the four sector method, the following sectors are considered:

- region A: Isolation > 0.2 and $\not\!\!E_T < 15$ GeV

---

[3] Pretag means before b-tagging

Jet Multiplicity	1jet	2jet	3jet	≥4jet
TagRate	124.6 ± 25.8	56.9 ± 12.1	16.3 ± 3.6	6.5 ± 1.5
Tagged	206.1 ± 54.7	76.5 ± 22.4	24.1 ± 9.4	20.8 ± 12.0
Combined	139.1 ± 23.3	61.3 ± 10.7	17.3 ± 3.4	6.7 ± 1.5

Table 6.1 Summary of non-W background estimate as a function of jet multiplicity for events with at least one SECVTX b-tagged jet.

- region E: $0.1 <$ Isolation < 0.2 and $\not\!\!E_T < 15$ GeV
- region C: Isolation > 0.2 and $\not\!\!E_T > 20$ GeV
- region F: $0.1 <$ Isolation < 0.2 and $\not\!\!E_T > 20$ GeV
- region A'': Isolation > 0.1 and $\not\!\!E_T < 10$ GeV
- region A' : Isolation > 0.1 and $10 < \not\!\!E_T < 20$ GeV
- region B'': Isolation < 0.1 and $\not\!\!E_T < 10$ GeV
- region B' : Isolation < 0.1 and $10 < \not\!\!E_T < 20$ GeV

These regions are slightly different from what was considered the non-W estimation. Thus they are useful to see the effects, e.g. stability and systematic uncertainty, when boundaries of the four sectors are varied. The ratios of $G = (N_E \cdot N_C)/(N_A \cdot N_F)$ and $G' = (N_{B''} \cdot N_{A'})/(N_{A''} \cdot N_{B'})$ are calculated for both pretag and tagged samples. Here region F and B' are the isolation and missing E_T side band region. If the extrapolations from isolation and missing E_T are valid, the fractions of G and G' should be equal to unity. Deviations from unity is assigned as systematic uncertainty. For both of pretag and tagged estimate, 25% systematic uncertainty is assigned conservatively.

After obtaining the estimates independently with the tag rate method and tagged method, those two results are combined by taking weighted average. At first the estimates over the different detector components for each method are added, then these two methods are combined. The final non-W estimates are shown in **Table 6.1** for events with at least one SECVTX b-tagged jet. The result from tagged method gives slightly higher estimate than tag rate method. But those methods are considered consistent within uncertainties.

When Neural Network b-tagging is applied, a non-W rejection factor is measured from data in region C. Region C is supposed to have a very similar event kinematics to real non-W events in the signal region D because only lepton isolation is the difference between the two regions. Finally, non-W estimate before applying NN b-tagging is scaled by this rejection factor.

Jet Multiplicity	1jet	2jet	3jet	≥4jet
≥1 SECVTX	139.1 ± 23.3	61.3 ± 10.7	17.3 ± 3.4	6.7 ± 1.5
= 1 SECVTX	139.1 ± 23.3	59.9 ± 10.4	16.4 ± 3.2	6.4 ± 1.4
= 1 SECVTX & NN tag	84.2 ± 14.1	38.9 ± 6.7	12.1 ± 2.3	5.5 ± 1.2
≥ 2 SECVTX	-	1.4 ± 0.3	0.9 ± 0.2	0.3 ± 0.1

Table 6.2 Summary of non-W background estimate as a function of jet multiplicity for various b-tagging options.

The non-W estimate for events with at least two SECVTX tags is obtained by measuring the ratio of the number of events with at least one b-tagging to that with at least two b-taggings in region A'(Isolation > 0.1 and $10 < \not{E}_T < 20$ GeV), B, and C'(Isolation > 0.1 and $\not{E}_T > 20$ GeV) because just a few events remain after requiring at least two SECVTX b-tagging. The non-W estimate for at least two SECVTX b-tagging is obtained by applying the ratio to the estimate with at least one SECVTX b-tagging. The results of non-W background estimate for various b-tagging strategies are summarized in **Table 6.2**

6.1.2 Mistag

The rate of SECVTX mistag or false tagged jets is derived from generic jet sample varying bins of η, ϕ, jet E_T, track multiplicity within an event[59]. Tag rate probabilities are summed for all of the taggable jets in the event. Since the double mistag rate is small, this sum is a good approximation of the single-tag event rate. Negative mistags, tags with unphysical negative decay length due to finite tracking resolution, are calculated as an estimate of falsely tagged jets, independent to first order of heavy flavor content in the generic jet sample. And 8% systematic uncertainty is taken into account. The positive mistag rate is enhanced relative to the negative tag rate by light-flavor secondary vertices and material interactions in the silicon detectors. As a result, the positive mistag rate is estimated by multiplying the negative mistag rate by a factor of 1.37 ± 0.15 [60]. For data collected after December 2004, additional correction factor of 1.05 ± 0.03 [61] is applied. The final mistag estimate is corrected down by the non-W QCD fraction and also the $t\bar{t}$ contribution to the pretag sample. To estimate the mistag contribution in NN-tagged events, we apply the light flavor rejection power of the b-tagger 0.35 ± 0.05, as shown in **Sec.4.2**, to the mistag estimate before applying NN b-tagger[62]. The mistag estimate for various b-tagging strategies are summarized in **Table 6.3**.

Jet Multiplicity	1jet	2jet	3jet	≥4jet
$\geq$ 1 SECVTX tag	399.0 ± 63.0	163.5 ± 25.8	49.2 ± 7.8	15.2 ± 2.4
= 1 SECVTX tag	399.0 ± 63.0	159.9 ± 25.3	47.2 ± 7.5	14.0 ± 2.2
= 1 SECVTX & NN tag	139.7 ± 27.3	53.9 ± 10.7	15.7 ± 3.1	4.2 ± 0.8
$\geq$ 2 SECVTX tag	-	3.5 ± 0.5	2.0 ± 0.3	1.2 ± 0.2

Table 6.3 Summary of mistag background estimate for various b-tagging strategies.

6.1.3 W+Heavy Flavor

The $Wb\bar{b}$ and $Wc\bar{c}$ states are major sources of background of b-tags in the W+jets channel. They are estimated primarily from the Monte Carlo, but their overall rates are normalized to data, because MC generators can predict W+jets events only to leading order diagrams. As a result, large theoretical uncertainties exist for overall normalization. The contribution from true heavy flavor production in W+jet events is determined from measurements of the heavy flavor event fraction in W+jet events and the tagging efficiency for those events.

These heavy flavor fractions have been studied extensively [63] using ALPGEN + HERWIG Monte Carlo[64, 65]. Heavy flavor fractions measured in ALPGEN have been calibrated using a jet data sample. A scaling factor of 1.5 ± 0.4 is found to be necessary to make the heavy flavor production in Monte Carlo match the production in data. The final results of heavy flavor fractions are obtained as shown in **Table 6.4**. In the table, 1B and 1C means the case that only one of the heavy flavor jets are detected when one of them goes out of the detector coverage or two jets merge into the same jet. 2B and 2C are the case that both of the heavy flavor jets are observed.

For the tagged W+HF background estimate, the heavy flavor fractions and tagging rates given in **Tables 6.4** and **6.5** are multiplied by the number of pretag events in data, after the number of pretag events have been corrected for the non-W contribution. The W+HF background must also be corrected for the contribution of $t\bar{t}$ events to the pretag sample.

In the previous analysis with 319 pb^{-1}[8] the evidence that the disagreement in W+1jet and W+2jet events are due to the heavy flavor fraction. In this analysis, the same correction factor of 1.2 ± 0.2, which is obtained by fitting W+1jet events, is applied to the heavy flavor fraction. Finally W+HF background is obtained by the following relation:

$$N_{W+HF} = f_{HF} \cdot \epsilon_{\text{tag}} \cdot \left[N_{\text{pretag}} \cdot (1 - f_{\text{non}-W}) - N_{\text{EWK}}\right], \tag{6.6}$$

where f_{HF} is heavy fraction, ϵ_{tag} is tagging efficiency and N_{EWK} is the expected number of $t\bar{t}$, single top and diboson events. The W+heavy flavor background estimate is

Jet Multiplicity	1jet	2jet	3jet	$\geq$ 4 jet
W+HF fraction before tagging (%)				
$WBB(1B)$	1.0 ± 0.3	1.4 ± 0.4	2.0 ± 0.5	2.2 ± 0.6
$WBB(2B)$	0.0 ± 0.0	1.4 ± 0.4	2.0 ± 0.5	2.6 ± 0.7
$WCC(1C)$	1.6 ± 0.4	2.4 ± 0.6	3.4 ± 0.9	3.6 ± 1.0
$WCC(2C)$	0.0 ± 0.0	1.8 ± 0.5	2.7 ± 0.7	3.7 ± 1.0
Wc	4.3 ± 0.9	6.0 ± 1.3	6.3 ± 1.3	6.1 ± 1.3

Table 6.4 The heavy flavor fractions in W + jets sample. Raw results from ALPGEN Monte Carlo have been scaled by the data-derived calibration factor of 1.5 ± 0.4. (Wc fractions have not been rescaled.)

summarized in **Table 6.6**.

6.1.4 Monte Carlo Derived Background

The normalization of the diboson and single top backgrounds are based on the theoretical cross sections listed in **Table 6.7**[66–69], the measured luminosity and the acceptance and b-tagging efficiency derived from MC. The MC acceptance is corrected for lepton identification, trigger efficiencies and z vertex cut. The tagging efficiency is always corrected by the scale factor (MC/data) of 0.89± 0.07. The expected number of events is obtained by the equation

$$N = \int \mathcal{L}dt \times \epsilon \times \sigma, \tag{6.7}$$

where ϵ is the total detection efficiency corrected by all of the scale factors.

6.1.5 Summary of Background Estimate

We have described the contributions of individual background sources to the final background estimate. The summary of the background estimates for the b-tagging condition of exactly one b-tagged jet before and after applying NN filter and at least two SECVTX b-tagged jets are shown in **Tables 6.8**, **6.9**, **Figs.6.3** and **6.4**. In accordance with those tables and figures, observed data and the Standard Model background expectations are consistent each other before and after Neural Network b-tagging is applied. It is also true for at least two b-tagged events shown in **Table 6.10** and **Fig.6.4**.

Jet Multiplicity	1jet	2jet	3jet	$\geq$ 4jet
		$\geq$ 1 SECVTX b-tag		
$WBB(1B)$	33.2 ± 2.4	34.5 ± 2.5	36.7 ± 2.6	40.2 ± 2.9
$WBB(2B)$	-	51.3 ± 3.6	54.1 ± 3.8	55.1 ± 3.9
$WCC(1C)$	6.2 ± 0.9	8.0 ± 1.1	9.7 ± 1.4	11.6 ± 1.6
$WCC(2C)$	-	14.4 ± 2.0	17.0 ± 2.4	17.8 ± 2.5
WC	8.9 ± 1.3	8.7 ± 1.2	7.6 ± 1.1	3.4 ± 0.5
		$\geq$ 1 SECVTX and NN b-tag		
$WBB(1B)$	29.9 ± 2.1	31.8 ± 2.3	34.1 ± 2.4	35.9 ± 2.6
$WBB(2B)$	-	47.2 ± 3.4	51.5 ± 3.7	51.3 ± 3.6
$WCC(1C)$	3.8 ± 0.5	5.5 ± 0.8	6.1 ± 0.9	6.4 ± 0.9
$WCC(2C)$	-	9.9 ± 1.4	8.6 ± 1.2	9.5 ± 1.4
WC	5.0 ± 0.7	4.6 ± 0.7	3.1 ± 0.4	3.4 ± 0.5
		$\geq$ 2 SECVTX b-tag		
$WBB(2B)$	-	9.7 ± 0.7	13.6 ± 1.0	11.5 ± 0.8
$WCC(2C)$	-	1.2 ± 0.2	0.8 ± 0.1	0.9 ± 0.1

Table 6.5 The b-tagging efficiencies by various b-tagging strategies for individual W+heavy flavor processes. Those numbers include the effect of the scale factors of SECVTX and NN b-tagger.

Jet multiplicity	1jet	2jet	3jet	$\geq$ 4jet
		$\geq$ 1 SECVTX b-tag		
$Wb\bar{b}$	340.9 ± 118.3	179.0 ± 61.2	37.8 ± 12.3	8.0 ± 3.2
$Wc\bar{c}$	101.6 ± 35.3	67.1 ± 22.9	16.4 ± 5.3	3.7 ± 1.5
Wc	325.7 ± 82.8	65.1 ± 17.0	8.3 ± 2.2	0.6 ± 0.2
		= 1 SECVTX b-tag		
$Wb\bar{b}$	340.9 ± 118.3	158.7 ± 54.2	32.1 ± 10.5	7.0 ± 2.8
$Wc\bar{c}$	101.6 ± 35.3	63.8 ± 21.8	16.0 ± 5.2	3.6 ± 1.5
Wc	325.7 ± 82.8	65.1 ± 17.0	8.3 ± 2.2	0.6 ± 0.2
		= 1 SECVTX and NN b-tag		
$Wb\bar{b}$	306.9 ± 106.9	144.7 ± 49.4	29.9 ± 9.7	6.4 ± 2.5
$Wc\bar{c}$	63.1 ± 22.0	43.0 ± 14.7	8.7 ± 2.8	1.9 ± 0.8
Wc	185.7 ± 47.2	34.4 ± 9.0	3.4 ± 0.9	0.6 ± 0.2
		$\geq$ 2 SECVTX b-tag		
$Wb\bar{b}$	-	20.3 ± 7.0	5.7 ± 1.8	1.0 ± 0.4
$Wc\bar{c}$	-	3.3 ± 1.1	0.4 ± 0.1	0.1 ± 0.04
Wc	-	-	-	-

Table 6.6 Summary of W+heavy flavor background estimate for various b-tagging options.

Theoretical Cross Sections	
WW	12.40 ± 0.8 pb
WZ	3.96 ± 0.06 pb
ZZ	1.58 ± 0.02 pb
Single Top s-channel	0.88 ± 0.05 pb
Single Top t-channel	1.98 ± 0.08 pb
$Z \to \tau\tau$	320 ± 9.0 pb
$t\bar{t}$	$6.7\ ^{+0.7}_{-0.9}$ pb

Table 6.7 Theoretical cross sections and errors for the electroweak and single top backgrounds, along with the theoretical cross section for $t\bar{t}$ at ($m_t = 175\text{GeV/c}^2$). The cross section of $Z^0 \to \tau\tau$ is obtained in the dilepton mass of $m > 30$ GeV/c^2 together with k-factor(NLO/LO) of 1.4.

! !! !! !! !! ! Jet Multiplicity	1jet	2jet	3jet	≥ 4jet
Pretag Events	94051	14604	2362	646
Mistag	399.0 ± 63.0	159.9 ± 25.3	47.2 ± 7.5	14.0 ± 2.2
$Wb\bar{b}$	340.9 ± 118.3	158.7 ± 54.2	32.1 ± 10.5	7.0 ± 2.8
$Wc\bar{c}$	101.6 ± 35.3	63.8 ± 21.8	16.0 ± 5.2	3.6 ± 1.5
Wc	325.7 ± 82.8	65.1 ± 17.0	8.3 ± 2.2	0.6 ± 0.2
$t\bar{t}$(6.7pb)	7.9 ± 1.4	49.2 ± 8.3	100.2 ± 16.9	116.8 ± 19.7
Single Top	19.1 ± 2.0	27.1 ± 2.9	5.6 ± 0.6	0.9 ± 0.1
Diboson/$Z^0 \to \tau\tau$	20.0 ± 3.3	23.3 ± 3.4	6.8 ± 1.4	1.7 ± 0.6
non-W QCD	139.1 ± 23.3	59.9 ± 10.4	16.4 ± 3.2	6.4 ± 1.4
Total Background	1353.3 ± 187.4	607.0 ± 83.6	232.6 ± 25.2	151.0 ± 20.5
Observed Events	1409	666	241	167

Table 6.8 Background estimate in exactly one SECVTX b-tagged events as a function of jet multiplicity.

Jet Multiplicity	1jet	2jet	3jet	$\geq$ 4jet
Pretag Events	94051	14604	2362	646
Mistag	139.7 ± 27.3	53.9 ± 10.7	15.7 ± 3.1	4.2 ± 0.8
$Wb\bar{b}$	306.9 ± 106.9	144.7 ± 49.4	29.9 ± 9.7	6.4 ± 2.5
$Wc\bar{c}$	63.1 ± 22.0	43.0 ± 14.7	8.7 ± 2.8	1.9 ± 0.8
Wc	185.7 ± 47.2	34.4 ± 9.0	3.4 ± 0.9	0.6 ± 0.2
$t\bar{t}$(6.7pb)	6.9 ± 1.2	42.0 ± 6.6	84.9 ± 12.8	98.6 ± 14.3
Single Top	16.7 ± 1.8	23.5 ± 2.4	4.8 ± 0.5	0.8 ± 0.1
Diboson/$Z^0 \rightarrow \tau\tau$	11.7 ± 2.2	14.2 ± 2.3	3.9 ± 0.9	1.0 ± 0.3
non-W QCD	84.2 ± 14.1	38.9 ± 6.7	12.1 ± 2.3	5.5 ± 1.2
Total Background	814.9 ± 140.7	394.4 ± 66.6	163.4 ± 18.7	118.9 ± 14.9
Observed Events	856	421	177	139

Table 6.9 Background estimate in events with exactly one SECVTX b-tagged jet that passes the NN filter as a function of jet multiplicity.

Jet Multiplicity	2jet	3jet	$\geq$ 4jet
Observed Events(pretag)	14604	2362	646
Mistag	3.5 ± 0.5	2.0 ± 0.3	1.2 ± 0.2
$Wb\bar{b}$	20.3 ± 7.0	5.7 ± 1.8	1.0 ± 0.4
$Wc\bar{c}$	3.3 ± 1.1	0.4 ± 0.1	0.1 ± 0.04
Wc	-	-	-
$t\bar{t}$(6.7pb)	10.4 ± 2.3	29.5 ± 6.4	45.5 ± 9.9
Single Top	4.2 ± 0.7	1.4 ± 0.2	0.3 ± 0.1
Diboson/$Z^0 \rightarrow \tau\tau$	1.2 ± 0.3	0.3 ± 0.1	0.1 ± 0.1
non-W QCD	1.4 ± 0.3	0.9 ± 0.2	0.3 ± 0.1
Total Background	44.2 ± 8.5	40.1 ± 6.8	48.6 ± 10.0
Observed Events	39	44	65

Table 6.10 Background estimate in at least two SECVTX b-tagged events as a function of jet multiplicity.

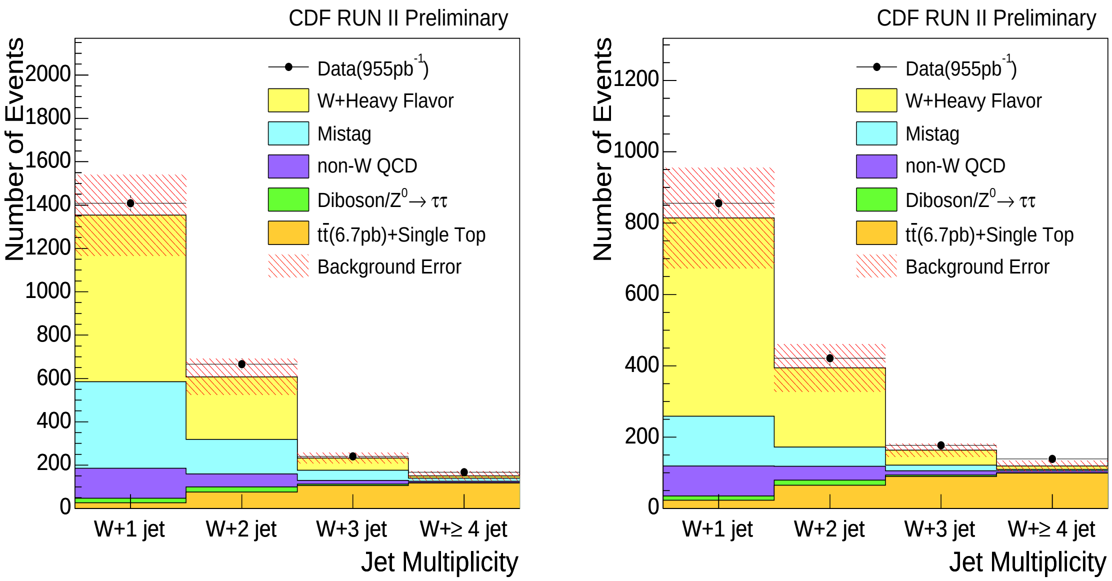

Figure 6.3 Number of events as a function of jet multiplicity obtained from exactly one SECVTX *b*-tagged events before(left) and after(right) applying the NN *b*-tagging requirement.

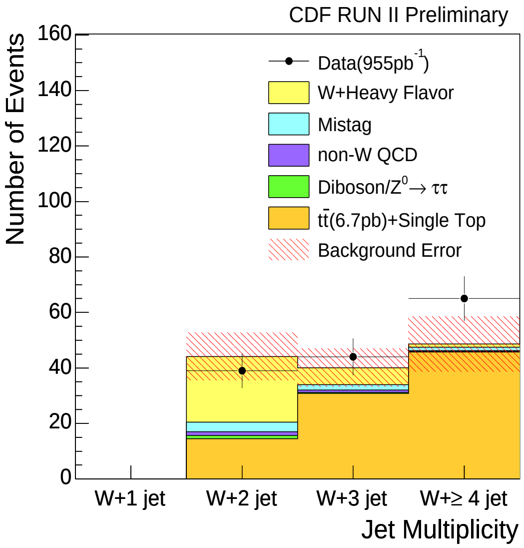

Figure 6.4 Number of events as a function of jet multiplicity obtained from at least two SECVTX *b*-tagged events.

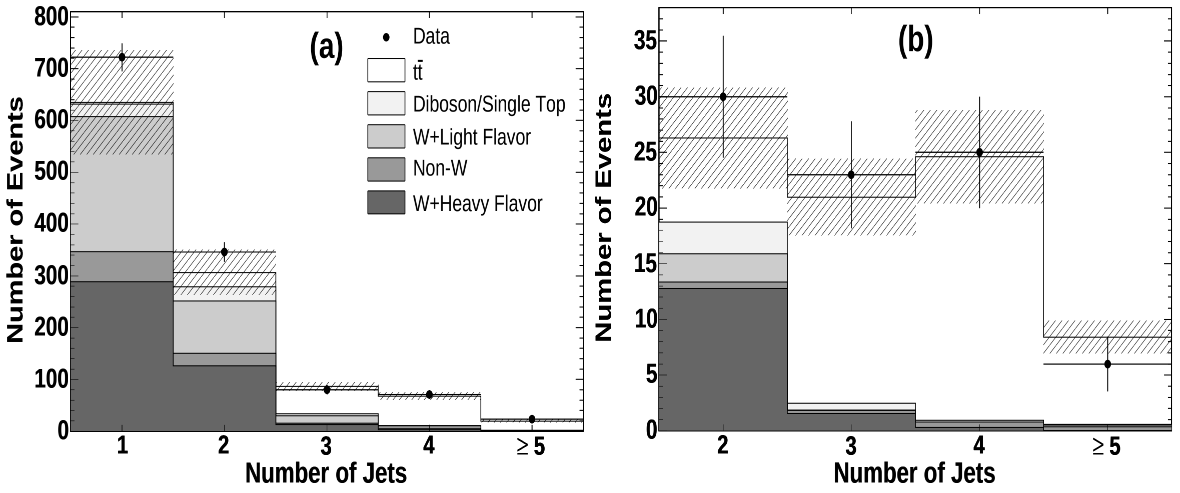

Figure 6.5 Summary of background and signal event yields versus number of jets in the event when requiring at least one b-tagged jet(left) and at least two b-tagged jets(right). The $t\bar{t}$ contribution is normalized to the measured cross section in each sample. The H_T requirement is released for events with fewer than three jets. The hashed region shows the uncertainty on the total expectation.

6.2 $t\bar{t}$ Production Cross Section Measurement

The final state of the most significant top quark pair production is $t\bar{t} \to (b\ell^+\nu)(\bar{b}\ell^-\bar{\nu})$, what is called lepton+4jet, process. Most of the lepton+jets top quark pair process are supposed to go into $W + 3$ or more jets bin. We have obtained background for lepton+jets events as a function of jet multiplicity, and this makes it possible if the background estimates are reasonable or not by measuring the $t\bar{t}$ production cross section because $W + 3$ or more jets bins are dominated by $t\bar{t}$ events after requiring at least one SECVTX b-tagged jet.

6.2.1 Measurement with 319 pb^{-1}

The $t\bar{t}$ production cross section measurements was performed using an integrated luminosity of 319 pb^{-1} under the assumption of top quark mass of 178 GeV/c^2 [70] with an additional $H_T > 200$ GeV selection[4] criteria to increase the purity of $t\bar{t}$ events. The background estimate summary is shown in **Fig.6.5**. The resulting cross sections from the two b-tagging strategies are obtained as:

$$\sigma_{t\bar{t}} = 8.7 \pm 0.9(\text{stat.})^{+1.1}_{-0.9}(\text{syst.})\text{pb} \qquad (\text{at least 1 } b\text{−tagged jet}), \tag{6.8}$$

$$\sigma_{t\bar{t}} = 10.1^{+1.6}_{-1.4}(\text{stat.})^{+2.0}_{-1.3}(\text{syst.})\text{pb} \qquad (\text{at least 2 } b\text{−tagged jets}). \tag{6.9}$$

---

[4] H_T is defined as a scalar some of all physics objects.

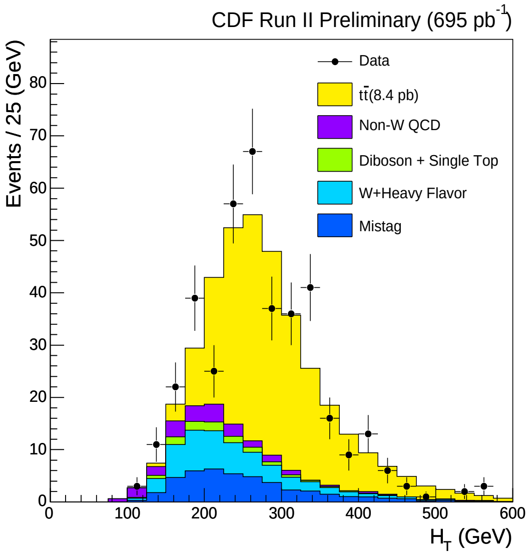

Figure 6.6 H_T distribution in $W+3$ or 4 jet events with at least one b-tagged jets.

The observed production cross sections are consistent with the theoretical cross section of $\sigma_{t\bar{t}} = 6.1^{+0.6}_{-0.8}$ pb for top quark mass of 178 GeV/c^2.

6.2.2 Updated Measurement with 695 pb^{-1}

As discussed above, we already estimated background in W+jets events as a function of jet multiplicity. The $t\bar{t}$ contribution to background must be removed for the $t\bar{t}$ cross section measurement. The H_T distribution in at least one tagged b-jet events is shown in **Fig.6.6** with 695 pb^{-1} of data [5]. We also applied additional $H_T > 200$ GeV selection criteria for W+3 or more jets events, and obtained background estimate of at least one and two b-tagged jets events as shown in **Fig.6.7**[71] separately. The observed cross sections are

$$\sigma_{t\bar{t}} = 8.2 \pm 0.6(\text{stat.}) \pm 1.0(\text{syst.}), \quad \text{(at least 1 } b\text{−tagged jet)}, \tag{6.10}$$

$$\sigma_{t\bar{t}} = 8.8^{+1.2}_{-1.1}(\text{stat.})^{+2.0}_{-1.3}(\text{syst.}) \quad \text{(at least 2 } b\text{−tagged jets)}, \tag{6.11}$$

---

[5] The $t\bar{t}$ production cross section measurement was performed when only 695 pb^{-1} was available, and it is not officially updated to 1 fb^{-1} at present.

for top quark mass[6] at 175 GeV/c^2. Those measurements are consistent with the theoretical cross section of $\sigma_{t\bar{t}} = 6.7^{+0.7}_{-0.9}$ pb for top quark mass of 175 GeV/c^2.

Furthermore, we have applied a Neural Network b-tagging to W+jets events in the previous section. It is a good cross check to measure $t\bar{t}$ production cross section with the Neural Network b-tagging requirement to see if our background modeling works well when Neural Network b-tagging is applied. The summary of background estimate requiring at least one b-tagged jet that passes Neural Network filter is shown in **Fig.6.8**, and $t\bar{t}$ production cross section is measured as:

$$\sigma_{t\bar{t}} = 8.5 \pm 0.6(\text{stat.}) \pm 1.0(\text{syst.}). \tag{6.12}$$

This result is consistent before applying Neural Network b-tagging and theoretical cross section of $\sigma_{t\bar{t}} = 6.7^{+0.7}_{-0.9}$ pb. Accordingly, the background modeling of the Neural Network b-tagging is validated by the fact that it results in a consistent $t\bar{t}$ cross section measurement before applying that.

---

[6] In the measurement with 319 pb^{-1}, the world average of the top quark mass was about 178 GeV/c^2, and it was used for geometrical and kinematic acceptance calculation. After using the latest data up to 750 pb^{-1}, the measured top quark mass becomes 172.5 ± 2.3 GeV/c^{2}at CDF. And top mass of 175 GeV/c^{2}is used as a milestone for other measurement.

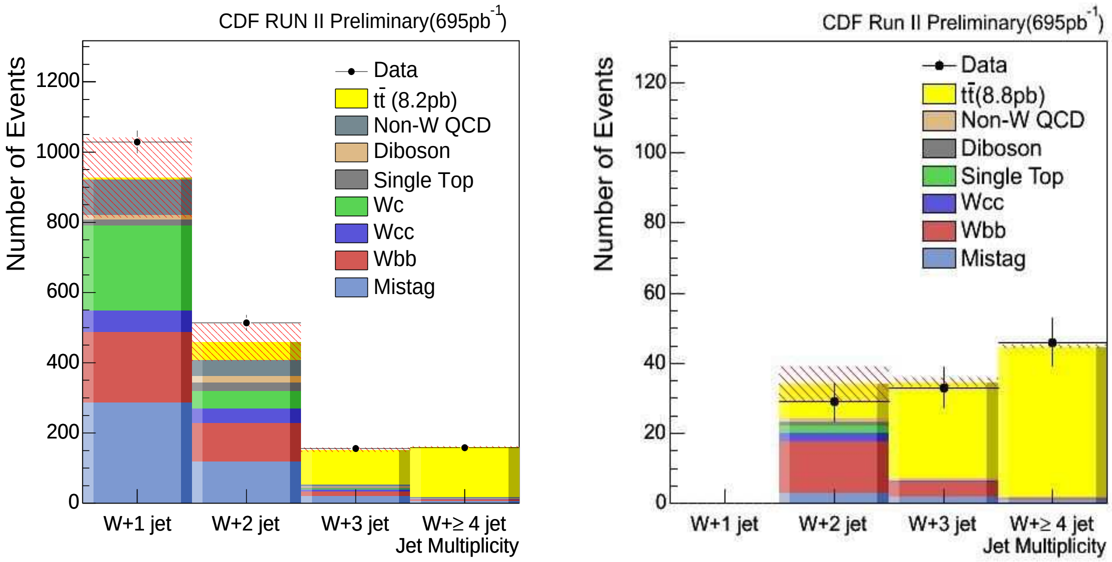

Figure 6.7 The expected number of W+jets events with at least one SECVTX b-tagged jet(left) and at least two SECVTX b-tagged jets(right). In the at least one b-tagged sample, $H_T > 200$ GeV selection criteria is required. The top prediction is scaled to our measured value of 8.2 pb(left) and 8.8 pb(right). The cross section measurement is only based on events with 3 or more jets.

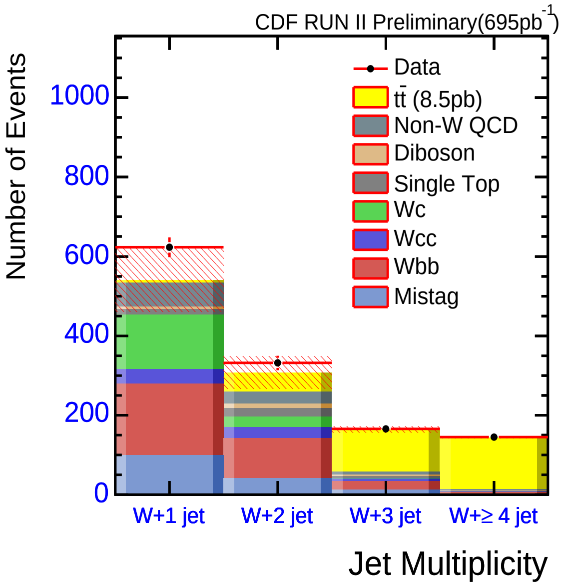

Figure 6.8 The expected number of W+jets events with at least one b-tagged jet that passes the Neural Network b-tagging condition. The top pair prediction is scaled to the measured value of 8.5 pb. The cross section measurement is only based on events with 3 or more jets.

Chapter 7

Search for Higgs Boson Production

Events selection and background estimation for the search for $WH \to \ell\nu b\bar{b}$ process is completed up to previous chapter. For the purpose of the search, signal acceptance and its systematic uncertainties are discussed first. Several b-tagging options are considered in this thesis, and it is also important to find the best way of the search a priori. A sensitivity study is considered. Then comparison between the Standard Model background prediction and data is performed.

7.1 Acceptance

The evaluation of the number of expected events of undiscovered process is based on theoretical cross section, branching ratio and a meaningful inputs of the parameters that the process depends on. In $WH \to \ell\nu b\bar{b}$ process, the dynamics is well defined by the Standard Model and it can be generated by Monte Carlo generators. In this thesis, PYTHIA[72] is used to generate the signal samples. However, the Standard Model Higgs boson is not discovered yet and its mass is an arbitrary input parameter. In accordance with other experiments, as discussed in **Sec.2.5**, a constraint on Higgs boson mass

$$114.4 < m_H < 199 \ (\mathrm{GeV/c^2}) \text{ at } 95\% \text{ C.L.}, \tag{7.1}$$

is obtained. Branching ratio of Higgs boson decay is dominated by the mode of $H \to W^+W^-$ for $m_H > 135$ GeV/c^2 instead of $H \to b\bar{b}$(see **Fig.2.3**). Therefore, Higgs boson mass at $m_H = 110, 115, 120, 130, 140$ and 150 GeV/c^2 is considered. The number of expected $WH \to \ell\nu b\bar{b}$ events($N_{WH\to\ell\nu b\bar{b}}$) is obtained by:

$$N_{WH\to\ell\nu b\bar{b}}(m_H) = \epsilon_{WH\to\ell\nu b\bar{b}}(m_H) \cdot \int dt\mathcal{L} \cdot \sigma(p\bar{p} \to WH|m_H) \cdot Br(H \to b\bar{b}|m_H), \tag{7.2}$$

Higgs Mass	Expected Signal Events			
(GeV/c^2)	Pretag	=1 tag	=1 tag & NNtag	$\geq$ 2 tag
110	4.81±0.34	2.15 ± 0.18	1.87 ± 0.18	0.66 ± 0.13
115	3.99±0.28	1.80 ± 0.15	1.56 ± 0.15	0.54 ± 0.11
120	3.23±0.23	1.45 ± 0.12	1.26 ± 0.12	0.44 ± 0.09
130	2.05±0.15	0.93 ± 0.08	0.81 ± 0.08	0.28 ± 0.06
140	1.03±0.07	0.46 ± 0.04	0.40 ± 0.04	0.15 ± 0.03
150	0.40±0.03	0.18 ± 0.02	0.16 ± 0.02	0.06 ± 0.01

Table 7.1 Expected $WH \to \ell\nu b\bar{b}$ signal events in W+2jets event for various b-tagging options, where "tag" and "NNtag" stand for SECVTX b-tagging and Neural Network b-tagging.

where $\epsilon_{WH\to\ell\nu b\bar{b}}$, $\int dt\mathcal{L}$, $\sigma(p\bar{p} \to WH)$ and $Br(H \to b\bar{b})$ are event detection efficiency, integrated luminosity, production cross section and branching ratio respectively. $\int dt\mathcal{L}$ is obtained by luminosity measurement as shown in **Table 5.1**. The production cross section and branching ratio are calculated to the precision of Next to Leading Order(NLO)[13, 14] at considered Higgs boson mass points. $\epsilon_{WH\to\ell\nu b\bar{b}}$, which is also called "acceptance", consists of all of the experimental aspects for detection and event selection. It is broken down into sub-factors as:

$$\epsilon_{WH\to\ell\nu b\bar{b}} = \epsilon_{z_0} \cdot \epsilon_{\text{trigger}} \cdot \epsilon_{\text{lepton ID}} \cdot \epsilon_{b\text{tag}} \cdot \epsilon_{\text{kinematics}} \cdot \left(\sum_{l'=e,\mu,\tau} Br(W \to l'\nu) \right), \tag{7.3}$$

where ϵ_{z_0}, $\epsilon_{\text{trigger}}$, $\epsilon_{\text{lepton ID}}$, $\epsilon_{b\text{tag}}$ and $\epsilon_{\text{kinematics}}$ are efficiencies to meet the requirements of primary vertex, trigger, lepton ID, b-tagging and kinematics, which includes Jets' E_T and η, missing E_T and the number of jet and lepton, as listed in **Sec.5.2**. ϵ_{z_0} is obtained from data, and others are calculated using Monte Carlo samples. The overall acceptances for various b-tagging options including all systematic uncertainties as a function of Higgs boson mass are shown in **Fig.7.1**(details of systematic uncertainties are discussed in the next section).

The expected number of $WH \to \ell\nu b\bar{b}$ signal events is estimated by Eq.7.2 at each Higgs boson mass point. The expectations for various b-tagging strategies are shown in **Table 7.1**. Neural Network b-tagging keeps about 90% of signal acceptance while it reduces about 65% of total background in W+2jet events according to **Tables 6.8** and **6.9**.

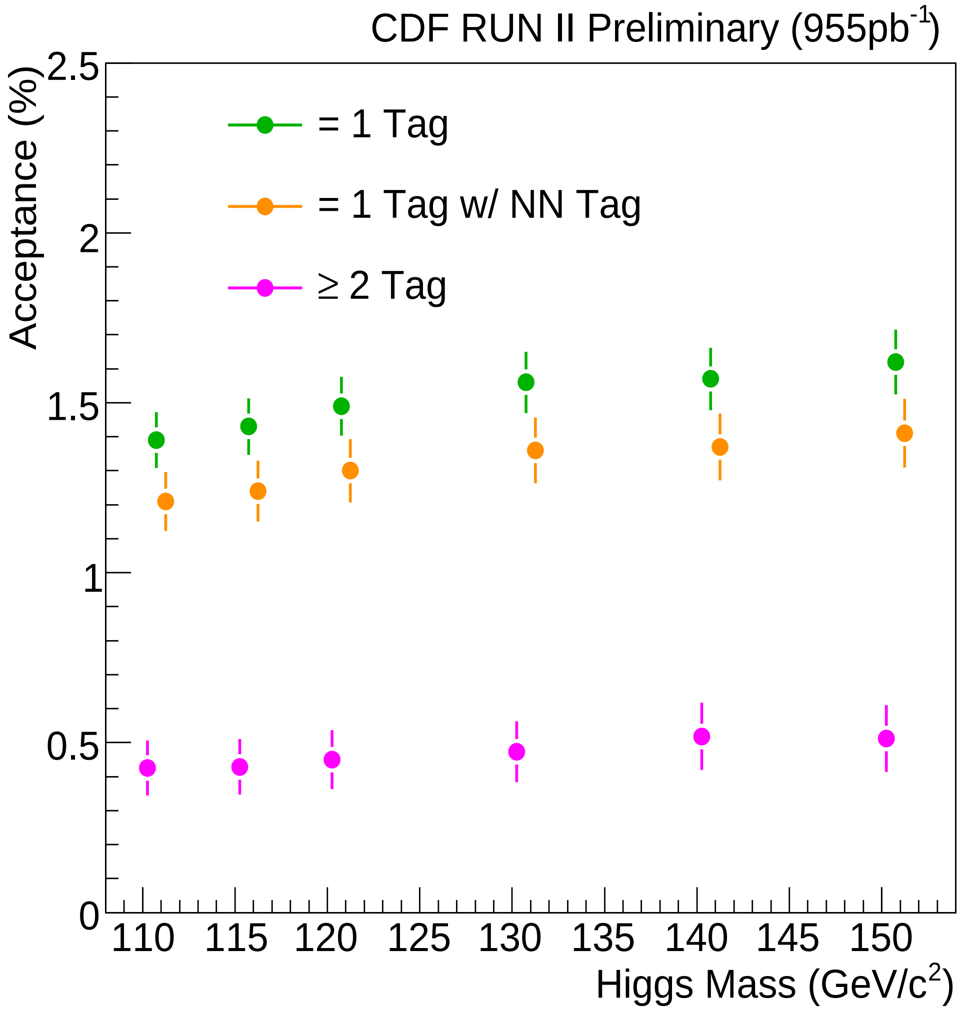

Figure 7.1 The summary of acceptance of the process $WH \to \ell\nu b\bar{b}$ in W+2jet bin for various b-tagging strategies as a function of Higgs boson mass. Error bar of each mass point stands for systematic uncertainty.

7.2 Systematics

The systematic uncertainties in acceptance include jet energy scale, initial and final state radiation, lepton ID, trigger efficiencies and b-tagging scale factor. Individual sources of total systematic uncertainties are discussed in detail.

- Lepton ID
  Measured for each lepton type, CEM electron, CMUP and CMX muon. 2% uncertainty is assigned[73–76].

- Trigger
  Obtained for individual trigger types, and 1% uncertainty is enough for the triggers considered in this thesis[77, 78].

- Initial and Final State Radiation (ISR/FSR)
  ISR and FSR systematic uncertainty are estimated by changing the parameters related to ISR and FSR from nominal values to half and double. The difference from the nominal acceptance is taken as the systematic uncertainly.

- Parton Distribution Function (PDF)[79–81]
  The uncertainty in the incoming partons' energy in proton and antiprotons. CTEQ5L is used as the nominal PDF, which is Leading Order(LO). CTEQ PDF is parametrized by 20 eigen vectors. An NLO version of PDF, CTEQ6M, provide a 90% confidence interval of each eigen vector. Using the value of each eigen vector at 90% edge of the confidence interval, nominal PDF is reweighted and corresponding acceptance is computed. The differences between nominal and reweighted acceptances are added in quadrature, and it is assigned as the systematic uncertainty.

- Jet Energy Scale(JES)
  Based on uncertainty of single jet energy. Jet energies in WH Monte Carlo samples are shifted by $\pm 1\sigma$ and the deviation from the nominal acceptance is taken as the systematic uncertainty.

- b-tagging
  The systematic uncertainty of SECVTX b-tagging is based on its scale factor uncertainty discussed in **Sec.4.1**. When Neural Network b-tagging is applied, the scale factor uncertainty from NN b-tagging(see **Sec.4.2**) is added to that of SECVTX in quadrature.

Total systematic uncertainty is obtained by adding each source in quadrature. The systematic uncertainties for various b-tagging options are summarized in **Table 7.2**.

source	uncertainty (%)		
	= 1 Tag	= 1 Tag & NNtag	$\geq$ 2 Tag
Lepton ID	∼2%	∼2%	∼2%
Trigger	<1%	<1%	<1%
ISR	1.5%	1.8%	4.3%
FSR	2.8%	3.2%	8.6%
PDF	1.6%	1.7%	2.0%
JES	2.3%	2.3%	3.0%
b-tagging	3.8%	5.3%	16%
Total	5.8%	7.2%	19.1%

Table 7.2 Systematic uncertainties for various b-tagging conditions. "Tag" and "NNtag" represent tight SECVTX and Neural Network b-tagging respectively.

7.3 Sensitivity

The Standard Model predicts that the decay width of Higgs boson is quite small, expected about a few MeV/c^2 scale[72], and it results in a sharp peak in dijet mass distribution. There are various b-tagging options, e.g. at least one or exactly one SECVTX b-tagging with or without Neural Network b-tagging filter, at least two SECVTX b-taggings, and combined use of those exactly one and at least two b-taggings.

Background estimate and expected number of $WH \to \ell\nu b\bar{b}$ signal events are obtained in **Secs.6.1** and **7.1** respectively. The best way of the search is chosen by using significance defined as $S/\sqrt{B}$ where S and B are the number of expected signal and background events. In this analysis, S and B are counted within a window which gives the best significance in dijet mass distribution found by varying the window peak and width for each b-tagging strategy. A comparison of significance between various b-tagging options, shown in **Fig.7.2**, provides an a priori milestone that predicts which option gives the best result. The improvement from the Neural Network b-tagging is seen in significance. By comparing the significance obtained from exactly one SECVTX tag with and without NN b-tagging filter, about 10% sensitivity improvement is found.

The significance in at least two SECVTX tagged events is almost the same as that in at least one tagged events before applying Neural Network filter. Accordingly, the separated use of exactly one and two SECVTX tagged events should result in another sensitivity improvement. The significance from the combination is obtained as:

$$\mathrm{Sig}(=1\mathrm{tag}\&\& \geq 2\mathrm{tag}) = \sqrt{\mathrm{Sig}(=1\mathrm{tag})^2 + \mathrm{Sig}(\geq 2\mathrm{tag})^2}. \tag{7.4}$$

This combined use of two separated b-tagging information provides a significant improve-

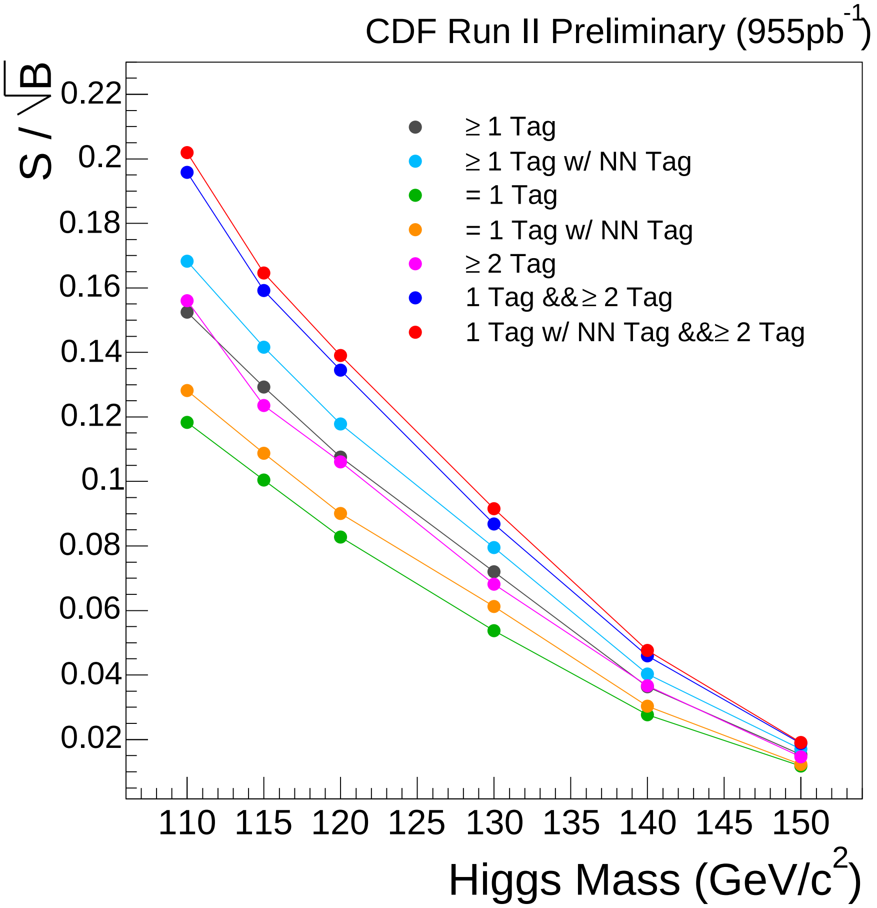

Figure 7.2 Comparison of significance obtained from various b-tagging strategies. "Tag" and "NN Tag" represent SECVTX and Neural Network b-tagging respectively. The symbol "&&" means a combined use of the two strategies.

ment on the significance as shown in **Fig.7.2**. The improvement from "≥ 1 tag && w/ NNtag" is about 20% compared to "= 1Tag w/ NN Tag && ≥ 2 Tag", which shows the best sensitivity without considering the combined use of two tagging conditions. Therefore, the analysis is focused on the event selection types of exactly one SECVTX b-tagging with Neural Network filter and at least two SECVTX b-tagging.

7.4 Kinematics

In this section, comparison of various kinematic distributions and dijet mass distributions between the Standard Model background expectation and observed data is performed. The Standard Model Higgs boson is expected to have a sharp mass peak in dijet mass distribution, thus dijet mass distribution is the most interesting and important distribution for the search. However, the background modeling, event selection, and the effect of Neural Network b-tagging on overall event kinematics should be validated to say something out of the dijet mass distribution. In this analysis, the following kinetic distributions are shown for the purposes.

- Transverse energy(E_T) of leading jet[1], 2nd leading jets and lepton
- Pseudo-rapidity(η) of leading jet, 2nd leading jet and lepton
- Azimuthal angle(ϕ) of leading jet, 2nd leading jet and lepton
- Missing transverse energy($\not\!\!E_T$)
- Scalar sum of E_T of jets, lepton and $\not\!\!E_T$, what is called "H_T"
- Transverse mass of W boson defined as

$$M_T = (E_\ell + \not\!\!E_T)^2 - (\boldsymbol{p}_T^{(\ell)} + \not\!\!\boldsymbol{E_T})^2. \tag{7.5}$$

- Transverse angle between leading jet and $\not\!\!E_T$
- Distance in η-ϕ plane between two jets defined as

$$\Delta R(\mathrm{jet1} - \mathrm{jet2}) = \sqrt{(\eta_{\mathrm{jet2}} - \eta_{\mathrm{jet1}})^2 + (\phi_{\mathrm{jet2}} - \phi_{\mathrm{jet1}})^2}. \tag{7.6}$$

The distributions of E_T, η and ϕ are the kinematics of each observed particles. Agreements of those distributions are the basis to see other kinetic distributions. Missing E_T and H_T are related with all other observables because those variables are correlated with E_T of jets and lepton. Thus the agreement between the Standard Model prediction and data justifies the event reconstruction and background modeling. Distributions of W transverse mass and transverse angle between leading jet and $\not\!\!E_T$ are especially to check if the non-W QCD background modeling is valid. Finally the distance in η-ϕ plane between two jets is directly correlated with dijet mass and it is a good check for a kinematics in dijet system.

---

[1] In this analysis, jets are in the order of magnitude of E_T

First of all, it should be checked to see if the event selection and background modeling works well before applying Neural Network b-tagging. The kinetic distributions using events with exactly one SECVTX b-tagged jet (before using Neural Network b-tagging) are shown in **Figs.7.3-7.9**. According to those distributions, observed data is in a fairly good agreement with the Standard Model background prediction. This agreement justifies the background modeling and event selection are working well and in our handle.

Next, in addition to exactly one SECVTX b-tagging requirement, Neural Network b-tagging is applied. The corresponding kinetic distributions are shown in **Figs.7.10-7.16**. The agreement between data and Standard Model background prediction is at the same level as before applying Neural Network b-tagging. This fact justifies that Neural Network b-tagging is working well and also our understanding of the background compositions should be correct in a good precision.

The kinetic distributions in events including at least two SECVTX b-tagged jets are shown in **Figs.7.17-7.23**. The background contamination is quite small in this b-tagging option as shown in **Fig.6.4** and **Table 6.10**. The agreement between data and background prediction is quite well.

Based on those 3 cases, background is under control in all of the b-tagging condition considered in this analysis. Finally the dijet mass distributions are shown in **Figs.7.24-7.26** for each event selection types. The dijet mass distributions are consistent with the standard model background prediction, and there is no significance mass peak that indicate Higgs boson signal. Therefore, a constraint on the Higgs boson production is discussed in the next chapter.

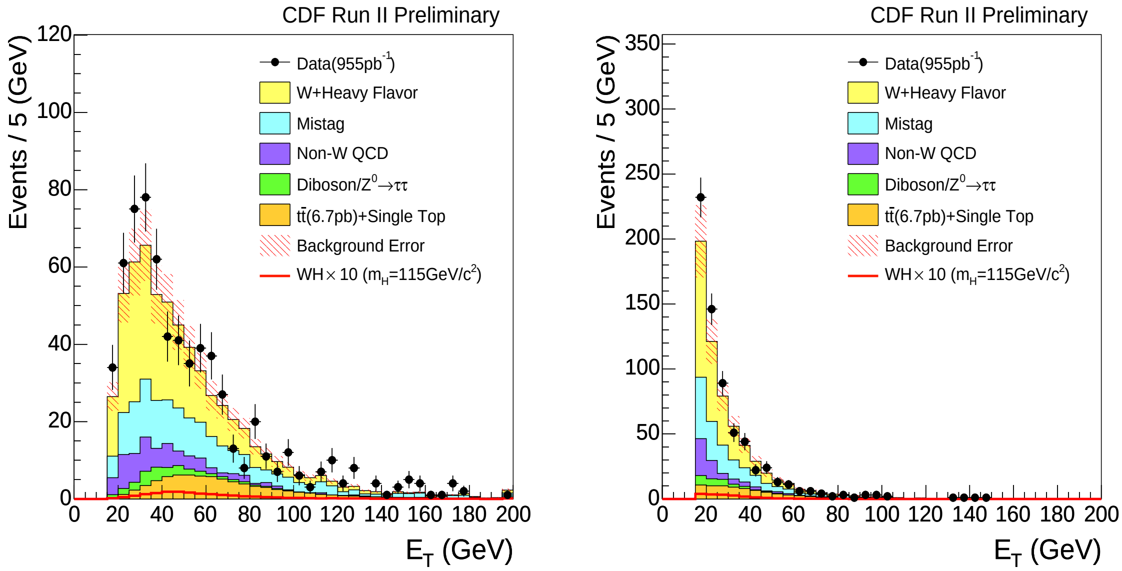

Figure 7.3 The leading(left) and second leading(right) jet E_T distributions in exactly one SECVTX b-tagged events.

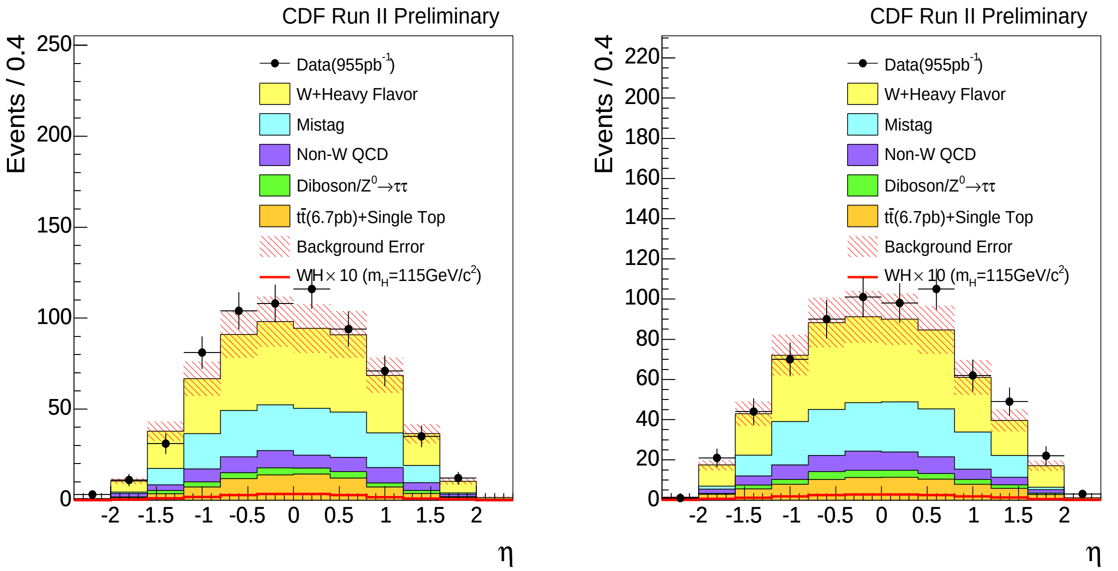

Figure 7.4 The leading(left) and second leading(right) jet η distributions in exactly one SECVTX b-tagged events.

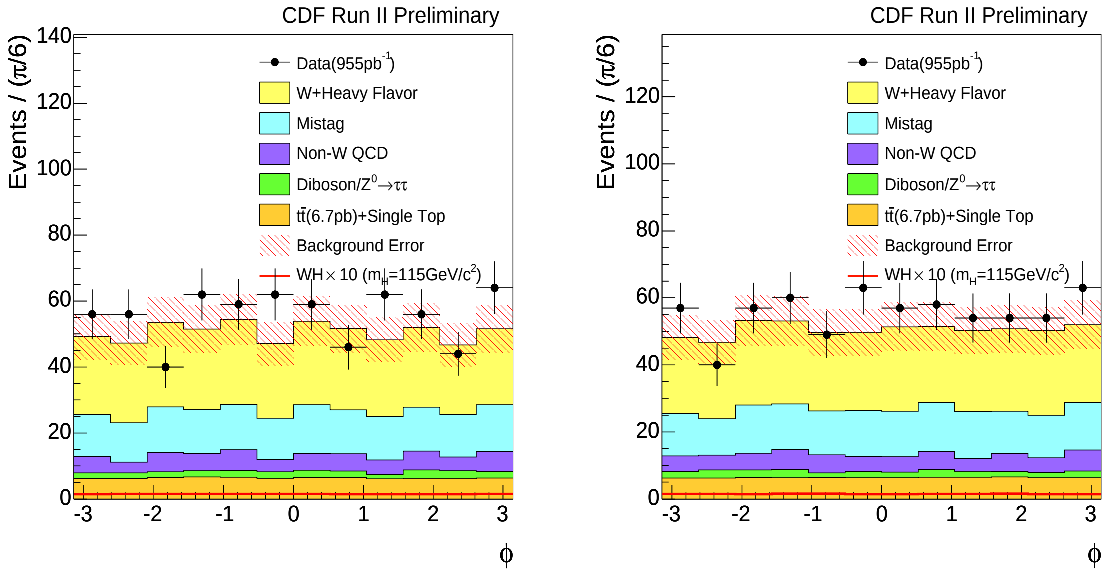

Figure 7.5 The leading(left) and second leading(right) jet ϕ distribution in exactly one SECVTX b-tagged events.

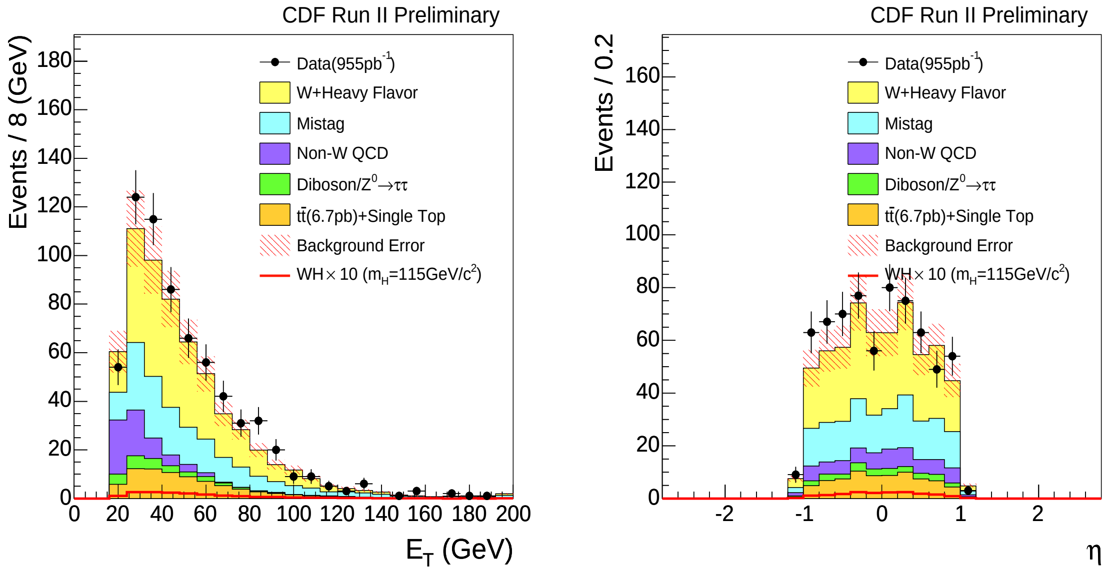

Figure 7.6 Lepton E_T(left) and η(right) distributions in exactly one SECVTX b-tagged events.

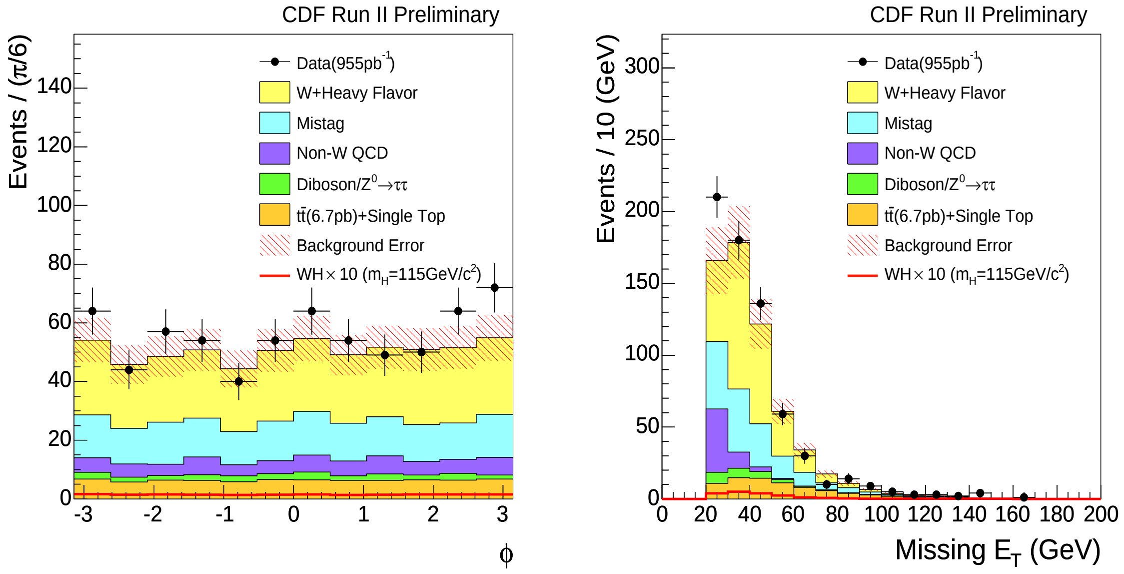

Figure 7.7 Lepton ϕ(left) and $\not{E}_T$(right) distributions in exactly one SECVTX b-tagged events.

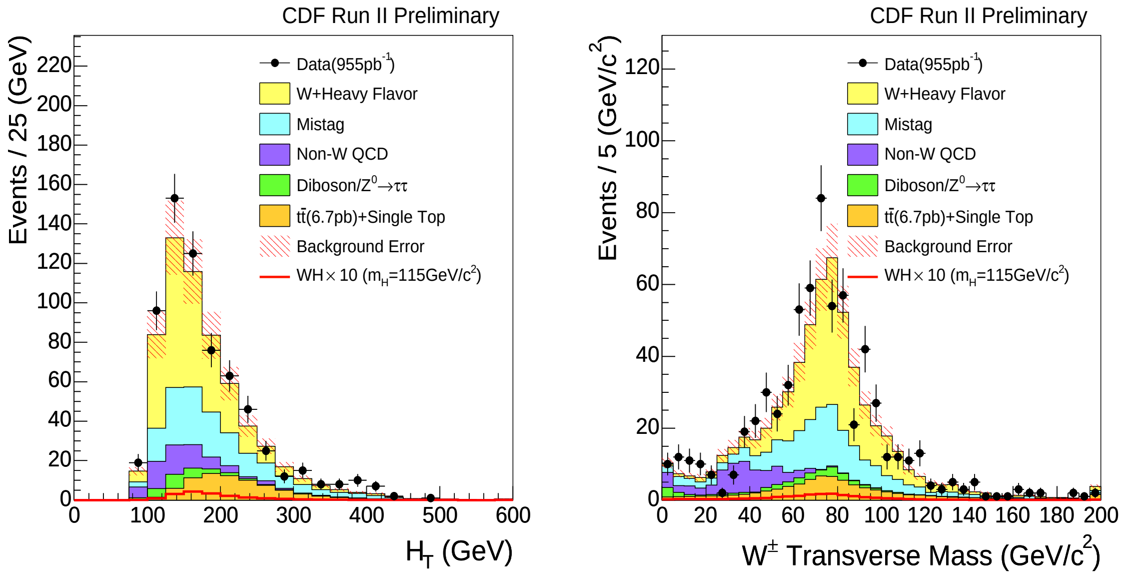

Figure 7.8 H_T(left) and M_T(right) distributions in exactly one SECVTX b-tagged events.

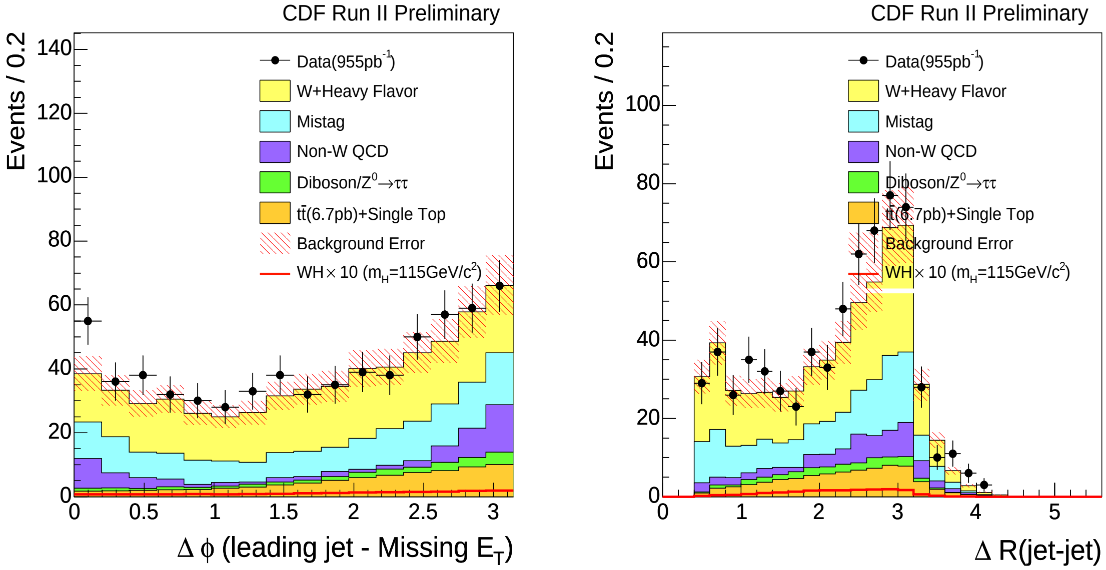

Figure 7.9 $\Delta\phi$(1st leading jet-MET)(left) and $\Delta R(\text{jet1} - \text{jet2})$(right) distributions in exactly one SECVTX b-tagged events.

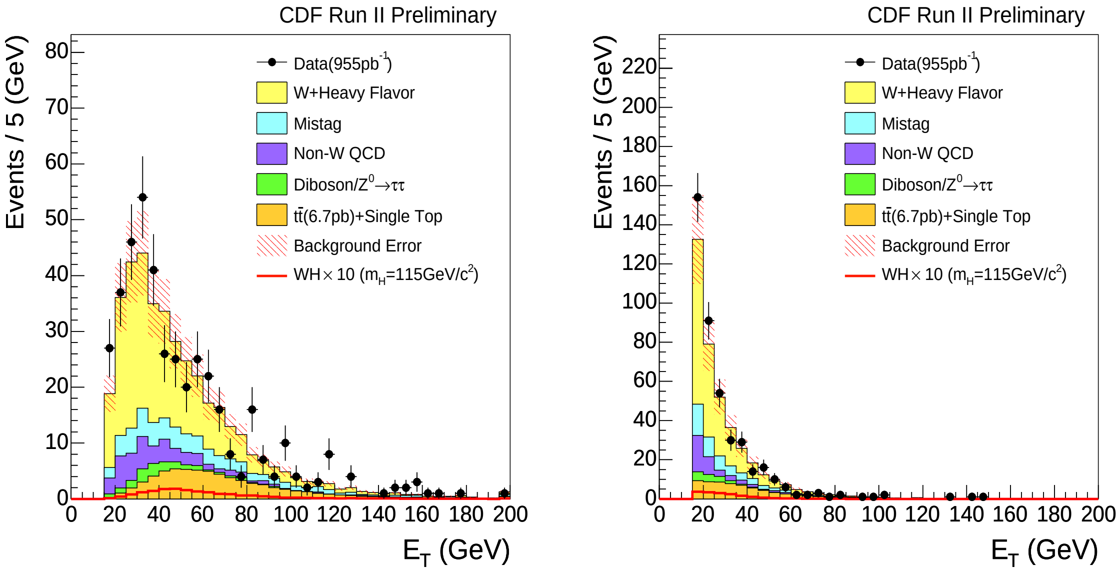

Figure 7.10 The leading(left) and second leading(right) jet E_T distributions in exactly one SECVTX and Neural Netwotk b-tagged events.

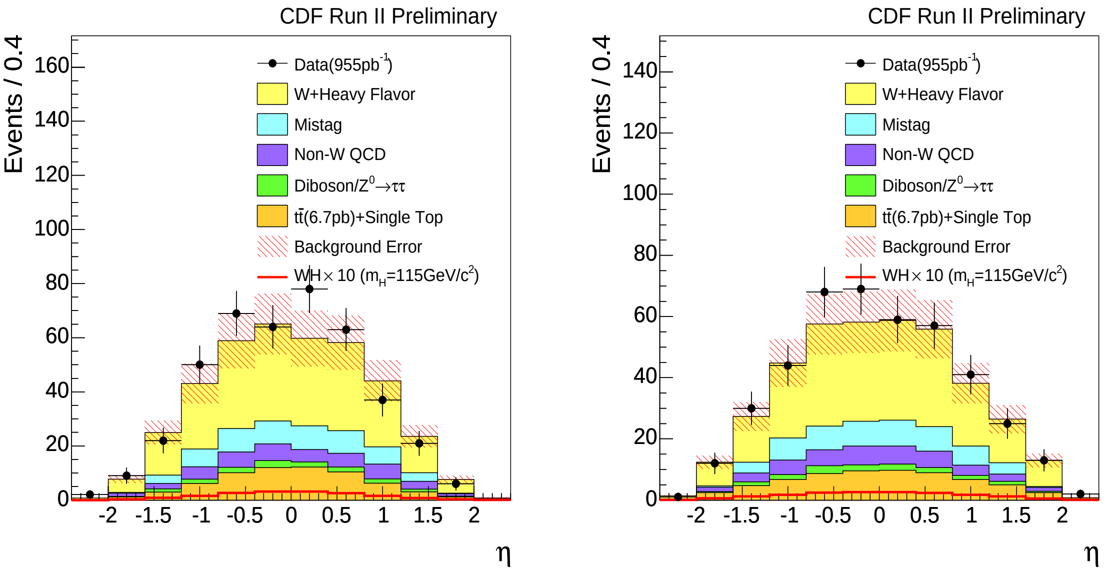

Figure 7.11 The leading(left) and second leading(right) jet η distributions in exactly one SECVTX and Neural Netwotk b-tagged events.

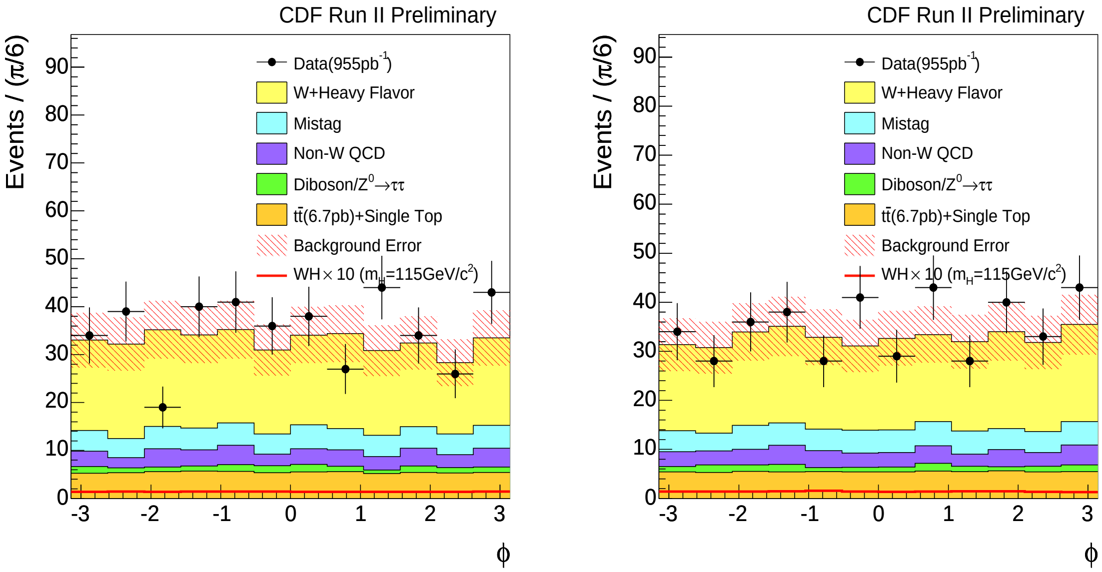

Figure 7.12 The leading(left) and second leading(right) jet ϕ distribution in exactly one SECVTX and Neural Netwotk b-tagged events.

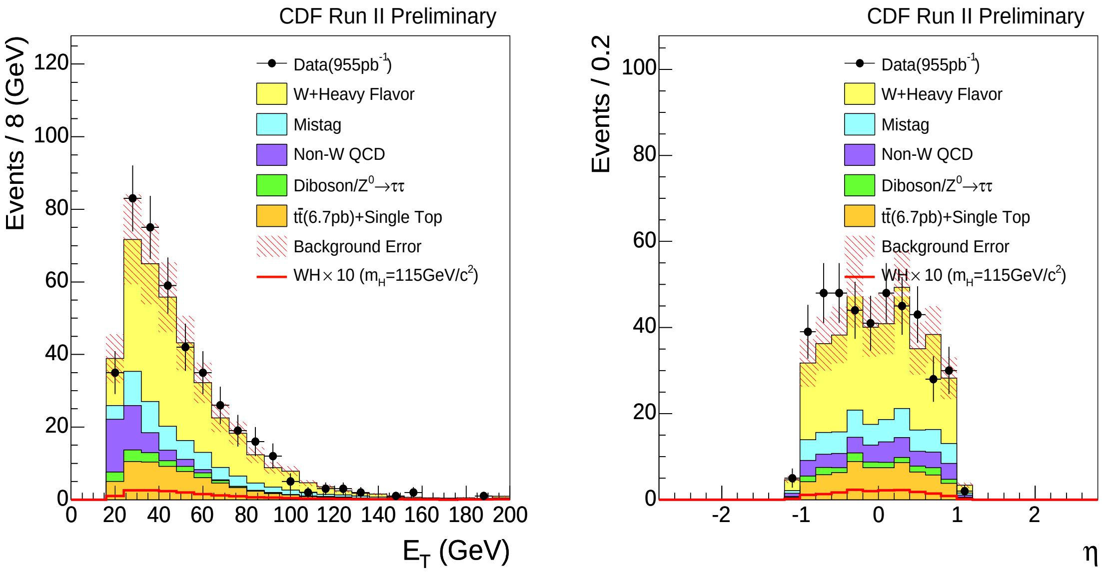

Figure 7.13 Lepton E_T(left) and η(right) distributions in exactly one SECVTX and Neural Netwotk b-tagged events.

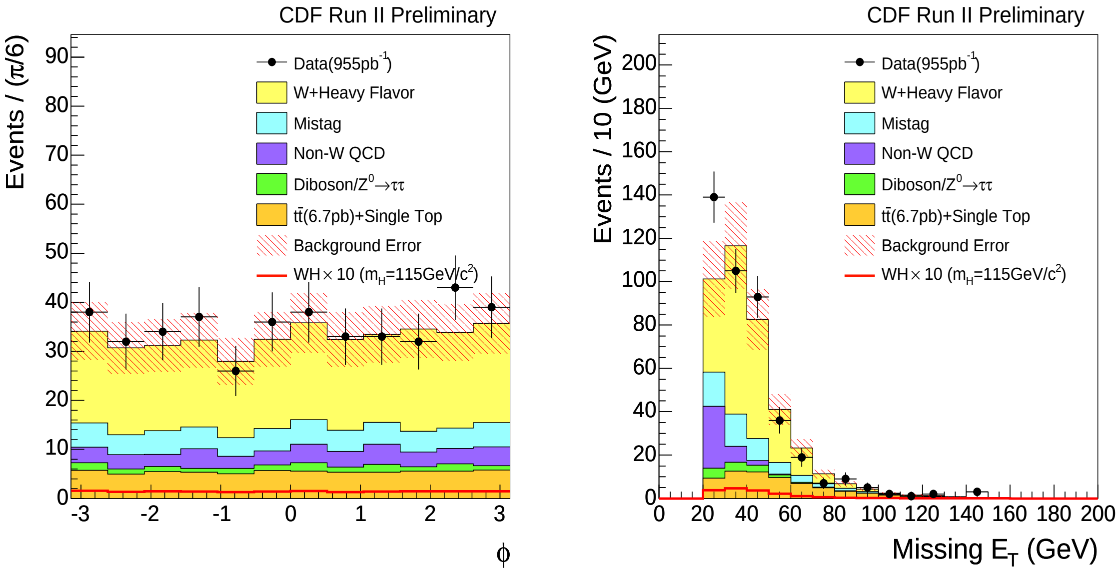

Figure 7.14 Lepton ϕ(left) and $\not\!\!E_T$(right) distributions in exactly one SECVTX and Neural Netwotk b-tagged events.

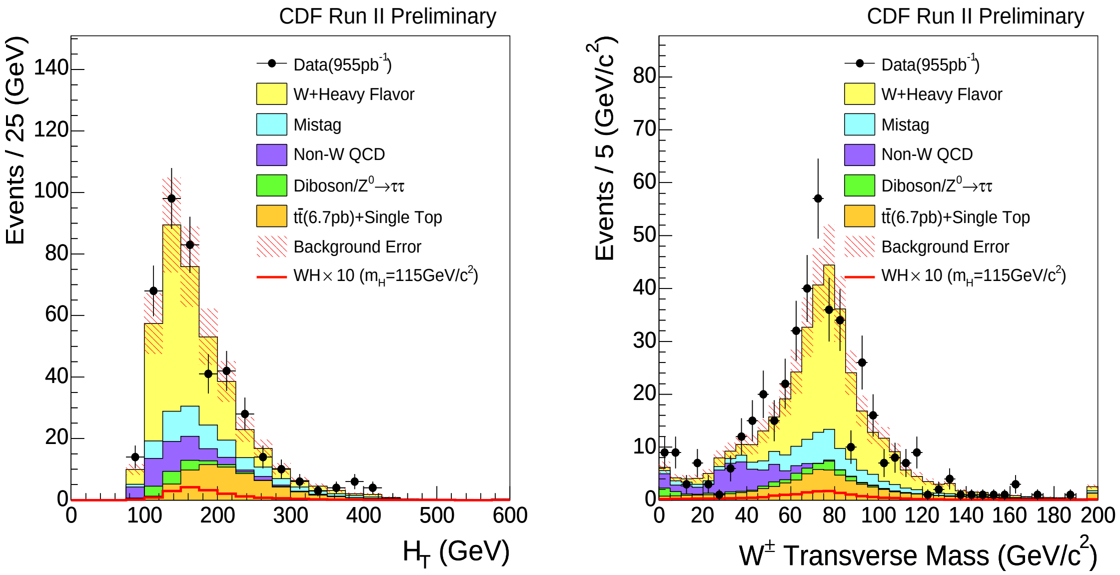

Figure 7.15 H_T(left) and M_T(right) distributions in exactly one SECVTX and Neural Netwotk b-tagged events.

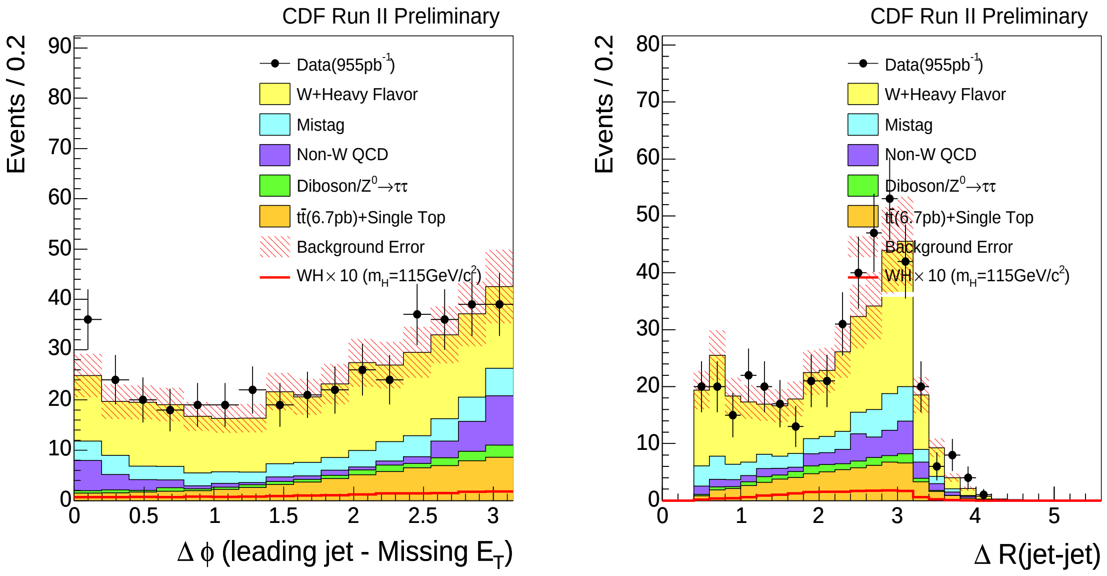

Figure 7.16 $\Delta\phi$(1st leading jet-MET)(left) and ΔR(jet1 − jet2)(right) distributions in exactly one SECVTX and Neural Netwotk b-tagged events.

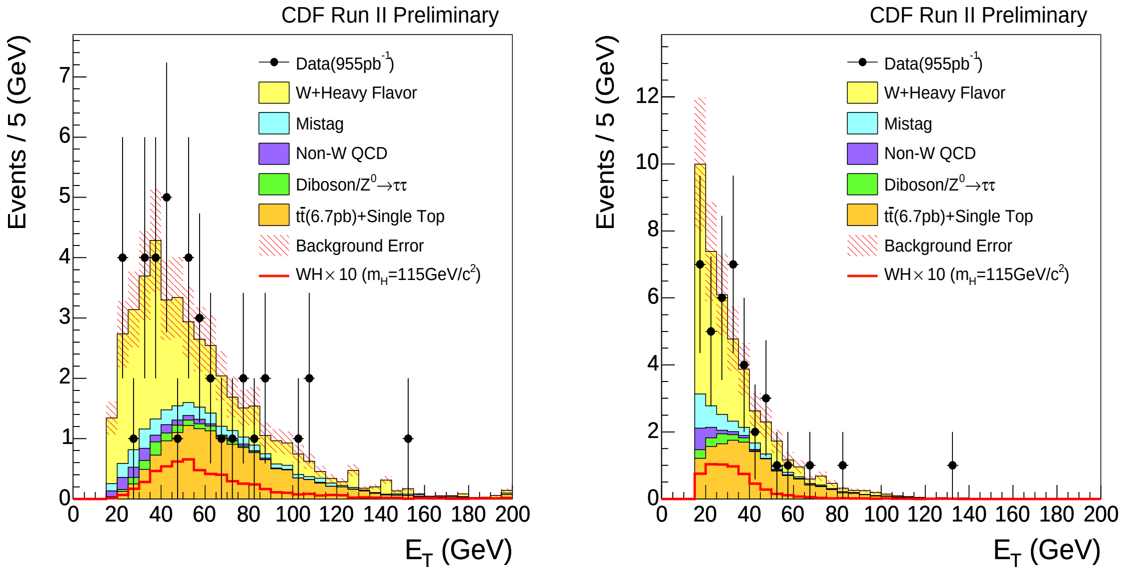

Figure 7.17 The leading(left) and second leading(right) jet E_T distributions in at least two SECVTX b-tagged events.

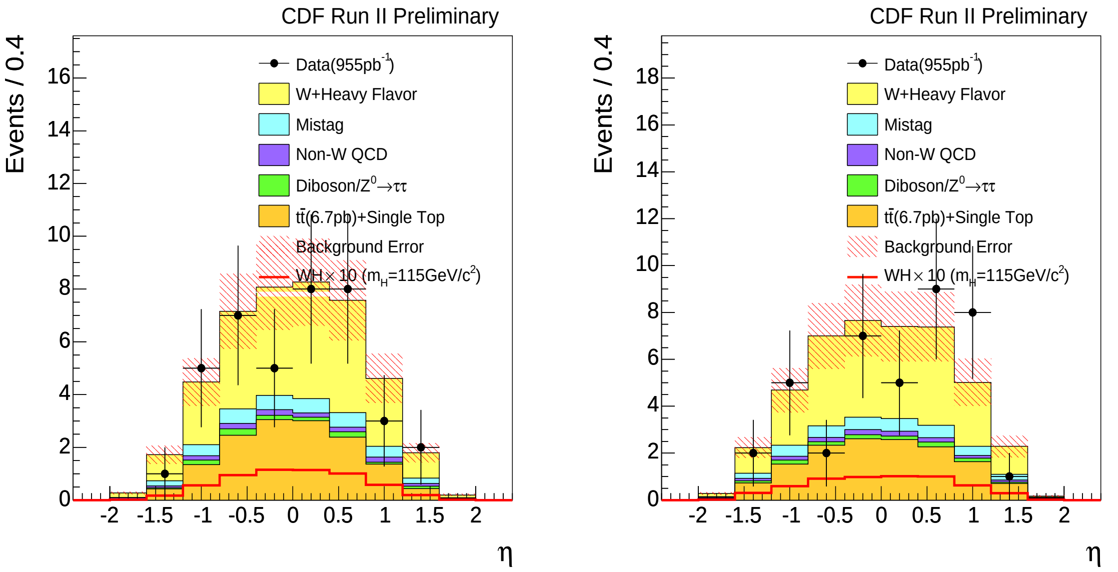

Figure 7.18 The leading(left) and second leading(right) jet η distributions in at least two SECVTX b-tagged events.

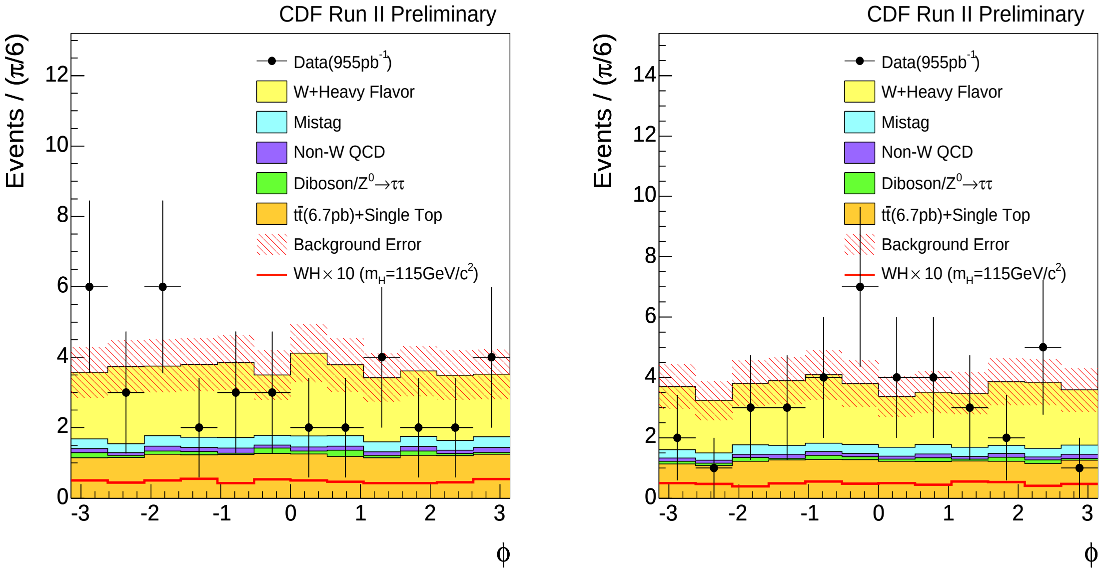

Figure 7.19 The leading(left) and second leading(right) jet ϕ distribution in at least two SECVTX b-tagged events.

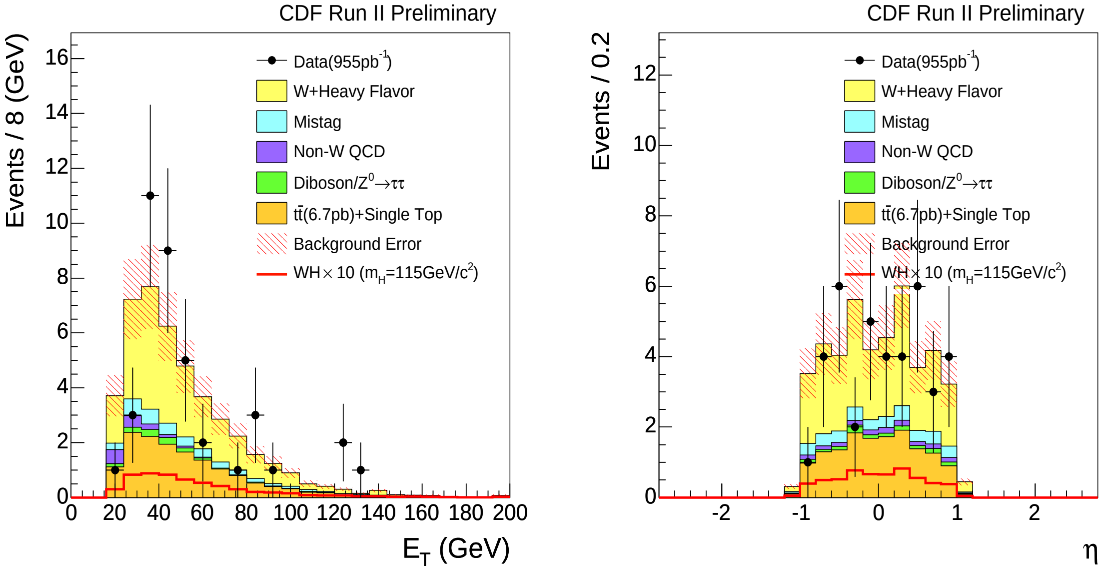

Figure 7.20 Lepton E_T(left) and η(right) distributions in at least two SECVTX b-tagged events.

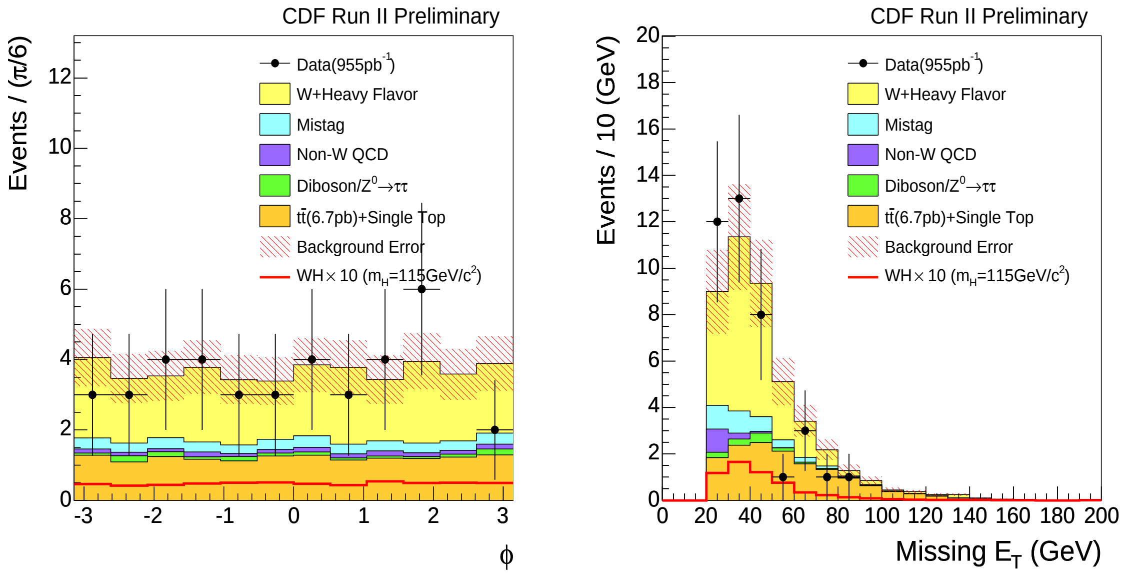

Figure 7.21 Lepton ϕ(left) and $\not{E}_T$(right) distributions in at least two SECVTX b-tagged events.

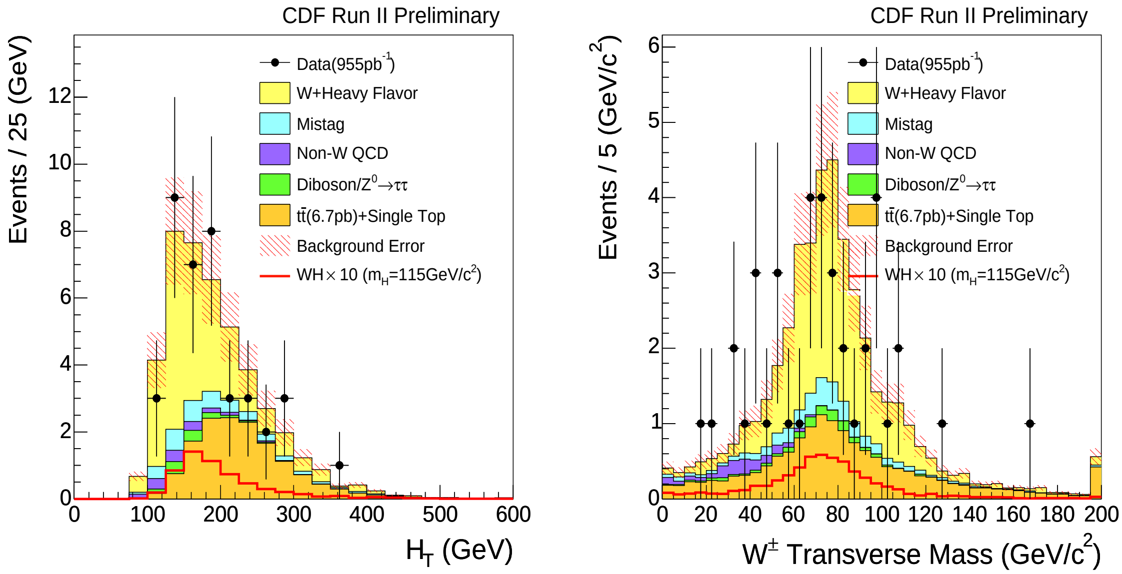

Figure 7.22 H_T(left) and M_T(right) distributions in at least two SECVTX b-tagged events.

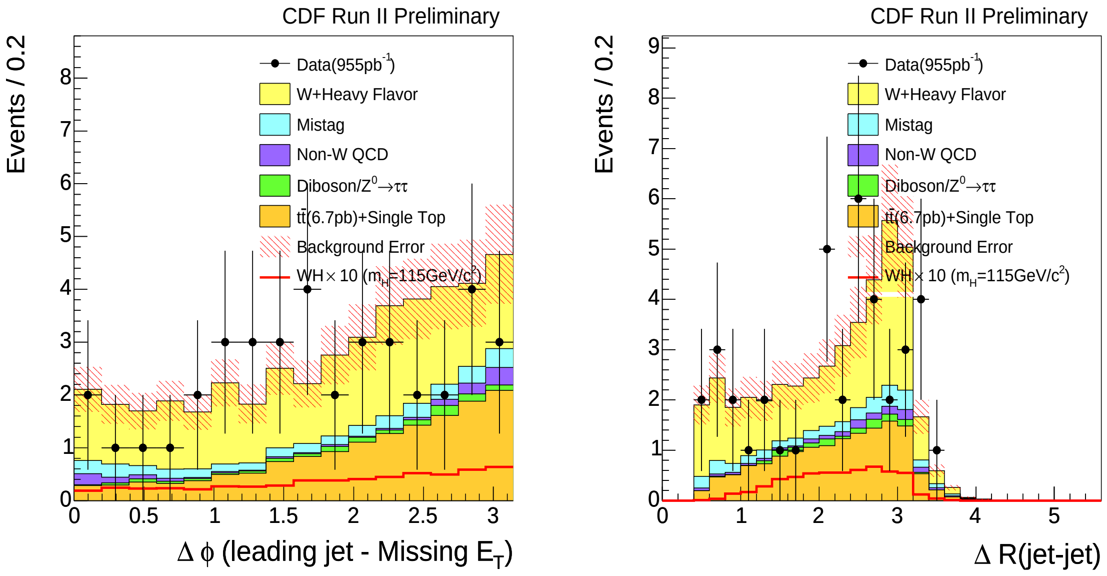

Figure 7.23 $\Delta\phi$(1st leading jet-MET)(left) and ΔR(jet1 − jet2)(right) distributions in at least two SECVTX b-tagged events.

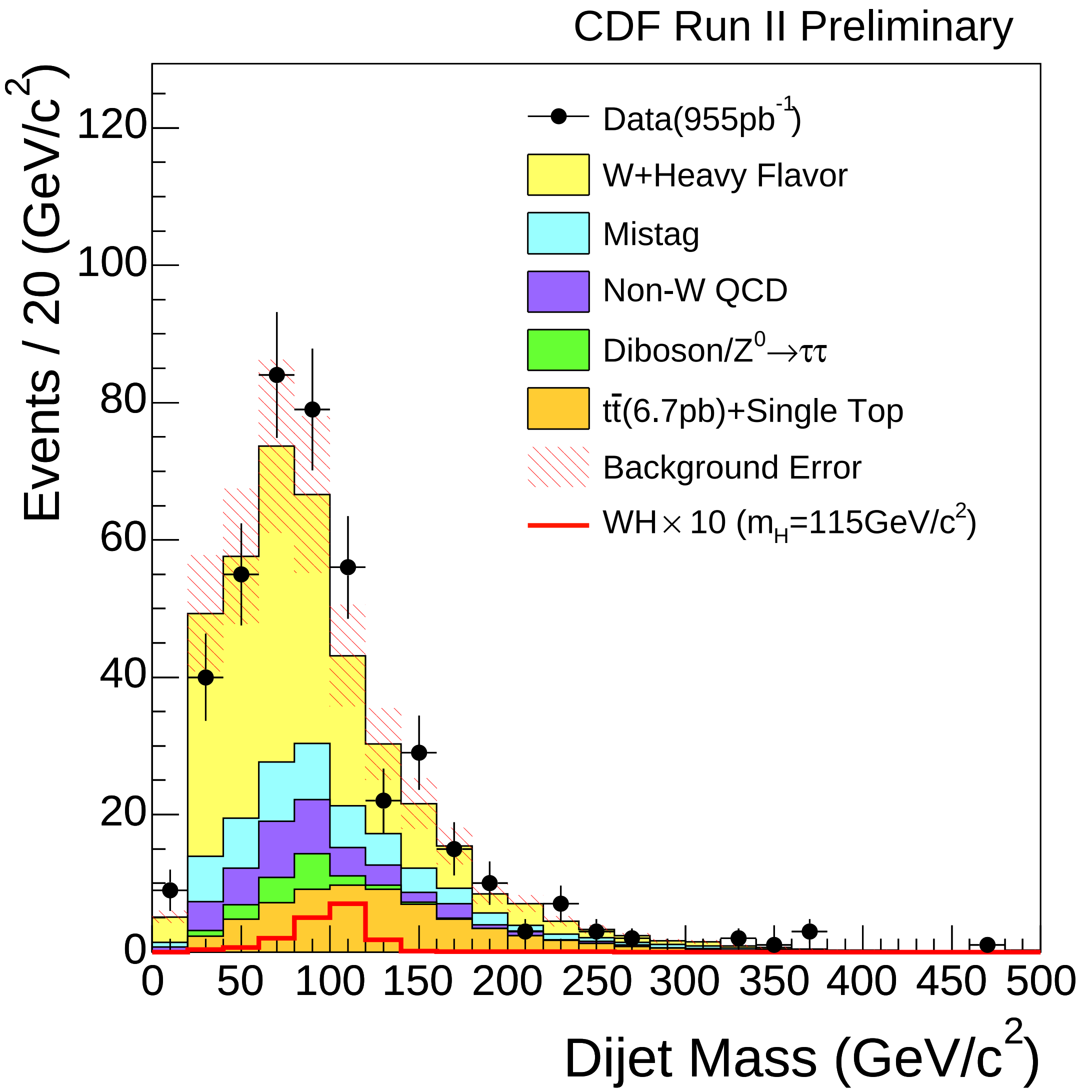

Figure 7.24 Dijet mass distribution in W+2jets events including exactly one SECVTX b-tagged jet that passes Neural Network b-tagging filter. Each contribution of the background sources are written in histogram, hatched box on the background histogram is background uncertainty, $WH \rightarrow \ell\nu b\bar{b}$ signal is scaled by a factor of 10 and drawn in solid(red) line and data is plotted with error bars.

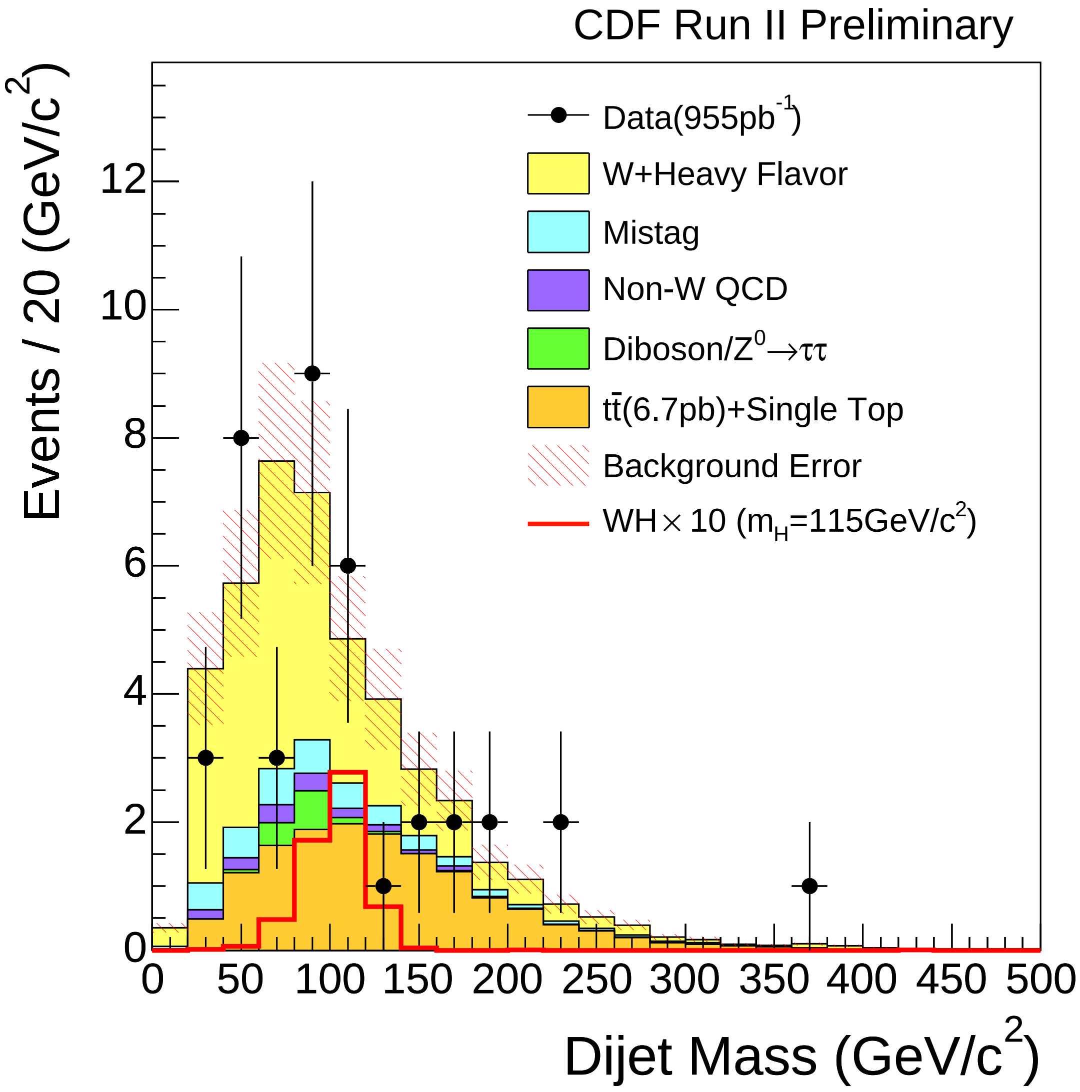

Figure 7.25 Dijet mass distribution in W+2jets events including at least two SECVTX b-tagged jets. Each contribution of the background sources are written in histogram, hatched box on the background histogram is background uncertainty, expected $WH \to \ell\nu b\bar{b}$ is scaled by a factor of 10 and drawn in solid(red) line and data is plotted with error bars.

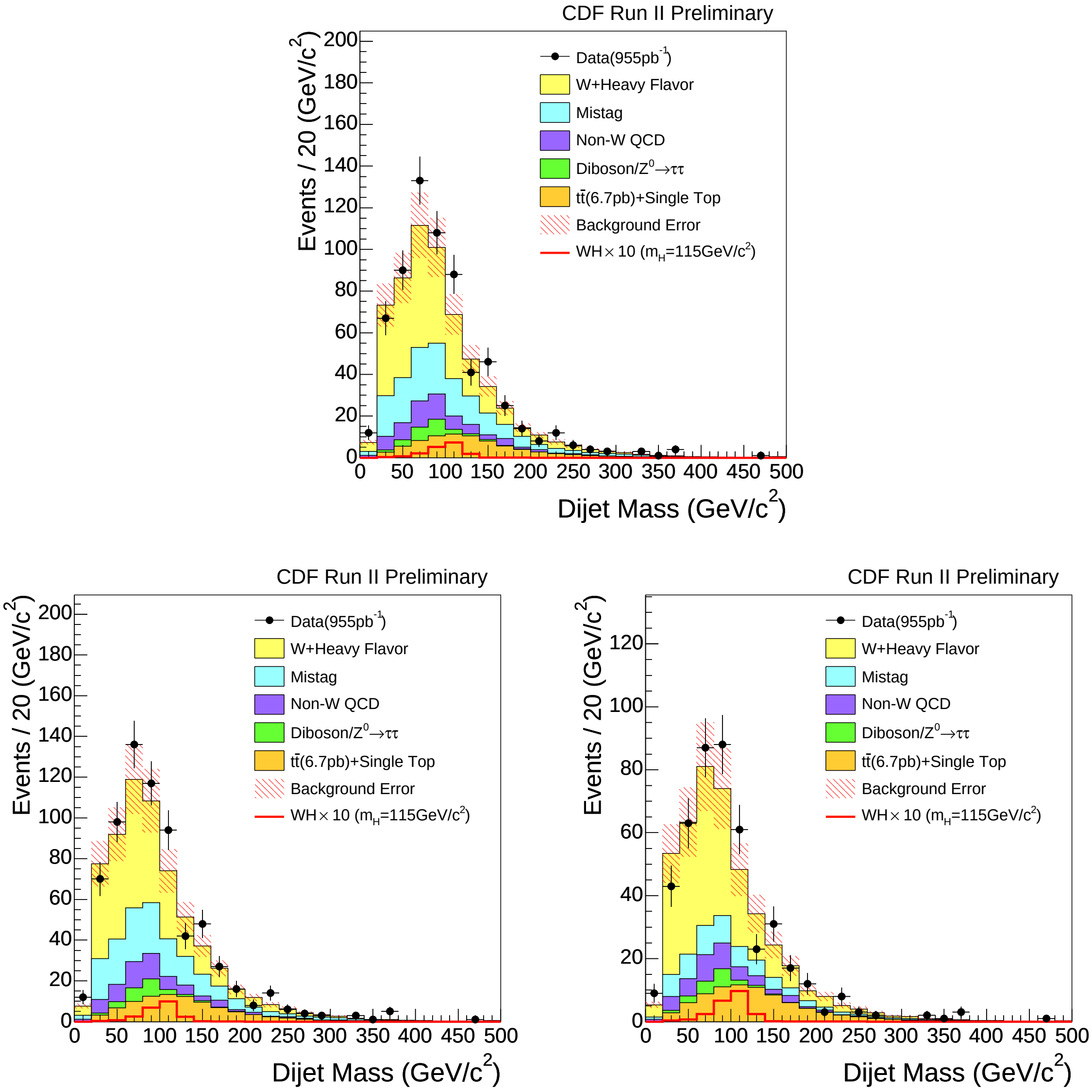

Figure 7.26 Dijet mass distributions in W+2jet events including exactly one SECVTX b-tagged jet(top), at least one SECVTX b-tagged jet without(bottom left) and with(right) applying Neural Network b-tagging. Each contribution of the background sources are written in histogram, hatched box on the background histogram is background uncertainty, expected $WH \to \ell\nu b\bar{b}$ is scaled by a factor of 10 and drawn in solid(red) line and data is plotted with error bars.

Chapter 8

Limit on Higgs Boson Production

No significant excess was found over the Standard Model background expectation as shown in the previous chapter. Accordingly we set an upper limit on the WH production cross section times branching ratio. Dijet mass distributions are fitted to extract an upper limit by using binned likelihood technique because dijet mass shape has most of Higgs boson specific signature. After setting an upper limit from $WH \to \ell\nu b\bar{b}$, the combination of the limits already obtained in CDF RUN II experiment is performed for the sake of setting stronger constraint on the Standard Model Higgs boson. Finally, the combination between CDF and DØ is also performed.

8.1 Binned Likelihood Technique

To find how consistent between two histograms, e.g. data and background, a method of fitting technique called "binned likelihood" is considered. This method takes care of uncertainties associated in each bin contents from the two histograms. The data counts in each bin is supposed to be fluctuating under the rule of Poisson statistics. Let Poisson probability be written as:

$$P_i(n_i, \mu_i) = \frac{\mu_i^{n_i} e^{-\mu_i}}{n_i!} \quad (i = 1, 2, \cdots, N_{\mathrm{bin}}), \tag{8.1}$$

where n_i, μ_i and N_{bin} stand for the number of observed data in i-th bin, the expectation in i-th bin and the total number of bins defined as: The purpose in this chapter is to set an constraint on the Standard Model Higgs boson production. Therefore, a null hypothesis is assumed by setting μ_i as:

$$\mu_i = s_i + b_i, \tag{8.2}$$

where s_i and b_i are the number of signal and expected background events in i-th bin respectively. s_i is a free variable to be extracted from data. s_i is written in another fashion:

$$s_i = \sigma(p\bar{p} \to W^{\pm}H) \cdot Br(H \to b\bar{b}) \cdot \epsilon_{WH \to \ell\nu b\bar{b}} \cdot \int \mathcal{L}dt \cdot f_i^{(WH \to \ell\nu b\bar{b})}, \tag{8.3}$$

where $f_i^{(WH \to \ell\nu b\bar{b})}$ is a signal fraction in i-th bin. $\epsilon_{WH \to \ell\nu b\bar{b}}$ and $\int \mathcal{L}dt$ are obtained in **Secs.7.1** and **5.2** respectively. Accordingly, $\sigma(p\bar{p} \to W^{\pm}H) \cdot Br(H \to b\bar{b})$ is the variable to be extracted from data, and the null hypothesis is interpreted as "the Standard Model Higgs boson exists with a certain value of $\sigma(p\bar{p} \to W^{\pm}H) \cdot Br(H \to b\bar{b})$ at specific confidence interval.". Then the alternative hypothesis is interpreted as "the Standard Model Higgs bosons production is not larger than a certain value of $\sigma(p\bar{p} \to W^{\pm}H) \cdot Br(H \to b\bar{b})$ at specific confidence level(C.L.)." With this logic, an upper limit on the Higss boson production cross section times branching ratio is sought. The extraction of the parameter of $\sigma(p\bar{p} \to W^{\pm}H) \cdot Br(H \to b\bar{b})$ is performed by using maximum likelihood method with a likelihood defined as:

$$L = \prod_{i=1}^{N_{\rm bin}} P_i(n_i, \mu_i) = \prod_{i=1}^{N_{\rm bin}} \frac{\mu_i^{n_i} e^{-\mu_i}}{n_i!}. \tag{8.4}$$

This likelihood is so called "binned likelihood" because it utilize the best of binning information. For background prediction b_i, here we categorized two kinds of background sources of QCD(mistag, $Wb\bar{b}, Wc\bar{c}, Wc$, non-W, Diboson), which is denoted by $N^{(QCD)}$, and TOP($t\bar{t}$, single top) written as $N^{(TOP)}$. Then, b_i becomes:

$$b_i = N^{(TOP)} f_i^{(TOP)} + N^{(QCD)} f_i^{(QCD)}, \tag{8.5}$$

where $f_i^{(TOP)}$ and $f_i^{(QCD)}$ are the background fractions of each background sources in i-th bin. Signal events and the expected background have systematic uncertainties, which must be taken into account correctly. Let the systematic uncertainties convoluted with the binned likelihood as:

$$\begin{aligned} L(\sigma \cdot Br) &= \int_{N_{QCD}} \int_{N_{TOP}} \int_{N_{WH}} \prod_{i=1}^{N_{\rm bin}} \frac{\mu_i^{n_i!} e^{-\mu_i}}{n_i} \\ &\times \; G(N_{QCD}, \sigma_{QCD}) G(N_{TOP}, \sigma_{TOP}) G(N_{WH}, \sigma_{WH}) dN_{QCD} dN_{TOP} dN_{WH}. \end{aligned} \tag{8.6}$$

The maximum of this likelihood distribution gives the most likely value of $\sigma \cdot Br$. An upper limit on it is obtained by one side examination. Let β be the cumulative probability of a variable α defined as:

$$\beta = \frac{\int_0^{\alpha_\beta} L(\alpha) d\alpha}{\int_0^{\infty} L(\alpha) d\alpha}, \tag{8.7}$$

where α_β is the upper limit of the variable α at confidence level of β. In this analysis, β is set at 0.95 and the upper limit on $\sigma(p\bar{p} \rightarrow WH) \cdot Br(H \rightarrow b\bar{b})$ at 95% C.L. is obtained.

8.2 Pseudo-Experiment and Limit Extraction

The method for a limit calculation is discussed in the previous section. Before looking at the upper limit obtained from data, pseudo-experiment, which is a method to make a mimic data, is performed to see the expectation of the limit. This gives an important milestone because data is always fluctuating by Poisson statistics. There is no way to know if the limit is reasonable or not from only a set of observed data. Pseudo-data is generated by fluctuating the background estimate with total uncertainties along Gaussian and each bin entry by Poisson distribution. Assuming such a pseudo data as a real data, limit is obtained by Eqs.8.6 and 8.7. In this analysis, 1000 pseudo-experiments are performed, and assigned their mean and root mean square as the expected limit and its deviation. The expected limits from various *b*-tagging strategies are shown in **Fig.8.1**. The upper limit obtained from the combined use of likelihoods of exactly one SECVTX *b*-tagged jet passing Neural Network *b*-tagging criteria and at least two SECVTX *b*-tagged jets criteria is computed as:

$$L(\sigma \cdot Br) = L(\sigma \cdot Br\ |1 \text{ Tag w/ NN Tag}) \times L(\sigma \cdot Br\ | \geq 2 \text{ Tag}), \tag{8.8}$$

where the correlations between "=1 Tag w/ NN Tag" and "$\geq$ 2 Tag" events are taken into account. The systematic uncertainty up to the pretag acceptance, luminosity uncertainty, and uncertainty of *b*-tagging scale factor are considered to be 100% correlated between the two selection types. In accordance with **Fig.8.1**, "=1 tag w/ NNtag" combined with "$\geq$2 Tag" gives the best expected limit as it is in the sensitivity study (see **Fig.7.2**).

Finally we set an upper limit on $\sigma(p\bar{p} \rightarrow WH) \cdot Br(H \rightarrow b\bar{b})$ with the combined likelihood of exactly one SECVTX *b*-tagged jet events and at least two SECVTX *b*-tagged events. (e.g. "=1 Tag w/ NN Tag && $\geq$ 2 Tag"). The likelihood distributions before and after the combination are shown in **Fig.8.2** for Higgs boson mass at 115 GeV/c^2. The observed limit as a function of Higgs boson mass is shown in **Fig.8.3** and **Table 8.1** together with the expected limit. The observed limit around 115 GeV/c^{2}is slightly higher than the expectation. To see if the obtained limit is reasonable or not, the results of pseudo experiments and the observed limit for each Higgs boson mass point are show in **Fig.8.4**.

For low mass region, we are somehow unlucky and obtained somehow worse upper limit than expected. But the result is still reasonable. This can be understood as a statistical fluctuation in dijet mass distributions (see **Fig.7.24**) around $m_H = 115$ GeV/c^2.

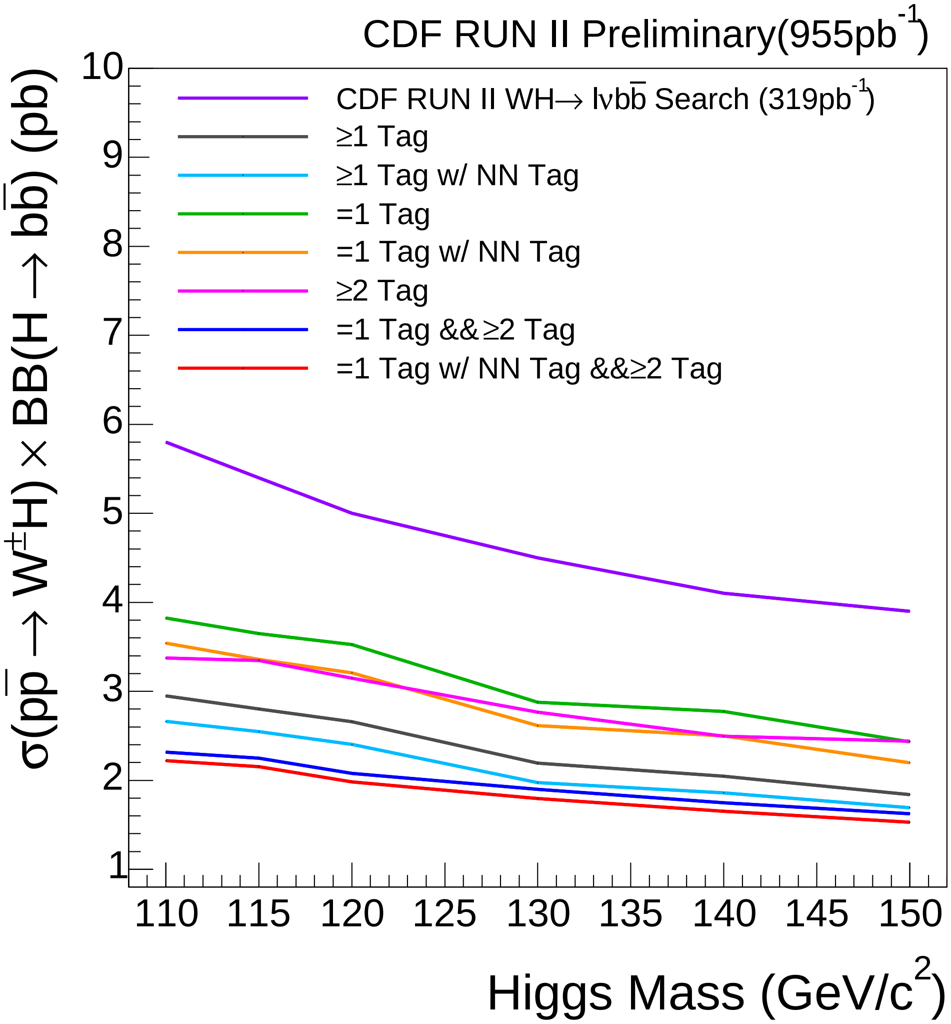

Figure 8.1 Expected upper limits on Higgs boson production cross section times branching ratio of $WH \rightarrow \ell\nu b\bar{b}$ process obtained from various b-tagging strategies. "Tag" and "NN Tag" mean SECVTX and Neural Network b-tagging respectively. The symbol of "&&" stands for the combined use of two b-tagging conditions. Purple line is the expected 95% C.L. upper limit obtained from at least one SECVTX b-tagged events in the previous analysis with 319 pb^{-1}.

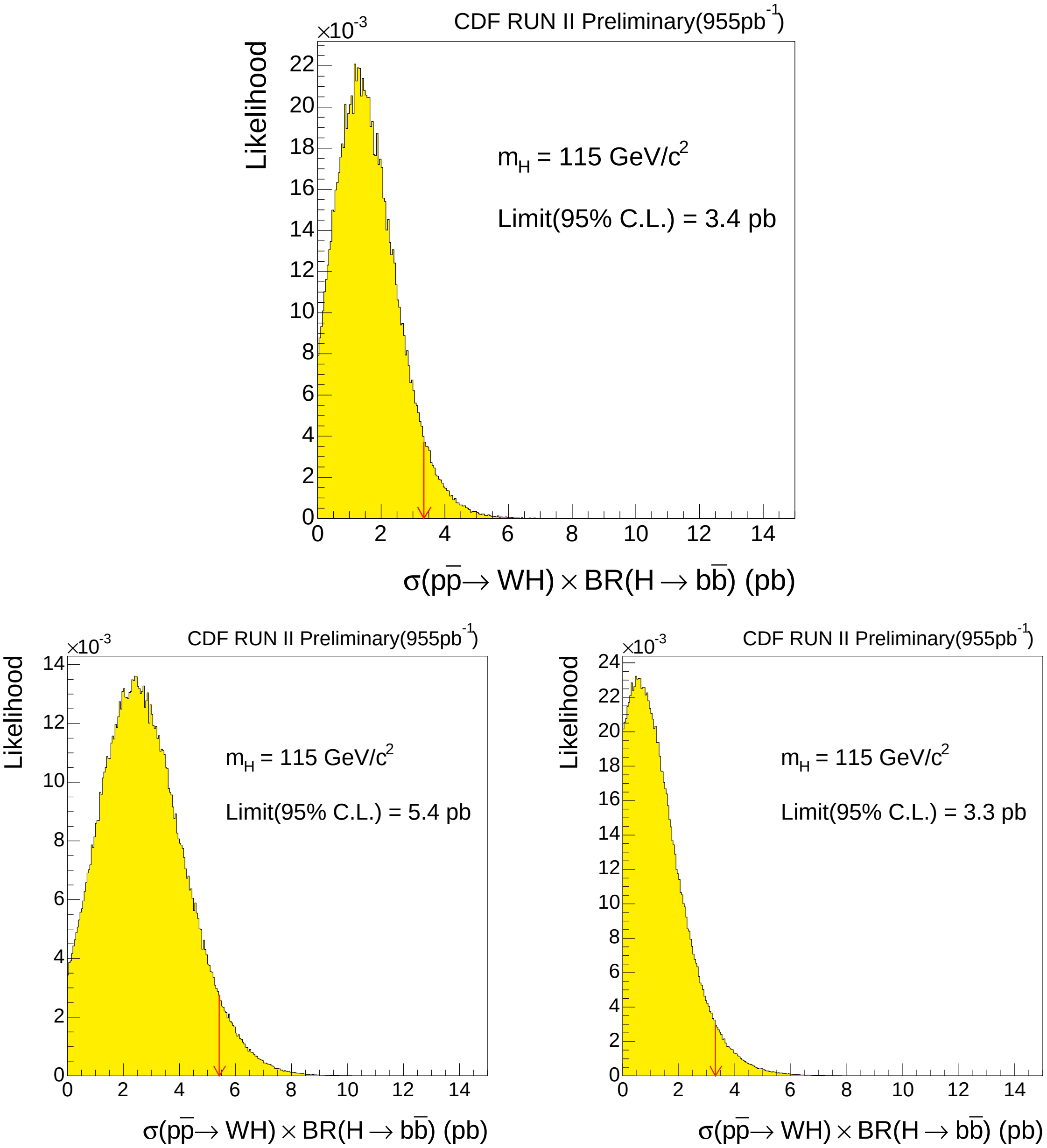

Figure 8.2 Likelihood distributions of events including exactly one SECVTX *b*-tagged jet passing Neural Network *b*-tagging(bottom left), at least two SECVTX *b*-tagged event(bottom right) and those combination(top). Red arrow shows the upper limit at 95% C.L.

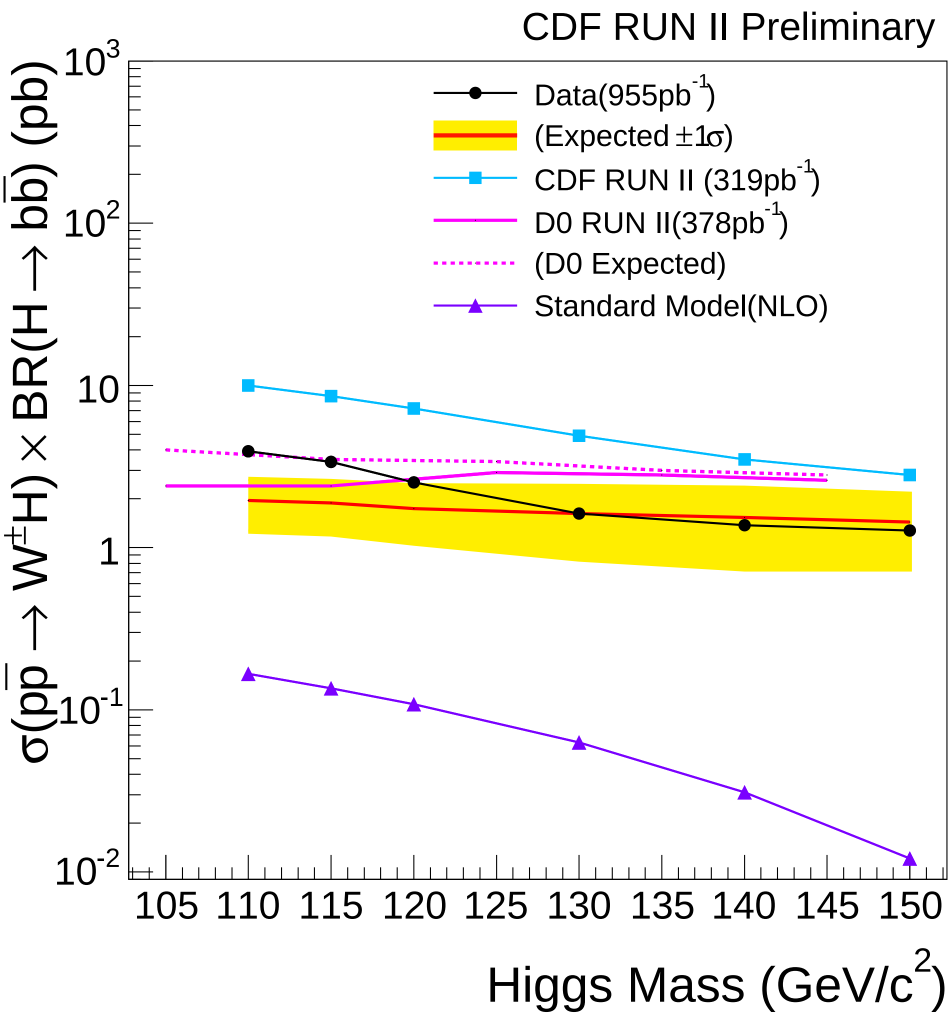

Figure 8.3 95% confidence level upper limit on $\sigma(p\bar{p} \to WH) \cdot Br(H \to b\bar{b})$ with an integrated luminosity of 955 pb^{-1} obtained from the combined likelihood between exactly one SECVTX b-tagged events passing Neural Network b-tagging and at least two SECVTX b-tagged events.

Higgs Mass GeV/c^2	Upper Limit(pb)	
	Observed	Expected
110	4.9	2.2±0.8
115	3.4	2.2±0.8
120	2.5	2.0±0.7
130	1.6	1.8±0.7
140	1.4	1.7±0.6
150	1.3	1.5±0.6

Table 8.1 Observed and expected upper limit on $\sigma(p\bar{p} \to WH) \cdot Br(H \to b\bar{b})$ at 95 % C.L.

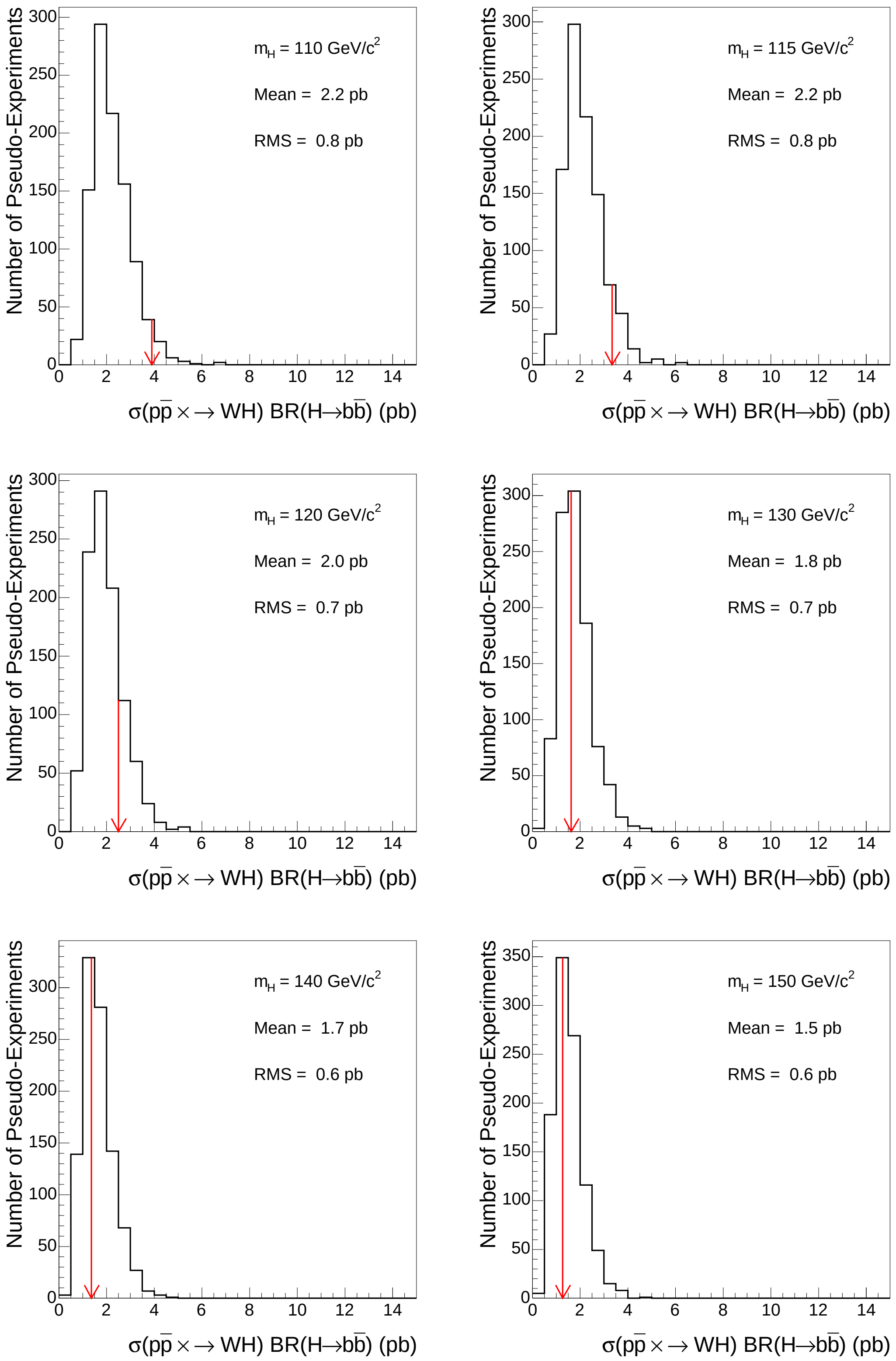

Figure 8.4 The result of pseudo-experiments obtained from the combined use of likelihood of exactly one SECVTX and Neural Network *b*-tagged events and at least two SECVTX *b*-tagged events. Red arrows are pointing the observed limits.

8.3 Combined Limit at CDF

CDF has made several searches for the Standard Model Higgs production using a data sample up to 1 fb^{-1} of integrated luminosity [82–86]. Since there is no single channel that is sensitive enough yet, it is necessary to combine the results of all the channels to maximize the search sensitivity. The most sensitive channels are $WH \to \ell\nu b\bar{b}$, $ZH \to \nu\bar{\nu}b\bar{b}$[82], $ZH \to \ell^+\ell^-\nu\bar{\nu}$[83] in the low Higgs boson mass range ($m_H < 135$ GeV/c^2), and $gg \to H \to W^+W^- \to \ell^+\ell^-\nu\bar{\nu}$[84] in high Higgs boson mass range ($m_H > 135$ GeV/c^2) are employed in the combination[1]. For low mass cases, $H \to b\bar{b}$ dominates the decay mode, thus dijet mass distribution is used for limit combination. However $H \to W^+W^-$ is dominant mode for high mass cases. In the process of $gg \to H \to W^+W^- \to \ell^+\ell^-\nu\bar{\nu}$, azimuthal angle of the two lepton system is employed.

The purpose of the present analysis is to develop a strategy on how to combine the results properly based on what we currently have. More importantly in the future, it would help us to sort out and define the common systematic between different analyses. We follow the procedure that was used in the RUN1 combination analysis of the Standard Model Higgs boson searches[87], which is based on a Bayesian framework that would make it possible to handle the systematic uncertainties properly on the large number of background and efficiency parameters involved in.

Cross sections and branching ratios are different from process to process, thereby the ratio of the upper limit on $(\sigma \cdot Br)$ at a certain Credible Level (C.L.)[2]. divided by that of the Standard Model prediction $(\sigma \cdot Br)_{SM}$ is considered to be a good variable to see where we are. Let R represent the ratio:

$$R_\beta = \frac{(\sigma \cdot Br)_\beta}{(\sigma \cdot Br)_{SM}}, \tag{8.9}$$

where β is the credible level. Let $\boldsymbol{n}$, $\boldsymbol{s}$ and $\boldsymbol{b}$ be introduced as:

$$\begin{aligned} \boldsymbol{n} &= \{n_{ij}\}, & (8.10)\\ \boldsymbol{s} &= \{s_{ij}\}, & (8.11)\\ \boldsymbol{b} &= \{b_{ij}\}, & (8.12)\\ (i &= 1, 2, \cdots, N_{\text{channel}}, \quad j = 1, 2, \cdots, N_{\mathrm{N_{bin}}}) & \end{aligned}$$

---

[1] CDF already has a result of $W^\pm H \to W^\pm W^+ W^-$ and $t\bar{t}H$ processes with 194 pb^{-1} and 320 pb^{-1} respectively. Those channels are not included in the combination in this analysis, because they are not expected to give large impact on the combination due to low sensitivity so far. Once those results are updated with more data, they should be included as well.

[2] In this thesis, use the term of "Credible Level (C.L.)" when Bayesian frame work is used

where n_{ij}, s_{ij}, b_{ij} and N_{channel} are the number of observed, expected signal, background events in i-th channel and j-th bin of the considered distribution respectively. The expected signal $\boldsymbol{s}$ is also written as:

$$s_{ij} = \int dt\mathcal{L} \cdot (\sigma_i \cdot Br_i)_{SM} \cdot \epsilon_i \cdot f_{ij}, \tag{8.13}$$

where ϵ_i and f_{ij} are the detection efficiency of i-th process and its binning fraction in j-th bin. The Bayesian posterior probability of $p(R|\boldsymbol{n})$, a probability density of R when data $\boldsymbol{n}$ is observed, is written as:

$$p(R|\boldsymbol{n}) = \frac{\int\int d\boldsymbol{s}d\boldsymbol{b}L(R,\boldsymbol{s},\boldsymbol{b}|\boldsymbol{n})\pi(R,\boldsymbol{s},\boldsymbol{b})}{\int\int\int dRd\boldsymbol{s}d\boldsymbol{b}L(R,\boldsymbol{s},\boldsymbol{b}|\boldsymbol{n})\pi(R,\boldsymbol{s},\boldsymbol{b})}, \tag{8.14}$$

where L and π are likelihood and prior probability. The likelihood is based on the binned Poisson density as shown in Eq.8.1. For a combination between different processes, a likelihood product over channels is considered as:

$$L(R,\boldsymbol{s},\boldsymbol{b}|\boldsymbol{n}) = \prod_{i=1}^{N_{\mathrm{channel}}} \prod_{j=1}^{N_{\mathrm{bin}}} \mu_{ij}^{n_{ij}} \frac{e^{-\mu_{ij}}}{n_{ij}!}, \tag{8.15}$$

where $\mu_{ij} = R \cdot s_{ij} + b_{ij}$. The variable in the prior density can be separated because signal, background estimate, and observed data are possible to be treated independently:

$$\pi(R,\boldsymbol{s},\boldsymbol{b}) = \pi(R)\pi(\boldsymbol{s})\pi(\boldsymbol{b}). \tag{8.16}$$

Since the numerator of R, e.g. $(\sigma \cdot Br)_\beta$, is a variable to be observed from data and nothing is know about it a priori. However, the denominator is obtained by the Standard Model. Regarding those facts, a flat prior density to the total number of Higgs events, e.g. $(R \cdot s_{\mathrm{total}})$ where $s_{\mathrm{total}} = \sum_i \sum_j s_{ij}$, is assigned instead of $(\sigma \cdot R)_\beta$[3]. Then Eq.8.16 can be transformed as:

$$\pi(R)\pi(\boldsymbol{s})\pi(\boldsymbol{b}) = s_{\mathrm{total}}\theta(Rs_{\mathrm{total}})\pi(\boldsymbol{s})\pi(\boldsymbol{b}), \tag{8.17}$$

where θ is a flat probability. Gaussian is a proper probability density function prior densities of $\pi(\boldsymbol{s})$ and $\pi(\boldsymbol{b})$:

$$\begin{aligned} \pi(s_{ij}) &= G(s_{ij}|\bar{s}_{ij}, \sigma_{s_{ij}}), && (8.18) \\ \pi(b_{ij}) &= G(b_{ij}|\bar{b}_{ij}, \sigma_{b_{ij}}) && (8.19) \end{aligned}$$

where $\bar{s}_{ij}(\bar{b}_{ij})$ and $\sigma_{s_{ij}}(\sigma_{b_{ij}})$ are the expected number of events and its total systematic

---

[3] This is an arbitrary choice in Bayesian framework.

m_H	σ_{WH}	σ_{ZH}	σ_{WW}	$Br(H \to bb)$	$Br(H \to W^+W^-)$
(GeV/c^2)	(fb)			(%)	
110	207.70	123.33	1281	77.02	4.41
120	152.89	92.70	1006	67.89	13.20
130	114.51	70.38	801	52.71	28.69
140	86.00	54.20	646	34.36	48.33
150	66.14	41.98	525	17.57	68.17
160	51.03	32.89	431	4.00	90.11
170	38.89	26.12	357	0.846	96.53
180	31.12	20.64	297	0.541	93.45
190	24.27	16.64	249	0.342	77.61
200	19.34	13.46	211	0.260	73.47

Table 8.2 The NNLO Higgs boson production cross sections and the decay branching ratios as a function of Higgs boson mass.

uncertainties of signal(background) and $G(x|\bar{x}, \sigma_x)$ stands for Gaussian with mean and standard deviation of $\bar{x}$ and σ_x. Taking those discussion into account, the final form of the posterior probability takes the form of:

$$p(R|\boldsymbol{n}) = \frac{\int\int d\boldsymbol{s}d\boldsymbol{b}L(R, \boldsymbol{s}, \boldsymbol{b}|\boldsymbol{n})G(\boldsymbol{s}|\bar{\boldsymbol{s}}, \boldsymbol{\sigma}_s)G(\boldsymbol{b}|\bar{\boldsymbol{b}}, \boldsymbol{\sigma}_b)s_{\text{total}}}{\int\int\int dRd\boldsymbol{s}d\boldsymbol{b}L(R, \boldsymbol{s}, \boldsymbol{b}|\boldsymbol{n})G(\boldsymbol{s}|\bar{\boldsymbol{s}}, \boldsymbol{\sigma}_s)G(\boldsymbol{b}|\bar{\boldsymbol{b}}, \boldsymbol{\sigma}_b)s_{\text{total}}}. \tag{8.20}$$

The Standard Model Higgs boson production cross sections at the TEVATRON and the decay branching ratios are obtained from the TeV4LHC Higgs working group[88] and HDECAY[14] to the precision of Next to Next to Leading Order (NNLO), which are summarized in **Table 8.2** as functions of Higgs boson mass. The residual theoretical uncertainties for WH and ZH production cross section are rather small, less than 5%. Also there is about 10% for gluon fusion $gg \to H$ process.

Systematic uncertainties in the various analyzes come from Monte Carlo modeling of the geometrical and kinetic acceptance, b-tagging efficiency scale factor, lepton identification, the effect due to the jet energy scale, background uncertainties, and the uncertainty on the luminosity. We divide these systematics into several groups.

- Signal acceptance: luminosity, b-tag efficiency scale factor, lepton identification, the jet energy scale, MC modeling (ISR/FSR+PDF), and the rest of the uncertainties.

- Background normalization: heavy flavor fraction, mistags, top contributions, non-W, diboson and the rest of the backgrounds.

- Background shape uncertainty.

Channels	$\ell\nu b\bar{b}$		$\nu\bar{\nu}b\bar{b}$		$\ell\ell b\bar{b}$	W^+W^-
	single	double	single	double		
Acceptance						
Luminosity (%)	6.0	6.0	6.0	6.0	6.0	6.0
b-tag SF (%)	5.3	16.0	8.0	16.0	8.0	0.0
Lepton ID (%)	2.0	2.0	2.0	2.0	1.4	3.0
JES (%)	3.0	3.0	6.0	(1-20)	(1.6-20)	1.0
MC modeling (%)	4.0	10.0	4.0	5.0	2.0	5.0
Trigger (%)	0.0	0.0	3.0	3.0	0.0	0.0
Shape (%)	0.0	0.0	0.0	0.0	-20.0	0.0
Background						
Mistag (%)	22	15	17	17	17	0
QCD (%)	17	20	-10	-44	-50	0
W/Z+Heavy Flavor(I) (%)	33	34	12	12	40	0
W+Heavy Flavor(II)(%)	0	0	-10	-42	0	0
Z+Heavy Flavor(II)(%)	0	0	-6	-19	0	0
Top(I) (%)	13.5	20	12	12	15	0
Top(II)(%)	0	0	-2	-3	0	0
Diboson(I) (%)	16	25	12	12	20	11
Diboson(II)(%)	0	0	-5	-10	0	0
Other (%)	0	0	0	0	0	-(12-18)

Table 8.3 The breakdown of systematic uncertainties for each individual channel where the positive values mean correlated between the channels while the negative ones are uncorrelated with the rest of channels.

For each group, we assign each measurement to be 100% correlated or uncorrelated with other measurements. The breakdown of systematics for each channel are summarized in **Table 8.3** where a positive value indicates 100% correlated systematic among the channels and a negative value indicates the systematic uncorrelated. The priors used are truncated Gaussian densities constraining a given parameter to its expected value with its uncertainty.

The corresponding 95% credibility upper limit R_{95} is obtained by:

$$\int_0^{R_{95}} p(R|\boldsymbol{n})dR = 0.95. \tag{8.21}$$

Fig.8.5 summarizes the limits from each individual channel and all the channels combined as a function of Higgs masses, and the results are also shown in **Table 8.4**.

To check the sensitivity of the combination of different channels, we calculate the mean upper limits one would obtain from a large ensemble of pseudo-experiments. In the absence of Higgs signal, the pseudo-experiment is generated by fluctuating the expected backgrounds with their uncertainties as performed in **Sec.8.2**. **Fig.8.6** shows the upper limits obtained from the pseudo-experiments at various Higgs boson mass and the observed limits, which are consistent with the expectation obtained from pseudo-experiments.

8.4 Combined Limit at the TEVATRON

As the method of the limit combination between different channels is discussed and applied to the results obtained in CDF in previous section, it is also possible to combine the results from DØ. The processes used for combinations are summarized in **Table 8.5**. The distributions used in the limit combination are dijet mass for low mass Higgs boson ($m_H < 135$ GeV/c^2) and azimuthal angle of two lepton system for high mass Higgs boson ($m_H > 135$ GeV/c^2). From CDF, the four channels used in previous section are employed. DØ provides $WH \rightarrow \not\ell \nu b\bar{b}$[4] and $W^{\pm}H \rightarrow W^{\pm}W^{+}W^{-} \rightarrow \ell_1^{\pm}\nu\ell_2^{\pm}\nu + X$ in addition to the same channels used in CDF. This process requires two like signed leptons, e.g. $\ell_1^{\pm}\ell_2\pm = e^{\pm}e^{\pm}, e \pm \mu^{\pm}, \mu^{\pm}\mu^{\pm}$, in the final state. Limits from individual processes and the final combined limit are shown in **Fig.8.7** and **Table 8.6**. For low mass Higgs boson range, $ZH \rightarrow \nu\bar{\nu}b\bar{b}, \ell^{+}\ell^{-}b\bar{b}$ and $WH \rightarrow \ell\nu b\bar{b}$ provides the dominant contribution to the combined limit as expected. Also $gg \rightarrow H \rightarrow W^{+}W^{-} \rightarrow \ell^{-}\bar{\nu}\ell^{+}\nu$ process shows the decisive contribution in high mass Higgs boson range. Finally the ratio of $(\sigma \cdot Br)_{95}/(\sigma \cdot Br)_{SM}$ becomes a factor of $4 \sim 10$ for Higgs boson mass $m_H = 100 \sim 200$ GeV/c^2. The result at present could not give a constraint on the Higss boson mass, but the ratio is getting close to the Standard Model. Some of the processes are not using full data set of 1fb^{-1} data yet, and they would be updated to the full data set of 1 fb^{-1}. Then the result would be improved further in near future.

---

[4] $\not\ell$ means that the lepton ℓ is not detected. This process has the same experimental final state of $\nu\bar{\nu}b\bar{b}$

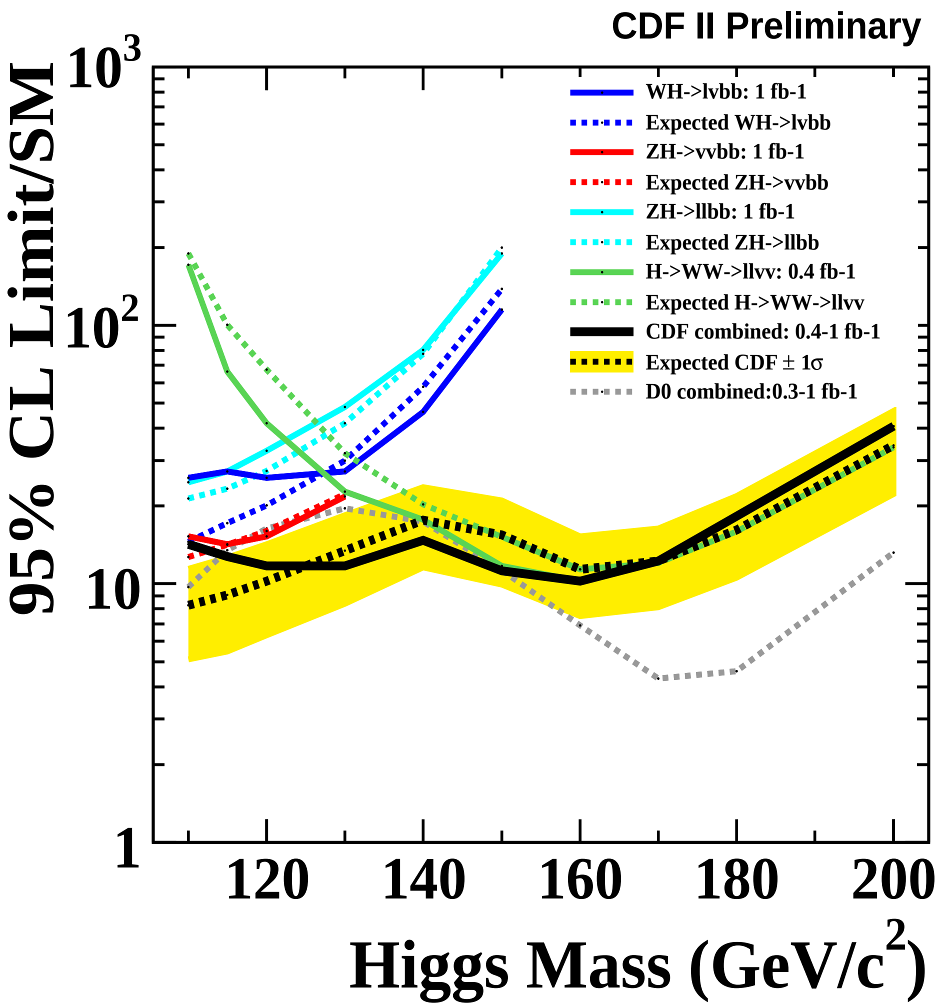

Figure 8.5 The combined upper limit as a function of Higgs mass between 110 and 200 GeV/c^2 as well as the individual limits from individual channels at CDF.

Mass (GeV/c^2)	Combined Ratio Limit (R_{95})	Expected Limits (pb)	
		Mean	RMS
110	14.2	8.3	3.2
115	12.8	9.0	3.6
120	11.8	10.2	4.0
130	11.8	13.4	5.0
140	14.8	17.7	6.1
150	11.2	15.3	5.3
160	10.2	11.4	3.9
170	12.2	12.3	4.2
180	18.2	16.2	5.7
200	40.8	34.4	12.2

Table 8.4 The summary of observed, expected ratio limits (R_{95}) for various Higgs mass at CDF.

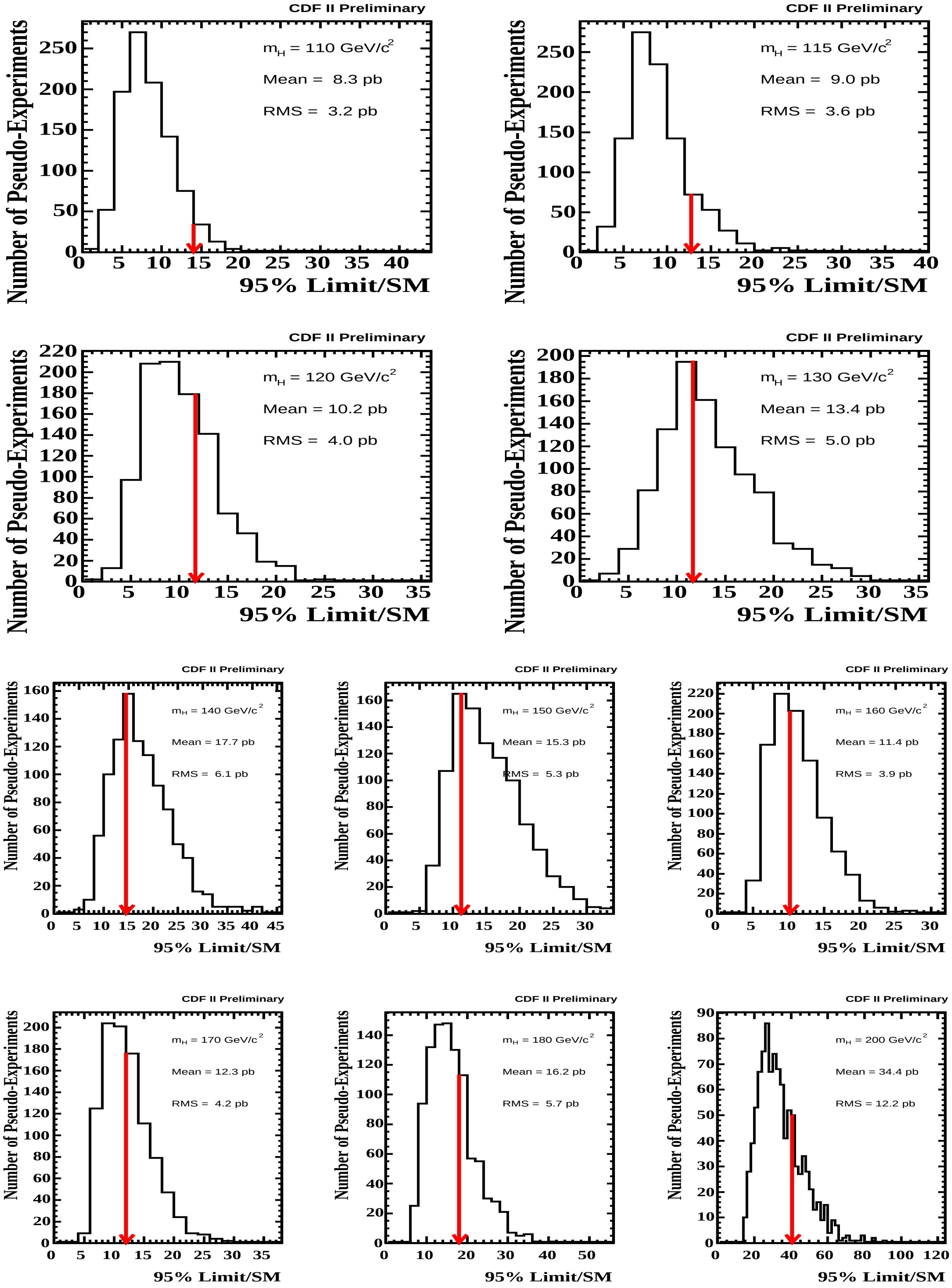

Figure 8.6 The distributions of upper limits from the pseudo-experiments for Higgs mass between 110 and 200 GeV/c^2 where the arrows indicate the observed 95% C.L. upper limit from data.

Process	Luminosity(pb^{-1})	Distribution	Reference
CDF			
$WH \rightarrow \ell\nu b\bar{b}$ (single/double tag)	1000	dijet mass	-
$ZH \rightarrow \nu\bar{\nu}b\bar{b}$ (single/double tag)	1000	dijet mass	[82]
$ZH \rightarrow \ell^+\ell^- b\bar{b}$ (at least one tag)	1000	dijet mass	[83]
$H \rightarrow W^+W^- \rightarrow \ell^+\nu\ell^-\bar{\nu}$	360	$\Delta\phi(\ell_1, \ell_2)$	[84]
DØ			
$WH \rightarrow e\nu b\bar{b}$ (single/double tag)	371	dijet mass	[18]
$WH \rightarrow \mu\nu b\bar{b}$ (single/double tag)	385	dijet mass	[18]
$WH \rightarrow \not\ell\nu b\bar{b} + X$ (single/double tag)	260	dijet mass	[89]
$ZH \rightarrow \nu\bar{\nu}b\bar{b}$ (single/double tag)	260	dijet mass	[89]
$ZH \rightarrow \ell^+\ell^- b\bar{b}$ (double tag)	320-389	dijet mass	[90]
$W^{\pm}H \rightarrow W^{\pm}W^+W^- \rightarrow \ell_1^{\pm}\nu\ell_2^{\pm}\nu$	363-384	$\Delta\phi(\ell_1, \ell_2)$	[91]
$H \rightarrow W^+W^- \rightarrow \ell^+\nu\ell^-\bar{\nu}$	930-950	$\Delta\phi(\ell_1, \ell_2)$	[92, 93]

Table 8.5 Processes to be combined in Higgs boson search at the TEVATRON.

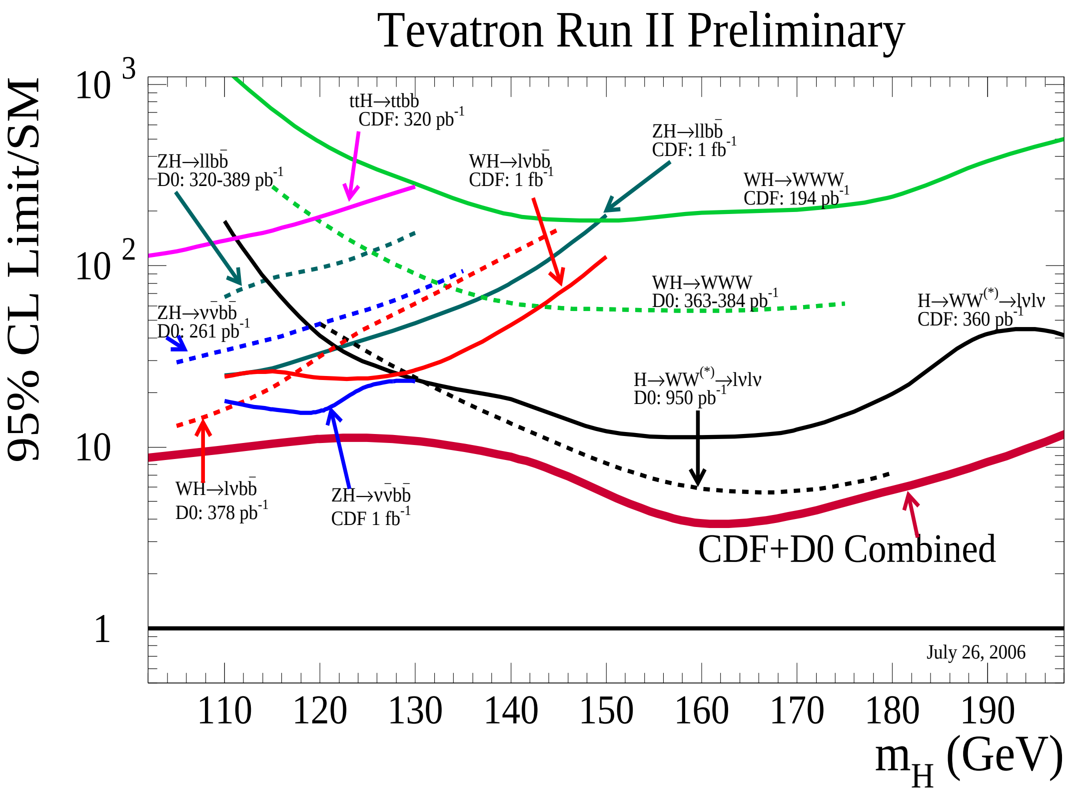

Figure 8.7 Summary of the Standard Model Higgs boson searches at the TEVATRON.

m_H (GeV/c^2)	100	115	120	140	160	180	200
Expected limit	6.2	7.6	8.7	9.3	5.0	7.5	15.5
Observed limit	8.5	10.4	11.1	8.8	3.8	6.1	12.3

Table 8.6 Observed and expected limit as a function of Higgs boson mass at the TEVATRON.

Chapter 9

Conclusions

We performed a search for Standard Model Higgs boson production in one of the most sensitive processes, $WH \rightarrow \ell\nu b\bar{b}$, using 1 fb $^{-1}$ at the TEVATRON. To improve the sensitivity of the search, we applied Neural Network b-tagging in addition to SECVTX b-tagging. The background modelings and its estimates are validated by the measurements of $t\bar{t}$ production cross section in $W+3$ or more jets events, and comparisons of a bunch of kinetic distributions. Neural Network b-tagging improved the sensitivity about 10% compared to the sensitivity before applying it. As a result, the combined use of exactly one SECVTX b-tagged events and at least two SECVTX b-tagged events showed the best sensitivity. Both of the number and kinetic distributions of data and Standard Model background prediction are consistent each other, thereby we set an upper limit on the Higgs boson production cross section times branching ratio as

$$\sigma(p\bar{p} \rightarrow WH) \times Br(H \rightarrow b\bar{b}) < 3.9 \sim 1.3(\text{pb}),$$

as a function of Higgs boson mass from 110 to 150 GeV/c^2 at 95% C.L..

Since there is no single channel that is sensitive enough for the Standard Model Higgs boson search yet, we have developed a Bayesian technique for the limit combination and applied it for the processes of $WH \rightarrow \ell\nu b\bar{b}$, $ZH \rightarrow \nu\bar{\nu}b\bar{b}$, $ZH \rightarrow \ell^+\ell^- b\bar{b}$ and $gg \rightarrow H \rightarrow W^+W^- \rightarrow \ell^+\nu\ell^-\bar{\nu}$. Combined upper limit at 95% C.L. on the ratio of Higgs production cross section times branching ratio to its Standard Model prediction is obtained as:

$$\frac{(\sigma \times Br)_{95}}{(\sigma \times Br)_{SM}} < 10.2 \sim 40.8,$$

for Higgs boson mass between 110 and 200 GeV/c^2. This limit combination in CDF

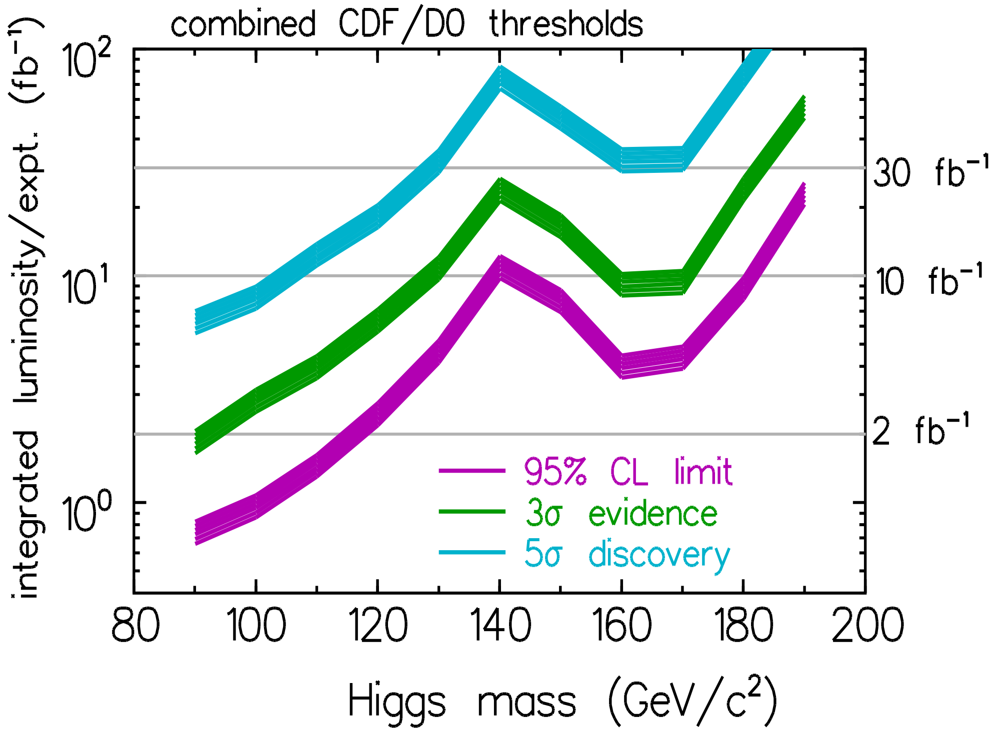

Figure 9.1 Prospects of sensitivity and integrated luminosity for the Standard Model Higgs boson search as functions of Higgs boson mass at the TEVATRON.

RUN2 experiment is the first attempt and provided a milestone for the final result of the experiment. Finally, Higgs boson searches at DØ are also combined, and the result is

$$\frac{(\sigma \times Br)_{95}}{(\sigma \times Br)_{SM}} < 3.8 \sim 12.3,$$

for Higgs boson mass between 110 and 200 GeV/c^2. The combined limit could not provide a constraint on the Higgs boson mass, but the limit is getting closer and closer to the Standard Model prediction. Some of the processes are not analyzed with the full data set of 1 fb^{-1} yet. Thereby, once these searches are updated in near future, the result would be improved.

The TEVATRON is planned to run at the end of 2009, and the total integrated luminosity in the final round of RUN2 experiment is expected to be from 4(pessimistic) to 8(optimistic) fb^{-1}. Taking the CDF and DØ combined sensitivity shown in **Fig.9.1** into account, there is possibility for 3σ evidence around at Higgs boson mass of 115 GeV/c^2. However, it is also important to to look for techniques that provide additional improvement in sensitivity aside from waiting for new data.

Bibliography

[1] S. Glashow, Nucl. Phys. **22**, 579 (1961).

[2] S. Weinberg, Phys. Rev. Lett. **19**, 1264 (1967).

[3] A. Salam, Proc. of the 8th Nobel Symposium on 'Elementary particle theory, relativistic groups and analyticity', Stockholm, Sweden, p.367-377 (1969).

[4] P. W. Higgs, Phys. Rev. Lett. **13**, 508 (1964).

[5] F. Abe *et al.*, Phys. Rev. Lett. **74**, 2626 (1995).

[6] ALEPH and DELPHI and L3 and OPAL Collaboration and the LEP Working Group for Higgs Boson Searches, Phys. Lett. **B 565**, 61 (2003).

[7] LEP Electroweak Working Group, `http://lepewwg.web.cern.ch/LEPEWWG/`.

[8] A. Abulencia *et al.*, Phys. Rev. Lett. **96**, 081903 (2006).

[9] Y. Ishizawa, Ph.D. dissertation, University of Tsukuba, Japan (2005).

[10] J.J. Thomson, Phil. Mag. 44 (1897) 293; Nature 55 (1897) 453.

[11] M. E. Peskin and D. V. Schroeder, *An Introduction to Quantum Field Theory*, Westview press, (1995).

[12] F. Halzen and A. D. Martin, *QUARKS & LEPTONS -An Introductory Course in Modern Particle Physics-*, John Wiley & Sons Inc., (1984).

[13] J. Conway, `http://www.physics.ucdavis.edu/∼conway/research/higgs/higgs.html`.

[14] A. Djouadi, J. Kalinowski, and M. Spira, Comp. Phys. Commun. **108**, 56 (1998).

[15] J. Erler, arXiv:hep-ph/0005084 (2000).

[16] LEP Electroweak Working Group, arXiv:hep-ex/0511027 (2005).

[17] J. de Troconiz and F. Yndurain, Phys. Rev. **D 71**, 073008 (2005).

[18] The DØ Collaboration, DØ-5054 (2006).

[19] F. Abe *et al.*, Nucl. Instrum. Meth. **A271**, 357 (1988).

[20] The CDF Collaboration, FERMILAB-Pub-96/390-E (1996).

[21] T. Affolder *et al.*, Nucl. Instrum. Meth. **A526**, 249 (2004).

[22] C. S. Hill, Nucl. Instrum. Meth. **A530**, 1 (2004).

[23] A. Sill, Nucl. Instrum. Meth. **A447**, 1 (2000).

[24] A. Affolder *et al.*, Nucl. Instrum. Meth. **A453**, 84 (2000).

[25] L. Balka and others., Nucl. Instrum. Meth. **A267**, 272 (1988).

[26] S. Bertolucci *et al.*, Nucl. Instrum. Meth. **A267**, 301 (1988).

[27] A. Artikov *et al.*, Part. Nucl. Lett. **114**, 25 (2002).

[28] A. Artikov, J. Budagov, and G. Bellettini, Nucl. Instrum. Meth. **A538**, 358 (2005).

[29] Trigger and Data set Working Group, `http://www-cdf.fnal.gov/internal/upgrades/daq_trig/twg/tools/trigopts.ps`.

[30] K. Anikeev *et al.*, CDF-5051 (1999).

[31] K. Maeshima *et al.*, `http://www-cdfonline.fnal.gov/internal/mon/consumer/home/consumer_home.html`.

[32] H. Wenzel *et al.*, `http://www-cdfonline.fnal.gov/internal/mon/consumer/framework/index.html`.

[33] B. Kilminster *et al.*, CDF-4794 (1998).

[34] B. Kilminster *et al.*, CDF-5292 (2000).

[35] J. Han *et al.*, `http://www-cdfonline.fnal.gov/internal/mon/consumer/ymon/YMon_Home.html`.

[36] C. Plager *et al.*, `http://www-cdfonline.fnal.gov/internal/mon/cdfdaq/XMon/xmon.html`.

[37] M. Worcester *et al.*,
`http://www-cdfonline.fnal.gov/internal/mon/consumer/trigmon/trigmon.html`.

[38] S. M. Wang *et al.*,
`http://www.phys.ufl.edu/ ming/WWW/cdf/lummon/lummon.html`.

[39] H. Stadie *et al.*,
`https://www-cdfonline.fnal.gov/internal/mon/consumer/BeamMon`.

[40] H. Bachacou *et al.*,
`http://fcdfhome.fnal.gov/usr/bachacou/SVXMon/svxmon.html`.

[41] G. Manca *et al.*,
`http://www-cdfonline.fnal.gov/internal/mon/consumer/silimon/new/Intro.html`.

[42] V. Khotilovich *et al.*,
`http://www-cdfonline.fnal.gov/internal/mon/consumer/objectmon/objectmon.html`.

[43] J. Paul *et al.*,
`http://www-cdf.fnal.gov/internal/people/links/KevinA.Burkett/COT/stage0.html`.

[44] W. Badgett *et al.*,
`http://www-cdfonline.fnal.gov/internal/mon/consumer/daqmon`.

[45] W. Badgett,
`http://www-cdfonline.fnal.gov/daq/hardware/daqerrmon.html`.

[46] M. Rescigno *et al.*,
`http://www-cdfonline.fnal.gov/internal/ops/svt/spymon/consumer.html`.

[47] S. Levy *et al.*,
`http://hep.uchicago.edu/cdf/physmon/physmon.html`.

[48] D. Acosta *et al.*, Phys. Rev. **D 72**, 032002 (2005).

[49] L. Cerrito and A. Taffard, CDF-6305 (2003).

[50] A. Abulencia *et al.*, arXiv:hep-ex/0607035, submitted to Phys. Rev. **D** (2006).

[51] D. Acosta *et al.*, CDF-6315 (2003).

[52] C. Neu *et al.*, CDF-7578 (2005).

[53] StatSoft, Inc., Neural Networks
`http://www.statsoft.com/textbook/stneunet.html` (1984-2003).

[54] C. Peterson, T. Rögnavaldsson, and L. Lönnbald, Comp. Phys. Commun. **81**, p.185-220 (1994).

[55] R. Brun and F. Rademakers, `http://root.cern.ch` (since 1995).

[56] M. Cavalli *et al.*, `http://www-cdf.fnal.gov/internal/dqm/dqm.html`.

[57] H. Bachacou, J. Nielsen, and W. Yao, CDF-6569 v1.0 (2004).

[58] H. Bachacou, J. Nielsen, and W. Yao, CDF-6569 v2.0 (2004).

[59] J. Guimaraes and C. S. Rappoccio, CDF-7326 (2006).

[60] D. Sherman, S. Rappoccio, and J. G. da Costa, CDF-7585 (2005).

[61] S. Budd, T. Junk, and C. Neu, CDF-8072 (2006).

[62] H. Bachacou *et al.*, CDF-7742 (2005).

[63] H. Bachacou *et al.*, CDF-7007 (2004).

[64] M. L. Mangano *et al.*, arXiv:hep-ph/0206293 (2003).

[65] G. Corcella *et al.*, arXiv:hep-ph/0201201 (2002).

[66] J. M. Campbell and R. K. Ellis, Phys. Rev. **D 65**, 113007 (2002).

[67] D. Acosta *et al.*, Phys. Rev. Lett. **94**, 091803 (2005).

[68] M. Cacciari *et al.*, arXiv:hep-ph/0303085 (2005).

[69] B. W. H. Laenen *et al.*, Phys. Rev. **D 66**, 054024 (2002).

[70] A. Abulencia *et al.*, Phys. Rev. Lett. **97**, 082004 (2006).

[71] S. Budd *et al.*, CDF-8037 (2006).

[72] T. Sjöstrand and L. Lönnbald, arXiv:hep-ph/0108264 (2001).

[73] C. Hill, J. Incandela, and C. Mills, CDF-7309 (2005).

[74] V. Martin, CDF-7031 (2005).

[75] U. Grundler, A. Taffard, and X. Zhang, CDF-7956 (2005).

[76] U. Grundler, A. Taffard, and X. Zhang, CDF-7262 (2006).

[77] Y. Ishizawa and J. Nielsen, CDF-7401 (2005).

[78] V. Boisvert, CDF-7939 (2005).

[79] O. Gonzalez and C. Rott, CDF-7051 (2004).

[80] H. Lai *et al.*, Eur. Phys. J. **C12**, 375 (2000).

[81] J. Pumplin *et al.*, JHEP **0207**, 012 (2002).

[82] V. Veszpremi *et al.*, CDF-8442 (2005).

[83] J. Efron *et al.*, CDF-8422 (2006).

[84] S. Chuang, M. Coca, and M. Kruse, CDF-7708 (2005).

[85] H. Kobayashi, K. Yamamoto, and Y. Seiya, CDF-7262 (2004).

[86] S. Lai and P. Sinervo, CDF-8203 (2006).

[87] L. Demortier *et al.*, CDF-4985 (2004).

[88] TeV4LHC Higgs working group, `http://maltoni.home.cern.ch/maltoni/TeV4LHC/SM.html`.

[89] The DØ Collaboration, Submitted to Phys. Rev. Lett., arXiv:hep-ex/0607022 (2006).

[90] The DØ Collaboration, DØ-5186 (2006).

[91] The DØ Collaboration, Submitted to Phys. Rev. Lett., arXiv:hep-ex/0607032 (2006).

[92] The DØ Collaboration, DØ-5063 (2006).

[93] The DØ Collaboration, DØ-5194 (2006).

Publication List

Published Papers

1. A. Abulencia *et al.* (the CDF Collaboration), "Measurement of the $t\bar{t}$ Production Cross Section in $p\bar{p}$ Collisions at $\sqrt{s} = 1.96$ TeV", Phys. Rev. Lett. **97**, 082004 (2006)
2. A. Abulencia *et al.* (the CDF Collaboration), "Search for Higgs Bosons Decaying to $b\bar{b}$ and Produced in Association with W bosons in $p\bar{p}$ Collisions at $\sqrt{s} = 1.96$ TeV", Phys. Rev. Lett. **96**, 081803 (2006)

Oral Reports

1. Y. Kusakabe *et al.*, "Search for Higgs Boson Production at CDF", CDF Collaboration Meeting, Elba, Italy, June 2006
2. Y. Kusakabe *et al.*, "$t\bar{t}$ Production Cross Section Measurement in Lepton+Jets Events", CDF Collaboration Meeting, Elba, Italy, June 2006
3. Y. Kusakabe *et al.*, "Search for Higgs Boson Production in Association with W Boson at CDF", American Physical Society, Dallas, Texas, USA, April 2004
4. Y. Kusakabe *et al.*, "Search for $WH \to \ell\nu b\bar{b}$ with 700 pb^{-1} at CDF", Higgs Workshop, Fermilab, Batavia, IL, USA, January 2006
5. Y. Kusakabe *et al.*, "Reconstruction of Parton Kinematics with Dynamical Likelihood Method", Japan Physical Society, Fukuoka, March 2004
6. Y. Kusakabe and K. Kondo, "General Formulation of Dynamical Likelihood Method", Japan Physical Society, Miyazaki, September 2003
7. Y. Kusakabe, J. Naganoma and K. Kondo, "A Method of Technicolor Search in W+2jet Channel with Dynamical Likelihood Method", Japan Physical Society, Tokyo, September 2002